ON THE EFFECT OF DIFFUSION ON GASEOUS DETONATION

A Dissertation

Submitted to the Graduate School
of the University of Notre Dame
in Partial Fulfillment of the Requirements
for the Degree of

Doctor of Philosophy

by

Christopher M. Romick

Joseph M. Powers, Director

Graduate Program in Aerospace and Mechanical Engineering

Notre Dame, Indiana

April 2015

ON THE EFFECT OF DIFFUSION ON GASEOUS DETONATION

Abstract

by

Christopher M. Romick

The development and propagation of detonations is examined in the presence of diffusive processes. The difference between the inviscid and viscous models is quantitatively evaluated for one-dimensional propagating detonations. First, an investigation of viscous effects is performed on one-dimensional pulsating unsupported Chapman-Jouguet detonations using a simplified one step kinetics model for various activation energies. The inclusion of viscosity in the model, delays instability to a higher activation energy and enlarges the activation energy range of the bifurcation process that leads to chaotic detonation. Then using detailed kinetics and full multi-component diffusion, a set of one-dimensional piston-driven hydrogen-air detonations is evaluated. The diffusive processes alter the behavior near the stability point, but as the intrinsic instability grows in strength, the viscous effects diminish. Harmonic analysis is used to illustrate how the frequency spectra of the pulsations evolve. Lastly, a study of the acceleration of several symmetric laminar flames in narrow two-dimensional channels is performed. Adiabatic no-slip walls contribute to the acceleration of the flame towards detonation by trapping the thermal energy that the boundary layer has converted from the mechanical energy of the propagating acoustic waves emanating from the flame. Below a threshold in channel width, viscous resistance becomes dominant and can significantly extend the time to the exponential pressure growth and acceleration of the flame. Increasing the percentage of diluent in the flame reduces the rate at which the flame accelerates and alters the width at which viscous resistance dominates. Ambient temperature isothermal walls retard the propagation of the flame in comparison to adiabatic walls at early times with the risk of extinction.

This work is dedicated to my loving wife, Evva.

CONTENTS

FIGURES

TABLES

SYMBOLS

Roman Letters

$\mathcal{A}_{ik}$	A ratio of collision integrals
a	Rate of acceleration to the initial plateau for the supporting piston velocity
a_j	Collision frequency factor of the j^{th} reaction
a_{ki}	Coefficients of the polynomial fit for specific heat capacity at constant pressure of the i^{th} specie
a_o	Ambient sound speed
$\mathcal{B}_{ik}$	A ratio of collision integrals
b	Rate of acceleration to the final supporting piston velocity
b_{ki}	Coefficients of the polynomial fit for viscosity of the i^{th} specie
$\mathcal{C}_{ik}$	A ratio of collision integrals
c	Constant
c	Order of a fitting polynomial for the specific heat capacity at constant pressure
c_{p_i}	Specific heat capacity at constant pressure of the i^{th} specie
c_i^i	Internal part of molecular specific heat capacity of the i^{th} specie
c_i^r	Rotational part of molecular specific heat capacity of the i^{th} specie
c_p	Specific heat capacity at constant pressure of the mixture

$\mathbf{c}_{\mathsf{U}}$	$N-$sized solution vector of the $\mathsf{L}-$matrix system
D	Wave speed of the leading shock
D_S	Wave speed of the weakened leading shock
D_λ	Mixture mass diffusion coefficient of the one step model
D_{ik}	Multicomponent diffusion coefficient between the i^{th} and k^{th} species
D_{CJ}	Wave speed of the leading shock in the Chapman-Jouguet case
D_i^T	Thermal diffusion coefficient of the i^{th} specie
$\mathcal{D}_{ik}$	Binary diffusion coefficient between the i^{th} and k^{th} species
$\mathcal{D}_{ik}^i$	Binary diffusion coefficient of internal energy between the i^{th} and k^{th} species
d	Dimension of problem
E	Non-dimensional activation energy in the one step model
$\overline{E}_j$	Activation energy of the j^{th} reaction
E_0	Activation energy of neutral stability boundary
E_n	Activation energy at which the behavior switches from a period-2^{n-1} to a period-2^n solution for $n \geq 1$
E_n^d	Diffusive E_n
E_n^i	Inviscid E_n
e	Specific internal energy of the mixture
e_i	Specific internal energy of the i^{th} specie
$\bar{e}_i$	Internal energy of the i^{th} specie per mole
f	Overdrive of the detonation
$\overline{g}_i^o$	Chemical potential at reference pressure of the i^{th} specie
h	Specific enthalpy of the mixture
h_i	Specific enthalpy of the i^{th} specie

$\overline{h}_i$	Enthalpy of the i^{th} specie per mole
h_i^f	Specific enthalpy of formation of the i^{th} specie
$\boldsymbol{\mathsf{I}}$	Identity matrix
$\imath$	Square root of -1
J	Number of reactions in the reaction mechanism
$\boldsymbol{\mathsf{j}}_i$	Diffusive mass flux of the i^{th} specie
K_B	Boltzmann's constant
K_j^c	Equilibrium constant for the j^{th} reaction
k	Isotropic thermal conductivity of the mixture
k_j	Arrhenius kinetic rate of the j^{th} reaction
L	Number of elements in the reaction mechanism
$L_{1/2}$	Half-reaction zone length in the one step model
$L_{1/2_{max}}$	Maximum half-reaction zone length in a time-dependent calculation
$L_{1/2_{min}}$	Minimum half-reaction zone length in a time-dependent calculation
L_{d_D}	Domain length necessary in a steadily traveling reference frame at speed D
L_{d_f}	Domain length necessary with the leading shock a fixed distance from the boundary
L_μ	Diffusive length scale in the one step model
L_{ign}	Length estimate before re-ignition
$\mathsf{L}^{\mathsf{U},\mathsf{U}}$	$N \times N$ sub-matrix of the $\mathsf{L}-$matrix system
L_x	Characteristic length scale of the energy deposition in the x-direction
L_y	Characteristic length scale of the energy deposition in the y-direction
Le	Lewis number
M	Third body chemical symbol

$\overline{M}$	Molecular mass of the mixture
$\overline{M}_i$	Molecular mass of the i^{th} specie
Ma	Ma number
N	Number of species in the reaction mechanism
$N_{1/2}$	Number of points in the steady half-reaction zone length for the one step model
N_{t_i}	Number time steps necessary in a inviscid computation
$N_{t_{RK}}$	Number time steps necessary in a viscous computation with the Runge-Kutta integration scheme
$N_{t_{RKL}}$	Number time steps necessary in a viscous computation with the Runge-Kutta-Legendre integration scheme
$\mathcal{N}_A$	Avogadro's constant
$\mathcal{O}$	Order of magnitude
P	Continuous Fourier transformation of the signal, $p(t)$
P_k	Discrete Fourier transformation of the signal, $p(t)$, at the k^{th} mode.
$\mathbf{P}$	$N \times N$ matrix defined as the inverse of the first sub-matrix of the $\mathsf{L}-$matrix system
P	Product symbol for the one step model
p	Pressure of the mixture
p	Order of a fitting polynomial for the specie viscosity
p^o	Reference pressure
p_o	Ambient pressure of the mixture
p_S	Shock pressure
p_s	Selected pressure
Pr	Prandtl number
$\mathbf{q}$	Total heat flux vector
q_n	Non-dimensional heat release of the one step model
q_r	Heat release of the one step reaction model

R	Reactant symbol for the one step model
$\mathcal{R}$	Universal gas constant
r_j	Reaction rate of the j^{th} reaction
s_i^f	Specific entropy of formation of the i^{th} specie
s_i^o	Specific entropy at reference pressure of the i^{th} specie
$\overline{s}_i^o$	Entropy at reference pressure of the i^{th} specie per mole
Sc	Schmidt number
T	Mixture temperature
T^o	Reference temperature
t	Temporal coordinate
t_a	Acoustic time scale
$\tilde{t}$	Temporal coordinate in the accelerating frame of reference
$\hat{t}$	Dummy integration variable
t_a	Time at which the initial acceleration of the supporting piston is centered
t_b	Time at which the deceleration to the final piston velocity is centered
t_m	Number of acoustic time scales over which the energy deposition lasts
t_f	Final time of integration
t_{ign}	Time to re-ignition
$\mathbf{u}$	Particle velocity vector of the mixture
$\tilde{u}$	Particle velocity in the accelerating frame
u_S	Shock particle velocity of the mixture
$u_p(t)$	Velocity of the supporting piston
$\overline{u_p}$	Final supporting piston velocity
u_{p_o}	Initial plateau in supporting piston velocity

$\mathbf{x}$	Spatial coordinates
x_c	Center of the energy deposition in the x-direction
$\tilde{x}$	Spatial coordinate in the accelerating frame
Y_i	Mass fraction of the i^{th} specie
y_c	Center of the energy deposition in the y-direction
y_i	Mole fraction of the i^{th} specie

Greek Letters

α_{ij}	Third body collision efficiency coefficient of the i^{th} specie for the j^{th} reaction
β_j	Temperature-dependency exponent of the j^{th} reaction
γ	Ratio of specific heats
Δt	Temporal spacing of a discrete signal
Δx	Grid resolution used in the computational method
Δx_i	Grid resolution necessary for an inviscid computation
Δx_v	Grid resolution necessary for an viscous computation
δ_{ij}	Kronecker delta
δ_∞	Feigenbaum's constant
ϵ	User-specified control threshold parameter that correlates to the error tolerated in the solution for the WAMR method
λ	Reaction progress variable for the one step model
λ_o	Ambient value of the reaction progress variable in the one step model
μ	Mixture viscosity
μ_i	Viscosity of the i^{th} specie
ν	Frequency
ν_h	High frequency in a pulsating detonation with multiple important active modes
ν_k	k^{th} frequency mode of a a discrete time-signal

ν_h	Low frequency in a pulsating detonation with multiple important active modes
ν_o	Fundamental frequency of pulsation
ν_{ij}	Net stoichiometric coefficient of the i^{th} specie in the j^{th} reaction
$\nu_{ij}^{'}$	Stoichiometric coefficient of the i^{th} specie in the reactants of the j^{th} reaction
$\nu_{ij}^{''}$	Reverse stoichiometric coefficient of the i^{th} specie in the products of the j^{th} reaction
ξ_{ik}	Relaxation collision numbers for the i^{th} and k^{th} species
ρ	Mixture mass density
ρ_o	Ambient mixture mass density
ρ_S	Shock mixture mass density
σ	Leonard-Jones collision diameter of the i^{th} specie
$\boldsymbol{\tau}$	Viscous stress tensor
Φ	Continuous PSD of a signal
Φ_d	Discrete PSD of a signal
$\phi(t)$	Continuous autocorrelation function of the signal $p(t)$
χ_i	Chemical symbol of the i^{th} specie
$\dot{\omega}_i$	Molar production rate per unit volume of the i^{th} specie
$\boldsymbol{\Omega}$	Collision Integrals

Other Symbols

∇	Spatial gradient operator

ACKNOWLEDGMENTS

I would like to thank my advisor, Dr. Joseph M. Powers for his support, guidance, and valuable insights. He has helped improve my writing skills and be able to convey my ideas in concise and straightforward manner. I am grateful for the advice and knowledge he has imparted to me.

I am also very thankful to Dr. Tariq D. Aslam for all the help, encouragement, and support. The numerous discussions we had has molded my thoughts and actions while working towards this dissertation. Additionally, I would like to acknowledge Los Alamos National Laboratory for its generous funding of my work.

I am also indebted to Dr. Samuel Paolucci and Dr. Karel Matouš for all of the computational resources they allowed me to utilize for this work. I would also like to thank Dr. Gretar Tryggvason for serving on my committee. I am so deeply thankful for the great friendships and the motivation to continue the pursuit of this Ph.D. of Dr. Patrick Bowden, Dr. Carlos Chiquete, Dr. Jorge Ferrer-Pérez, and Temistocle Grenga.

For the unending support and dedication at all times of night and day, I thank my parents and my wife. I am extraordinarily lucky to be your son and husband.

CHAPTER 1

INTRODUCTION

1.1 Motivation and Background

A critical concern of science is to develop a better explanation of the universe. The observable universe has many phenomena that span a wide set of scales. Such multiscale phenomena are encountered in a number of fields of practical interest such as astrophysics, biochemistry, material science, meteorology, and combustion. In the case of combustion, this broad range of scales is caused by a complex interaction between reactive, advective, and diffusive processes.

The modeling of these phenomena presents a formidable task, even with modern computational capabilities. As an example, in combustion, complex chemically reactive flows can be represented in the continuum limit by the reactive, compressible, Navier-Stokes (NS) equations. The Navier-Stokes equations are a set of coupled partial differential equations (PDEs) governing the conservation of mass, linear momenta, energy, and evolution of species mass fractions. Even with the assumption of a continuum, there can exist a vast range of temporal and spatial scales. For atmospheric pressures, the temporal scales can range from the macroscale, $\mathcal{O}(\mathrm{s})$, down to those of the finest reaction scales, $\mathcal{O}\left(10^{-9}\ \mathrm{s}\right)$; the spatial scales can range from near the mean-free path length scale, $\mathcal{O}\left(10^{-6}\ \mathrm{m}\right)$, up to the laboratory scale, $\mathcal{O}\left(\mathrm{m}\right)$ [108]. These fine reaction scales are a manifestation of an averaged representation of the molecular collision model in which the fundamental length scale is the mean free path [1]. In order to achieve a mathematically verified prediction, this wide range of scales must be resolved, which poses a daunting task. According to Manley et al. [79] there is "a single, overarching grand challenge for 21$^{\text{st}}$-century combustion science: the development of a validated, predictive, multiscale combustion modeling capability."

A specific reactive flow of interest today is a supersonic combustion wave in which exothermic energy release contributes a driving shock, more commonly known as a detonation wave. A detonation is a shock-induced combustion wave in which the exothermic energy release contributes to driving the shock. This phenomenon is of particular interest due to industrial safety [16, 95, 131, 141], and more recently, the emerging interest in detonation engines [82, 112, 122, 148]. Currently, the main projected application of supersonic combustion is flight, with the possibility to make any location on Earth reachable within two hours [75]. With supersonic/hypersonic combustion, there is a possibility for a lower cost per mass to send a payload into space; for these purposes as well as other purposes, there are air-breathing technologies under development. As an example, the X-51A Waverider successfully flew for almost 200 seconds, reaching approximately Mach 5 [96]. Even though its main application is flight, supersonic combustion also has potential in other areas *e.g.* powder coating [94], removal of build-up of slag [53], and power production. Moreover, entrepreneurs are already filing for patents for detonation-driven power generators [76]. Furthermore according to industry leaders, there is a potential to increase in the fuel-efficiency using pulsating detonations over current power production techniques [64, 81].

Detonations which are self-sustained show a nearly universal instability [69]. There are several types of instabilities that have been observed, *e.g.* longitudinal, rectangular, diagonal, and spinning. The rectangular and diagonal instabilities have been detected in rectangular cross-sectional shock tubes. The rectangular instability is characterized by the triple points moving parallel to the tube walls and two sets of orthogonal “slapping” waves. The diagonal instability is characterized by a three-dimensional structure in which the triple points propagate diagonally with respect to the tube’s cross section. The key criterion in determining which instability forms is the way the detonation is initiated [44]. If a diaphragm in a reactive shock tube is pre-cut along the diagonal of the cross section, the rectangular instability results; when the pre-cut is along the median of the cross-section, the diagonal instability manifests itself. A spinning instability can develop in a multitude of geometric cross-sections, including circular, square, and triangular, and consists of one or more shocks traveling around the long axis of the shock-tube in the azimuthal direction. It has also been observed that the pitch of spinning is proportional to the cross-section’s diameter ratio, and that the instability normally occurs in mixtures near the limits of detonation [25, 30]. The longitudinal instability only exists in small diameter tubes where the development of the multi-dimensional instabilities are hindered. These galloping instabilities occur along the direction of propagation of the detonation wave; the front can be seen periodically or irregularly speeding up or slowing down [142].

Evidence of these many instabilities have been observed experimentally in soot-tracks [69]. These soot-tracks are records of where these transverse waves intersect with each other and the leading shock, or triple points [97]. These triple points trace cellular patterns on soot-coated foil placed in the shock tube. These cellular patterns are dependent on the composition of the gaseous mixture as well as the initial (upstream) pressure [143]. These patterns can both be regular, with a consistent cell-size for weakly unstable mixtures like highly diluted hydrogen-oxygen mixtures, and very irregular, for a more complex fuel-air mixture like methane [5]. Figure 1.1 shows examples of these patterns on smoke foils produced by Austin [5]. A zoomed profile, of the detonation front illustrates some of the basic multi-dimensional features of an instability for a propagating detonation in a highly-dilute hydrogen-oxygen mixture,

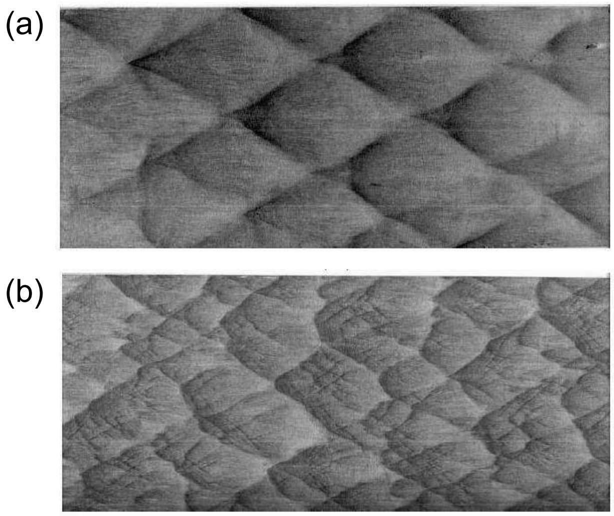

Figure 1.1. Smoke foil patterns from Austin [5] of detonations in mixtures of (a) $2H_2 - O_2 - 12Ar$ and (b) $C_3H_8 - 5O_2 - 9N_2$.

is shown in Figure 1.2.

The underlying mechanisms driving detonation instabilities are not particularly well understood; thus the process of detonation formation is also of great interest. One of the earliest studies into the formation of detonation was done by Chapman and Wheeler [13], who studied the speed at which a flame propagated in a methane-air mixture. Oppenheim et al. [98] were the first to suggest an "explosion within a explosion" for a theory that lead to a detonation from a subsonic flame (deflagration). Oppenheim et al. [99] first reported the recording of compression waves from a laminar flame which eventually coalesced to form a shock wave and thus perturbed the trailing laminar flame, leading to detonation, or in other words the deflagration-to-detonation transition (DDT).

The simplest model of a detonation treats the detonation as a discontinuity between the ambient upstream state and the downstream thermochemical equilibrium state. The minimum velocity at which the detonation can propagate was first predicted by Chapman [11] and Jouguet [57], using only the inviscid steady one-

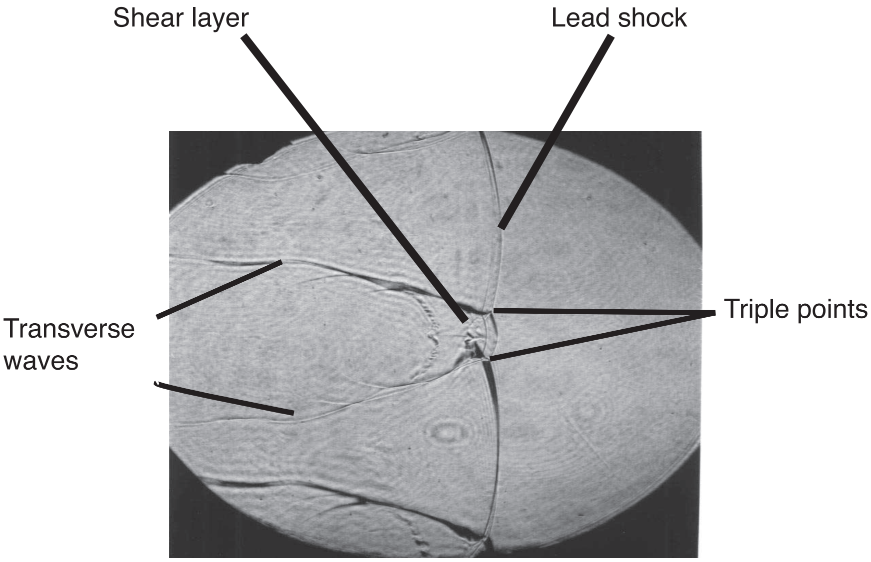

Figure 1.2. A schlieren image from Austin [5] of a detonation in a mixture of $2H_2 - O_2 - 17Ar$ at ambient pressure of $p_o = 20$ kPa. The basic structure of the instabilities in the detonation has been highlighted.

dimensional jump conditions. The corresponding state to this minimum velocity is often referred to as the Chapman-Jouguet (CJ) state for this reason and is a sonic point. It is noteworthy, that while it was largely unknown outside of Russia at the time, Mikhelson [88] did much of the same work as Chapman and Jouguet. This idea was an extension of the earlier work of Rankine [114] and Hugoniot [51], who formulated inviscid jump conditions for an inert shock wave.

This understanding was furthered by the work of Zel'dovich [178], von Neumann [160], and Döring [24], who accounted for the fact that the detonation wave has finite thickness due to the finite time of chemical reaction. In this model the leading shock, which is still described as discontinuity, raises the temperature and the pressure peaks initiating the chemical reactions. This is usually followed by an induction zone in which primarily dissociation reactions occur. The induction zone is followed by a recombination zone where most of the energy is released due to exothermic reactions. This energy release raises the temperature, ultimately causing an expansion to the sonic CJ state in the unsupported case [33]. This one-dimensional, steady model that utilizes a leading inviscid shock followed by a finite-rate energy release is known as the ZND model. This model added insight to the propagation of the detonation; there is adiabatic heating by the leading shock which is then supported by the expansion of the burnt fuel.

In addition to the previously mentioned CJ case, it is also possible to have a detonation that has a piston at the back of the burnt expanded gases that prescribes a velocity higher than the minimal CJ final state velocity. These piston-supported detonations are typically referred to overdriven detonations, where the overdrive of the detonation, $f = (D/D_{CJ})^2$, in which D is the wave speed of the leading shock and D_{CJ} the wave speed of the leading shock in the CJ case. This imposed rear boundary state is connected to the final reaction state via a constant state for a steady model, and thus, this enforces the wave speed of the detonation to realize this prescribed reaction zone final state. Therefore, the only way to achieve this overdriven state in the steady case is through an external force, like a supporting piston.

The models described thus far are strictly steady-state approximations. However as previously mentioned, there is much experimental evidence that many detonations are intrinsically unstable; though both the CJ and ZND theories have been successful in predicting the detonation velocity in an average sense [33]. With the mechanisms driving detonation instabilities not fully understood, no theory exists to predict the behavior of a specific detonation. This has led to many numerical studies, to gain greater insight into the hydrodynamics of detonations.

The intricate coupling between the fluid mechanics and chemistry, however, results in difficultly in accurately modeling detonations. This is due to the fact that there is a large breadth of scales that must be captured. Devices of interest, *i.e.* pulse detonation engines or shock-tubes, are on the order of meters. Additionally, Powers and Paolucci [108] demonstrated, using an spatial eigenvalue analysis for a steady, CJ detonation propagating into a stoichiometric mixture hydrogen-air at an ambient state of 1 atm and 298.15 K, the smallest chemical reaction length scales to be $\mathcal{O}\left(10^{-7}\ m\right)$. This estimation is on the same order of the mean-free path, and these fine length scales are a manifestation of the averaged continuum representation of the collisions that occur between molecules, which have an underlying principal length scale of the mean free path [1]. Furthermore, diffusive effects occur on similar scales, and thus, need a comparable resolution to be captured correctly.

In order to reduce the computational resources necessary to simulate the development and propagation of detonations, several assumptions can be made. The first assumption that is usually made is to neglect diffusive processes, as their effects are thought to be small in comparison to advection and reaction, *cf.* Fedkiw et al. [31], Walter and da Silva [162], and He and Karagozian [46]. Secondly, as mentioned by Shepherd [132], it is a common practice to use a reduced kinetics or simplified model. Additionally, the model can be reduced to a single spatial dimension. Although many of the intrinsic instabilities of detonations are multi-dimensional, valuable information about how the structure of detonations evolve, how instabilities develop, and how detonation velocities change in time can all be gained through one-dimensional studies.

There are indications that the first assumption, of neglecting diffusion, may be problematic. Singh et al. [138] and Powers [107], in a two-dimensional study of detonation patterns using a one step kinetics model, demonstrated that for the reactive Euler equations detonation patterns were grid-dependent. Moreover, the patterns using the reactive Navier-Stokes equations reduce to a grid-independent dissipative structure. Furthermore, while using grid sizes around $10^{-6}\ m$ for their three-dimensional simulations of unsteady hydrogen-air detonations, Tsuboi et al. [156] report wave dynamics that show strong sensitivity to the grid. While apparent convergence of some structures was reported, they also note with regard to some particulars of the detonation structure “The present results cannot resolve such cross-hatchings in the ribbon because of a lack of grid resolution.” Likewise, Deiterding [22] also reports that the interactions between chemistry and hydrodynamic flow in inviscid detonations “in general exhibit a strong dependency on the mesh spacing.” Additionally, in regions that require high resolution for a one step detonation in a channel, diffusion plays an important role [85]. Al-Khateeb et al. [2] suggests that hydrogen-air mixtures have reaction length scales present which have time scales associated with them over which both chemistry and diffusion can be important. The presence of reaction dynamics and steep gradients at micron length scales suggests that in fact physical diffusion has an important role to play. These results suggest that numerical diffusion could play a significant role in the inviscid calculations. Thus, the introduction of grid-independent physical diffusion should be considered, and the overall effect on detonations needs to be quantified.

Before relaxing either of the other assumptions of using simplified kinetics or one-dimensional flow, it is useful to examine the interaction between chemistry and advective processes and transport phenomena in the simplest model. The simplest kinetic model is one that is composed of a single reaction. This introduces a single chemical reaction length scale, in contrast to the multiple reaction scales of detailed kinetic models; thus, allows the interplay between chemistry and transport phenomena be more easily studied. Additionally, restricting the model to one dimension permits more resolution to be used at a lower computational cost [124]. Moreover, in two dimensions Watt and Sharpe [166] conclude, that “resolved and accurate calculations of the cellular dynamics are currently computationally prohibitive, even with a dynamically adaptive numerical scheme.” Furthermore, in two-dimensions Radulescu et al. [113] found that the correct average chemical thickness observed in experiments cannot be realized using artificial diffusive terms alone.

Such a model has been studied extensively in the inviscid limit. The stability and non-linear dynamics of this "one step" model are well understood. The following review is meant as a broad overview of work done in one dimension, but is not all-inclusive.

Erpenbeck [28, 29] began the study into the stability of the ZND profile of the standard one step irreversible kinetic model. Lee and Stewart [68] furthered the early work of Erpenbeck by developing a normal-mode approach to the linear stability of the idealized detonation to one-dimensional perturbations using a shooting method to find the unstable modes. Bourlioux et al. [10] studied the nonlinear development of instability in this one step model. The investigation into the stability of the one step kinetic model was continued by He and Lee [45] using the Euler equations in one dimension. They found two critical activation energies; the first critical activation energy separated the stable and unstable regimes, and the second separated the unstable regime from a regime where the period of oscillations became infinite. Using a newer normal mode approach, Sharpe [127] found results in good agreement with Lee and Stewart [68]; however, using asymptotics it was also found that the overdriven detonations did not tend to the CJ detonation as the overdrive approached unity. Montgomery et al. [90] used the one step model in the inviscid limit to study the critical length for DDT in a initially perturbed linear temperature gradient and found that the perturbations can increase the critical length an order of magnitude versus the unperturbed case. Eckett et al. [27] studied the one step model in context of direct initiation of a detonation using a blast wave in spherical coordinates in one dimension. In the inviscid limit, Sharpe and Falle [128] found that a minimum of 100 points was required in the half-reaction length to achieve a converged solution. Short and Wang [135] studied the dynamics of pulsating detonations enforcing at most two linearly unstable modes and found that the lower frequency dominated in all cases studied except one. In this exception, the amplitude of the lower frequency still dominates. Kapila et al. [58] studied how the initial temperature gradient affects the development and evolution of detonations, while using a one step kinetics model in the inviscid limit. It was found that weak detonations can form if the initial gradient was weak, but then decayed to CJ conditions given a sufficiently long computational domain. Daimon and Matsuo [19] performed simulations for various overdriven detonations and predicted a bifurcation process as the overdrive was lowered. A normal mode approach was applied by Kasimov and Stewart [59] to the linear stability problem of the ZND profile; they performed a numerical analysis using a first order shock-fitting technique. Ng et al. [93] developed a coarse bifurcation diagram showing how the oscillatory behavior became progressively more complex as activation energy increased. Henrick et al. [47] developed a more detailed bifurcation diagram using a true fifth order shock-fitting method. Kassoy [60], Kassoy et al. [61], and Regele et al. [118] studied the development of DDT using a local thermal power deposition function as a novel way to initialize the flame and simulate a spark, realizing detonation waves on the microsecond time scale.

Several one-dimensional studies of detonations have included transport processes in the one step limit. The earliest works focused on finding a strictly steady diffusive detonation. Friedrichs [35] included both viscous and thermal dissipation, but neglected mass diffusion as the reaction was treated as a discontinuity, from unreacted to fully reacted as in CJ Theory. Hirschfelder and Curtiss [48] expanded ZND theory by including mass, momentum, and energy diffusion while studying a one step irreversible model. In addition to restricting the Lewis and Prandtl numbers, it was necessary to treat the shock and reaction separately, only including viscous and thermal dissipation in the shock zone. Wood [171, 172] tested several activation energies as well as several ratios of specific heats. For the values tested under certain conditions, a “strictly” steady solution was possible in the overdriven state. Using the one step kinetics model, Clarke et al. [17, 18], examined the effects of diffusion on the development of a detonation from a small energy release. Wagner [161] showed the existence of a steady planar viscous detonation wave under a special condition on the Prandtl number. The work of Clarke et al. [17, 18] was continued by Sileem et al. [137], who used a power deposition function that acted only over a prescribed time and is then suppressed, to initialize a DDT. Using the Navier-Stokes equations, Chen [14] demonstrated solutions of the one step model in Euler and Lagrange coordinates are equivalent. Gasser and Szmolyan [39] were able to show the existence of steady diffusive strong detonations in the limit of weak diffusion. The nonlinear stability of a strongly overdriven detonation was examined by Tan and Tesei [147] using the one step model in the Navier-Stokes equations. Lyng and Zumbrun [78] studied the stability of a one step detonation in the weak diffusion limit. Texier and Zumbrun [152], expanding on the earlier work of [78], demonstrated that in the weak diffusion limit, a one step detonation will undergo a transition through a Hopf bifurcation as the overdrive is lowered. Through the use of Evans functions, Humpherys et al. [52] demonstrated for the Majda's scalar model of detonation an unstable mode in the inviscid limit can revert to a stable mode when diffusive effects are accounted for in the model. As the development of an analytical solution for a viscous detonation is not the main focus of this work, the reader is referred to the references in Humpherys et al. [52] for further developments in this area.

Expanding the kinetics model adds more reaction length scales and likely stiffness; additionally, the chemical reaction mechanism can have greater fidelity with experiment and thus, more closely mimics the physical world. Several studies in the inviscid limit have examined the behavior of extended simplified kinetics models in one dimension [84, 92, 123, 126, 129, 136, 140]. However, many studies with larger kinetics models in fact use detailed kinetic models of a full reaction model which has been developed for the particular gaseous mixture of interest. This allows individual components of the mixture to have their own intrinsic properties and the mixture's properties to be composed of a combination of the individual components' properties.

The following is meant to highlight some important works done with detailed kinetic mechanisms in the one-dimensional limit. One of the first to model shock-induced combustion with detailed kinetics was Sussman [145], who used the same hydrogen-air mixture and ambient pressure and temperature as used by Lehr [70] in experiments of flow around spherical projectiles. The computations were performed with only twenty points in the induction zone; however, the predicted behavior grew more complex as the overdrive was lowered, similar to the results found in various one step studies. Eckett [26] performed numerical simulations of pulsating hydrogen-oxygen detonations in the inviscid limit and found that as the overdrive of the detonation was decreased, more complex behavior in the pulsations occurred. In order to achieve a converged solution, a minimum of 150 cells were necessary in the induction zone. Singh et al. [139] calculated the development of an argon–diluted hydrogen–oxygen viscous detonation in one dimension after a reflected shock passes through the mixture. While studying both hydrogen-carbon dioxide-air and hydrogen-air mixtures using the spherical Navier-Stokes equations in one dimension, Gu et al. [42] predicted upper and lower bounds on the initial temperature gradient needed to develop a detonation from a hotspot. Yungster and Radhakrishan [175] studied the stability of hydrogen-air mixtures in the inviscid limit for various equivalence ratios and overdrives using a strong shock wave to directly initiate the detonation. From a grid-convergence study, it was found that a resolution on the order of a micron was needed for a converged solution for a detonation propagating into a pressure of 0.2 bar. Using the one-dimensional Euler equations in one dimension, Yungster and Radhakrishan [176] then studied ethylene-air mixtures and predicted that as the equivalence ratio is increased, the amplitude of the pulsating detonations grows and the periodicity increases, similar to that seen in the simpler hydrogen-air model. Using the one-dimensional cylindrical Navier-Stokes equations, Wang et al. [163] studied a mixture of hydrogen-oxygen mixture diluted by argon in the context of a implosion and found that a secondary implosion caused by the interaction of the reflected shock and the imploding contact discontinuity caused the system to reach a much higher temperature and pressure than that of the reflected shock alone. Daimon and Matsuo [20] examined various equivalence ratios and overdrives using a hydrogen-air mechanism in the inviscid limit and reported similar results found by [26, 145, 175] who studied other hydrogen-based fuel mixtures.

The necessary resolution in modeling detonations has limited the number of multi-dimensional studies performed. Much of the early work of detonation modeling in multiple dimensions made use of simplified kinetics [56, 104, 134, 168]. Additionally, to reduce the computational cost, most studies were performed in the inviscid limit as well [3, 71, 72].

Some of the earliest work in multiple dimensions was performed by Oran et al. [102], using the one step model with a fitted induction zone to hydrogen-air and methane-air mixtures, and Taki and Fujiwara [146], using a two step model. Using the one step irreversible Arrhenius kinetics model, Bourlioux and Majda [9] performed both analytic and numerical studies for several values of activation energy and heat release and noted that artificial numerical viscosity is grid dependent; therefore, the range of wavelengths that can be unstable is limited by the mesh chosen. Gamezo et al. [37, 38] examined cellular detonations in the inviscid limit with the one step model using a shock to directly initiate the detonation. It was reported that as activation energy increased, the cellular structures became more irregular and that in two dimensions the average reaction zone length was longer than in a single dimension. Gavrikov et al. [40] performed both two- and three-dimensional simulations in the inviscid limit using the one step model to find the cell width and to create a correlation between it and the one-dimensional characteristic reaction zone thickness. A resolution study was performed by Sharpe [125] on the detonation structure with strong transverse waves in the inviscid limit, and it was found that to ensure the transverse wave structure was properly captured, more than fifty points were needed in the half-reaction length of the one step model. Moreover, it was noted that the results of using the Euler equations will not converge quantitatively, because artificial numerical viscosity is grid dependent. Sharpe and Quirk [130] used a parallel adaptive mesh in two dimensions with the one step model in the inviscid limit to study a wide channel in a hope to find the intrinsic cell size. It was found even in the weakly unstable case there was not a unique final cell size; however, it was also shown that the average cell length-to-width ratio was well predicted by linear analysis. In the inviscid limit using the one step model, Teng et al. [151] examined how the half-reaction length evolved in oblique detonations.

Though detailed kinetic mechanisms add stiffness to the reaction model, several studies have been performed in the inviscid limit. One of the earliest was done by Oran et al. [103], who examined the development of detonations in a highly diluted hydrogen-oxygen mixture diluted by argon at low pressure. Tsuboi et al. [155] performed a three-dimensional simulation of a 2 mm long, 0.5 mm square channel with a 5 μm resolution using a hydrogen-air mixture and predicted the appearance of both rectangular and diagonal instabilities. While studying a mixture of hydrogen and oxygen diluted by argon in the inviscid limit, Hu et al. [49, 50] calculated the cellular structure and found that at an ambient pressure of 6.67 kPa, a resolution on the order of 25 μm was needed and reported that the results matched closely those of [103]. Deiterding [21] studied this same problem as [49, 50, 103] with his parallel adaptive scheme and was able to go onto a three-dimensional simulation like that of [155], using maximum resolution 16.8 points in the induction zone. Additionally, the behavior of the detonation through a 60 degree bend in two dimensions was predicted in the inviscid limit. Taylor et al. [149] made a comparison of the intrinsic cell-sizes from a directly initiated detonation between those from the one step model and detailed kinetics for two hydrogen-based fuel mixtures.

The extension of detonation modeling to multi-dimensional studies introduces the geometric effects; thus, allowing more of the physics to be captured than in a one-dimensional model. There are several studies examining multi-dimensional behavior of detonations with both simplified and detailed kinetics in the presence of physical diffusion. One of the first was performed by Khokhlov et al. [65], who examined the shock-flame interaction that lead to a detonation with the one step model in the Navier-Stokes equations. Tegnér and Sjögreen [150], using the one step model examined the development of the DDT phenomenon from a small region initialized at higher state. A pre-heating shock eventually forms and when it reaches sufficient strength, a dramatic increase in pressure occurs followed by a decay to the self-supporting CJ detonation, in agreement with other DDT studies. Both two- and three-dimensional studies were performed by Oran and Gamezo [101] of the shock-flame interaction leading to detonation for the one step model fitted to acetylene-air and ethylene-air mixtures. Using a simplified kinetics model starting from an already initiated detonation, Kivotides [66] demonstrated that in a micro-channel, the transverse wave behavior of a detonation can be altered by diffusive processes. Yuan and Tang [174] studied shock-induced combustion around a blunt body using the Navier-Stokes equations and an adaptive mesh redistribution method. While studying both detailed kinetic mixtures of hydrogen-oxygen and hydrogen-air, it was found that at high Mach numbers, if a very fine mesh was used or consecutive steps had grid redistribution, that false combustion instabilities occurred. Wang and Xu [164, 165] used the two-dimensional Navier-Stokes equations with detailed kinetics to simulate diffraction and re-initiation of a detonation in a low pressure hydrogen-oxygen-argon mixture. While studying flame acceleration to a detonation in a channel, it has been shown that there is qualitative agreement between experiments and computations for a pure hydrogen-oxygen mixture [54, 55, 73, 74]. Ziegler et al. [179] used detailed kinetics and reported that for a viscous double Mach reflection detonation of hydrogen-air a near micron grid-size was not quite sufficient to resolve all the strong shocks present. While studying several activation energies in the context of the one step model, Mazaheri et al. [85] reports that in regions that require high resolution, diffusion plays an important role. Chinnayya et al. [15] examined the viscous behavior of an already initiated one step detonation in a narrow channel at low pressure and showed in narrower channels the addition of viscosity can completely damp the transverse wave behavior. Recently, Lv and Ihme [77] studied several test problems for a discontinuous Galerkin method including several detailed kinetics deflagrations with the inclusion of diffusion.

1.2 Structure of Dissertation

The remainder of this dissertation is organized as follows. In Chapter 2, the mathematical representation used in the continuum approximation for unsteady, gaseous, reactive compressible flows is developed. This development includes detailed mass-action kinetics and multicomponent transport phenomena. In addition to this detailed model, a reduction of this description is presented for a simplified model that consists of a single reaction and a single specie each for the combined reactants and products.

Chapter 3 presents a one-dimensional study [120] of the reduced model for CJ detonations while varying the activation energy of the reaction. In fact, it is the diffusive analog of the inviscid study by Henrick et al. [47]. The aim of this work is to highlight the effect of diffusive processes on pulsating detonations. The use of the one step model introduces a single reaction length scale, and thus, allows the interplay between chemistry and transport phenomena be more easily studied. Additionally, a new harmonic analysis of the temporal behavior of the detonation pressure is presented followed by an examination of the evolution of the half-reaction zone length.

In Chapter 4, the work examining the effect of diffusive processes on pulsating detonations is extended to include detailed kinetics [121]. A one-dimensional study of piston-driven flows of a stoichiometric hydrogen-air mixture is presented. This study examines how the long time behavior of the detonation evolves as the supporting piston velocity is varied. The behavior is examined in both the temporal and frequency domains and a comparison is made between the inviscid and viscous analogs.

Chapter 5 consists of a DDT study for several hydrogen-based fuel mixtures in narrow channels. Here, the effects of channel width and percent of diluent on the time to transition is presented. Additionally, the effect of ambient temperature isothermal boundaries is explored and compared with the acceleration process with adiabatic boundaries. Finally, Chapter 6 summarizes the overall work and suggestions for future directions in research.

The evaluation of detonation cell sizes, like those found experimentally and shown in Figure 1.1, is computationally expensive when all spatial and temporal scales associated with reactive, advective, and diffusive processes are resolved. The instabilities helping these detonations propagate have very fine features demonstrated in Figure 1.2. The finest spatial scales that must be resolved at the high pressures present in detonations propagating in ambient atmospheric pressure are on the $\mathcal{O}\left(10^{-7}\text{ m}\right)$ or smaller. This means that with an explicit temporal integration scheme, the required time step required is on the $\mathcal{O}\left(10^{-12}\text{ s}\right)$ or smaller in magnitude. Typical wave speeds in detonations are $\mathcal{O}\left(10^{3}\text{ m/s}\right)$; thus for a 10^{-3} m wide channel, the time for transverse wave to propagate across the channel is $\mathcal{O}\left(10^{-6}\text{ s}\right)$. A single half cycle of the propagation of a transverse wave requires $\mathcal{O}\left(10^{6}\right)$ time steps. Moreover, numerous cycles of these transverse waves are necessary to quantify the cell sizes predicted. Additionally, the detonation front is propagating within the channel, giving a minimum ratio of spatial scales of $\mathcal{O}\left(10^{4}\right)$ that needs to be resolved in multiple directions. Thus, performing a comprehensive study for various channel widths and mixtures is computationally intractable without reducing the ratio of either the spatial or temporal scales or both. This dissertation will focus on resolving all relevant scales of the model, and thus, an examination of detonation cell sizes was not considered.

CHAPTER 2

MATHEMATICAL MODEL

In this chapter the general mathematical model is presented. The gaseous, compressible, reactive flows can be described by partial differential equations (PDEs) in the continuum limit. Modeling these flows, additionally, involves the initial and boundary conditions corresponding to the flow variables. The specific initial and boundary conditions for the specific problems examined in this work will be included in the following chapters for the individual problems. Likewise, the numerical methods used in numerical modeling of the individual problems will be presented in subsequent chapters.

The governing partial differential equations for a gaseous reactive mixture consisting of N species are the unsteady, compressible, reactive Navier–Stokes equations. Equations (2.1)-(2.4) represent the conservation of mass, linear momenta, energy and the evolution of species, respectively. In conservative form they are expressed as

$$\frac{\partial \rho}{\partial t} + \nabla \cdot (\rho \mathbf{u}) = 0, \tag{2.1}$$

$$\frac{\partial}{\partial t}(\rho \mathbf{u}) + \nabla \cdot \left(\rho \mathbf{u}\mathbf{u}^T + p\mathbf{I} - \boldsymbol{\tau}\right) = \mathbf{0}, \tag{2.2}$$

$$\frac{\partial}{\partial t}\left(\rho\left(e + \frac{\mathbf{u}\cdot\mathbf{u}}{2}\right)\right) + \nabla \cdot \left(\rho \mathbf{u}\left(e + \frac{\mathbf{u}\cdot\mathbf{u}}{2}\right) + (p\mathbf{I} - \boldsymbol{\tau})\cdot\mathbf{u} + \mathbf{q}\right) = 0, \tag{2.3}$$

$$\frac{\partial}{\partial t}(\rho Y_i) + \nabla \cdot (\rho \mathbf{u} Y_i + \mathbf{j}_i) = \overline{M}_i \dot{\omega}_i, \qquad i = 1, \ldots, N-1, \tag{2.4}$$

where $\nabla \equiv \partial/\partial \mathbf{x}$ is the spatial gradient operator, and the independent variables are t, the temporal coordinate, and $\mathbf{x}$ the spatial coordinate vector. The dependent variables are the mixture mass density, ρ, the mixture velocity vector, $\mathbf{u}$, the mixture pressure, p, the viscous stress tensor, $\boldsymbol{\tau}$, the specific internal energy of the mixture, e, the total heat flux vector, $\mathbf{q}$, the mass fraction, Y_i, the diffusive mass flux, $\mathbf{j}_i$, the molecular mass, $\overline{M}_i$, and the molar production rate per unit volume, $\dot{\omega}_i$, for the i^{th} specie. The $\mathbf{I}$ symbol is the identity tensor. Equations (2.1) and (2.3) are scalar equations. Equations (2.2) and (2.4) are vector equations of lengths d and $N - 1$, respectively, where d is the dimension of the problem. To close the system, constitutive relations must be specified.

2.1 Reactive Gaseous Mixture Properties

This work is restricted to ideal mixtures of calorically imperfect gases adhering to Dalton's model. This leads to a thermal equation of state of

$$p = \rho \frac{\mathcal{R}}{\overline{M}} T, \tag{2.5}$$

where $\mathcal{R} = 8.314 \times 10^7$ erg/(mole K) is the universal gas constant, $\overline{M}$ the mixture molecular mass, and T the mixture temperature [110]. The mixture molecular mass is given by

$$\overline{M} = \left(\sum_{i=1}^{N} \frac{Y_i}{\overline{M}_i} \right)^{-1} . \tag{2.6}$$

Additionally, as the mass fraction of i^{th} specie, Y_i, is defined as

$$Y_i = \frac{m_i}{m}, \qquad i = 1, \ldots, N, \tag{2.7}$$

where m_i is the mass of i^{th} specie and m the total mass in the system; logically it follows that

$$\sum_{i=1}^{N} Y_i = 1. \tag{2.8}$$

Furthermore, the mole fraction of the i^{th} specie can be defined as

$$y_i = \frac{\overline{M}}{\overline{M}_i} Y_i. \qquad i = 1, \ldots, N, \tag{2.9}$$

Therefore,

$$\sum_{i=1}^{N} y_i = 1, \tag{2.10}$$

and it also follows that Equation 2.6 can be written in terms of mole fractions as

$$\overline{M} = \sum_{i=1}^{N} y_i \overline{M}_i. \tag{2.11}$$

For a mixture consisting of N species composed of L elements, and interacting in J chemical reactions, the number of moles of l^{th} element in the j^{th} reaction is conserved. This molar balance can be expressed as

$$\sum_{i=1}^{N} \phi_{li} \nu_{ij} = 0, \tag{2.12}$$

for all elements, $l = 1 \ldots L$, and all reactions, $j = 1 \ldots J$, where ν_{ij} is the net stoichiometric coefficient of the i^{th} specie in the j^{th} reaction and ϕ_{li} the number of atoms of l^{th} element in the i^{th} species. Here $\nu_{ij} = \nu_{ij}^{''} - \nu_{ij}^{'}$, where $\nu_{ij}^{'}$ and $\nu_{ij}^{''}$ are the stoichiometric coefficients in the reactants and products of the i^{th} specie in the j^{th} reaction, respectively. Additionally, the molar production rate per unit volume of the i^{th} specie, $\dot{\omega}_i$, can be expressed in terms of the J reaction rates as

$$\dot{\omega}_i = \sum_{j=1}^{J} \nu_{ij} \mathsf{r}_j, \tag{2.13}$$

where r_j is the reaction rate of the j^{th} reaction. By applying Equations (2.12) and (2.13) to the sum of Equation (2.4) from $i = 1$ to N and comparing to Equation (2.1) demands that

$$\sum_{i=1}^{N} \mathbf{j}_i = \mathbf{0}, \tag{2.14}$$

thus indicating that the species mass flux are defined with respect to the mean flow.

The attention of this work is focused on two classes of models. One makes use of a realistic detailed kinetics model, and the other will employ several simplifications and use a single reaction. In the subsequent sections, the remaining constitutive relations used for the equation of state and reaction rates are defined. Additionally, the mass, momentum, and energy diffusion transport relations adopted will be detailed.

2.2 Detailed Model

In the realistic detailed kinetics model, the specific enthalpy of the i^{th} specie, h_i, is given by

$$h_i = h_i^f + \int_{T^o}^{T} c_{p_i}\left(\hat{T}\right) d\hat{T}, \tag{2.15}$$

where h_i^f is the the specific enthalpy of formation of the i^{th} specie evaluated at the reference state, which is given by the reference pressure, $p^o = 1 \text{ atm} = 1.01325 \times 10^6 \text{ dyne/cm}^2$, and the reference temperature, $T^o = 298$ K, and c_{p_i} the specific heat at constant pressure of the i^{th} specie. As all of the species are considered calorically imperfect ideal gases, the specific heats at constant pressure are independent of pressure but are a function of temperature. The specific heat at constant pressure of the i^{th} specie is evaluated from a polynomial fit in temperature that utilizes thermodynamic data as

$$c_{p_i} = \mathcal{R} \sum_{k=0}^{\mathsf{c}} a_{ki} T^k, \tag{2.16}$$

where a_{ki} are the coefficients of the c-order polynomial provided by the `CHEMKIN` [63] database. Note that this polynomial fit could be easily cast into a form using $(T/T_o)^k$ such that the coefficients could be dimensionless. Additionally, the specific entropy at reference pressure, s_i^o, of the i^{th} specie is given by

$$s_i^o = s_i^f + \int_{T^o}^{T} \frac{c_{p_i}\left(\hat{T}\right)}{\hat{T}} d\hat{T}, \tag{2.17}$$

where s_i^f is the entropy of formation of the i^{th} specie. The specific enthalpy can be used to calculate the specific internal energy, e_i, of the i^{th} specie as

$$e_i = h_i - \frac{\mathcal{R}T}{\overline{M}_i}. \tag{2.18}$$

The molar-based thermodynamic properties can be obtained by multiplying the species molecular mass,

$$\overline{e}_i = \overline{M}_i e_i, \tag{2.19}$$

$$\overline{h}_i = \overline{M}_i h_i, \tag{2.20}$$

$$\overline{s}_i^o = \overline{M}_i s_i^o. \tag{2.21}$$

Furthermore, using these molar-based quantities, the species chemical potential at reference pressure for the i^{th} specie, $\overline{g}_i^o$, is given by

$$\overline{g}_i^o = \overline{h}_i - T\overline{s}_i^o. \tag{2.22}$$

The mixture specific internal energy, e, and enthalpy, h, are calculated using the specific internal energies or enthalpies of the species,

$$e = \sum_{i=1}^{N} Y_i e_i = \sum_{i=1}^{N} \left(Y_i h_i\right) - \frac{p}{\rho}, \tag{2.23}$$

$$h = \sum_{i=1}^{N} Y_i h_i. \tag{2.24}$$

In order to obtain the mixture temperature from either the mixture specific internal energy or enthalpy, an iterative procedure utilizing a Newton root-finding technique adapted from Press et al. [109] is used.

As briefly alluded to in Section 2.1, a chemical reaction interaction consisting of J reactions and N species can be represented in a general form as

$$\sum_{i=1}^{N} \nu'_{ij}\chi_i \rightleftharpoons \sum_{i=1}^{N} \nu''_{ij}\chi_i, \tag{2.25}$$

where χ_i is the chemical symbol of i^{th} species and $\rightleftharpoons$ represents the possibility of reversible reactions. Each of these reactions can be expressed as two parts; the first being a forward reaction and the other a reverse reaction. The overall reaction rate of the j^{th} reaction adopted is one of the law of mass action [4, 6, 41, 67, 110] and is given by

$$\mathsf{r}_j = k_j \left(\prod_{i=1}^{N} \left(\rho \frac{Y_i}{\overline{M}_i} \right)^{\nu'_{ij}} - \frac{1}{K_j^c} \prod_{i=1}^{N} \left(\rho \frac{Y_i}{\overline{M}_i} \right)^{\nu''_{ij}} \right), \tag{2.26}$$

where k_j is the Arrhenius kinetic rate and K_j^c the equilibrium constant for the j^{th} reaction. The Arrhenius kinetic rate of the j^{th} reaction is given by

$$k_j = a_j T^{\beta_j} \exp\left(\frac{-\overline{E}_j}{\mathcal{R}T} \right). \tag{2.27}$$

In Equation (2.27), a_j, β_j, and $\overline{E}_j$ are the collision frequency factor, the temperature-dependency exponent, and activation energy of the j^{th} reaction, respectively. Moreover, the equilibrium constant for the j^{th} reaction is calculated as

$$K_j^c = \left(\frac{p^o}{\mathcal{R}T} \right)^{\sum_{i=1}^{N} \nu_{ij}} \exp\left(\frac{-\sum_{i=1}^{N} \overline{g}_i^o \nu_{ij}}{\mathcal{R}T} \right). \tag{2.28}$$

In the certain reactions, a third body, M, is needed for the reaction to proceed. In this case, the concentration of the third body must be included in the reaction rate;

thus, Equation (2.26) is modified for the j^{th} reaction as

$$\mathsf{r}_j = \left(\sum_{i=1}^{N} \alpha_{ij} \left(\rho \frac{Y_i}{\overline{M}_i}\right)\right) \left(k_j \left(\prod_{i=1}^{N} \left(\rho \frac{Y_i}{\overline{M}_i}\right)^{\nu'_{ij}} - \frac{1}{K_j^c} \prod_{i=1}^{N} \left(\rho \frac{Y_i}{\overline{M}_i}\right)^{\nu''_{ij}}\right)\right), \tag{2.29}$$

where α_{ij} is the third body collision efficiency coefficient of the i^{th} specie for the j^{th} reaction. If all species have the same efficiency as third bodies, then α_{ij} equals unity for all species. However, some species may contribute more and thus, α_{ij} may differ from unity and vary from specie to specie in the j^{th} reaction.

In order to complete the system for the realistic detailed model, the diffusive transport relations adopted in this work were chosen following Bird et al. [8]. The diffusive mass, momentum, and energy transport relations are given as

$$\mathbf{j}_i = -\frac{D_i^T \nabla T}{T} + \rho \sum_{\substack{k=1 \\ k \neq i}}^{N} \frac{\overline{M}_i D_{ik} Y_k}{\overline{M}} \left(\frac{\nabla y_k}{y_k} + \left(1 - \frac{\overline{M}_k}{\overline{M}}\right) \frac{\nabla p}{p}\right), \tag{2.30}$$

$$\boldsymbol{\tau} = \mu \left(\nabla \mathbf{u} + (\nabla \mathbf{u})^T - \frac{2}{3} (\nabla \cdot \mathbf{u}) \mathbf{I}\right), \tag{2.31}$$

$$\mathbf{q} = -\mathsf{k} \nabla T + \sum_{i=1}^{N} \mathbf{j}_i h_i - \mathcal{R} T \sum_{i=1}^{N} \frac{D_i^T}{\overline{M}_i} \left(\frac{\nabla y_i}{y_i} + \left(1 - \frac{\overline{M}_i}{\overline{M}}\right) \frac{\nabla p}{p}\right), \tag{2.32}$$

where D_i^T is the thermal diffusion coefficient for the i^{th} specie, D_{ik} the multi–component diffusion coefficient between the i^{th} and k^{th} species, μ the dynamic viscosity of the mixture, and k the isotropic thermal conductivity of the mixture. The mixture dynamic viscosity is function of the temperature and molecular composition and is evaluated using the Wilke formula [167]

$$\mu = \sum_{i=1}^{N} \frac{y_i \mu_i}{\sum_{k=1}^{N} y_k \Phi_{ik}}, \tag{2.33}$$

$$\Phi_{ik} = \frac{1}{\sqrt{8}} \left(1 + \frac{\overline{M}_i}{\overline{M}_k}\right)^{\frac{1}{2}} \left(1 + \left(\frac{\mu_i}{\mu_k}\right)^{\frac{1}{2}} \left(\frac{\overline{M}_k}{\overline{M}_i}\right)^{\frac{1}{4}}\right)^2, \tag{2.34}$$

where μ_i is the dynamic viscosity for the i^{th} specie. The species dynamic viscosities are evaluated using a p order polynomial fit of the logarithm of the mixture temperature

$$\ln \mu_i = \sum_{k=0}^{\mathsf{p}} b_{ki} \left(\ln T\right)^k, \tag{2.35}$$

where b_{ki} are the polynomial coefficients for the i^{th} specie provided by the `TRANSPORT` database [62]. Note that this polynomial fit could be easily cast into a form using $\left(\ln\left(T/T_o\right)\right)^k$ and $\ln\left(\mu_i/\mu_{i_o}\right)$ such that the coefficients could be dimensionless. The remaining three diffusion coefficients, D_i^T, D_{ik}, and k are functions of the molecular composition and thermodynamic state and are obtained from the solution of a linear system defined by the block $\mathsf{L}-$matrix system [23, 62, 86]. For more details about the calculation of these transport coefficients and the $\mathsf{L}-$matrix system, see Appendix A.

Equation (2.30) is an extended Fick's law which consists of driving influences: 1) the temperature diffusion, commonly referred to as the Soret effect, 2) the material diffusion, and 3) the pressure diffusion. The viscous stress tensor, $\boldsymbol{\tau}$, in Equation (2.31) obeys a Newtonian stress-strain rate relation under Stokes' hypothesis. Therefore, from now on the dynamic viscosity will be referred to as viscosity. Additionally, Equation (2.32) is an extended Fourier's law. This extended Fourier's law consists of the heat flux due to heat diffusion, mass diffusion, and the DuFour effect due to the pressure and material gradients. The forms of both Fourier's and Fick's laws are appropriate for a mixture of ideal gases, as detailed in a derivation by Merk [86] and summarized by Kee et al. [62], where additional references can be found. In the detailed kinetics model chosen here, the diffusive transport coefficients are evaluated using the `TRANSPORT` package [62] and the mixture and reaction properties are evaluated with the `CHEMKIN` package [63].

It can be argued that for polyatomic gases, *e.g.* N_2, H_2O, and H_2O_2, other more complex diffusive relations may be more representative. An example of such a model is one that does not satisfy Stokes' hypothesis. There are indications that in some pure polyatomic gases that the second coefficient of viscosity becomes important [153, 154]. As indicated by Chapman and Cowling [12] and more recently by Gad-el-Hak [36], there is considerable amount of scatter in the experimental data for such coefficients. Moreover, there could be non-equilibrium effects that may in fact become important inside shock and detonation waves. However, the models for these effects can have drastically more complicated forms as demonstrated in Müller and Ruggeri [91]. As such the inclusion of such effects would make the early examination of diffusive processes on detonations exceedingly more complex and are thus left for future investigations.

2.3 Simplified Model

Now, a simplified version of the detailed model is derived by adopting several assumptions. The first assumption is to consider only a single reaction in the model that is irreversible, such that the reactant goes to product, $\mathsf{R} \rightarrow \mathsf{P}$, where R and P are the reactant and product, respectively. Secondly, the reactant and product have identical molecular masses, $\overline{M}_{\mathsf{R}} = \overline{M}_{\mathsf{P}}$. Therefore, the mixture molecular mass remains constant, $\overline{M} = \overline{M}_{\mathsf{R}} = \overline{M}_{\mathsf{P}}$, and thus, the mole and mass fractions are the identical, $y_{\mathsf{R}} = Y_{\mathsf{R}}$ and $y_{\mathsf{P}} = Y_{\mathsf{P}}$. Thirdly, the Soret effects is neglected so thermal diffusion coefficients are set to zero, $D^T_{\mathsf{R}} = D^T_{\mathsf{P}} = 0$. Additionally, both the reactant and product are calorically perfect ideal gases and have identical specific heats, $c_{p_{\mathsf{R}}} = c_{p_{\mathsf{P}}} = c_p = c$, where c_p is the mixture specific heat at constant pressure and c a constant.

Under these assumptions, the model reduces significantly. From here, the mass fraction of the reactant and product will be given by $1 - \lambda$ and λ, respectively. The mass diffusion transport relations, Equation (2.30), reduce to

$$\mathbf{j}_\lambda = -\rho D_\lambda \nabla \lambda, \tag{2.36}$$

where D_λ is the mass diffusion coefficient of the mixture. Likewise, the energy diffusion transport relation reduces to

$$\mathbf{q} = -\mathsf{k} \nabla T + \rho D_\lambda q_r \nabla \lambda, \tag{2.37}$$

where $q_r = h^f_{\mathsf{R}} - h^f_{\mathsf{P}}$ is the heat release of the reaction. Furthermore, the mixture specific internal energy, Equation (2.23), becomes

$$e = \frac{p}{\rho\left(\gamma - 1\right)} - q_r \lambda, \tag{2.38}$$

by assuming that $h^f_{\mathsf{R}} = c_{p_{\mathsf{R}}} T^o$. In Equation (2.38) γ is the ratio of specific heats, and as the specific heats are constant, the ratio remains constant. Lastly, as the single reaction is irreversible, the molar production rate per unit volume of λ can written as

$$\dot{\omega}_\lambda = \frac{\rho}{\overline{M}} \left(1 - \lambda\right) a T^\beta \exp\left(\frac{-\overline{E}}{\mathcal{R} T}\right). \tag{2.39}$$

CHAPTER 3

PULSATING DETONATIONS WITH ONE STEP KINETICS

3.1 Introduction

In this chapter, a one-dimensional investigation of the long time dynamics of a detonation described by the standard one step model, first studied in the inviscid limit [28, 29] is performed. Much of this chapter is drawn from Romick et al. [120]. The aim is to obtain a better understanding of the effects of diffusive processes on pulsating detonations. The detonation pressure traces are examined in both temporal and frequency domains. Additionally, a study comparing shock-capturing and shock-fitting techniques in the inviscid limit is presented.

The chapter is organized as follows. In Section 3.2, the mathematical model is presented, followed by a description of the computational method. The convergence of the period-doubling bifurcation points is shown to be in agreement with the general theory of Feigenbaum [32], and diffusion is seen to have a generally stabilizing effect on detonation dynamics. This is followed in Section 3.3.3 by a discussion of the evolution of the frequency decomposition of the long time detonation pressure trace as activation energy is varied. Likewise, Section 3.3.4 discusses how the half-reaction length varies temporally versus activation energy. Lastly, the rate of convergence of the solutions for the computational method utilized and their independence from the computational method is presented.

3.2 Formulation

In order to reduce the computational cost, a reference frame moving at a constant velocity, D, was chosen. It was selected to be the CJ wave speed which is the average wave speed of the detonations.

3.2.1 Mathematical Model

The model equations adopted in this chapter are the one-dimensional version of Equations (2.1)-(2.4). The diffusive transport relations taken here are Equations (2.36), (2.31), and (2.37) for mass, momentum, and energy diffusion, respectively. Additionally, the equations of state are given by Equations (2.5) and (2.38). Lastly, to make a direct comparison with the previous work the molar production rate, Equation (2.39), is modified by a Heaviside function. This forces the downstream ambient conditions to remain constant at all times, rather than having the reaction progress variable minutely increasing over time. Therefore, the governing equations are taken as:

$$\frac{\partial \rho}{\partial t} + \frac{\partial}{\partial x}\left(\rho\left(u - D\right)\right) = 0, \tag{3.1}$$

$$\frac{\partial}{\partial t}\left(\rho u\right) + \frac{\partial}{\partial x}\left(\rho u\left(u - D\right) + p - \frac{4}{3}\mu\frac{\partial u}{\partial x}\right) = 0, \tag{3.2}$$

$$\begin{aligned}\frac{\partial}{\partial t}\left(\rho\left(e + \frac{u^2}{2}\right)\right) + \frac{\partial}{\partial x}\Bigg(\rho\left(e + \frac{u^2}{2}\right)\left(u - D\right) + pu \\ -\mathsf{k}\frac{\partial T}{\partial x} + \rho D_\lambda q_r\frac{\partial \lambda}{\partial x} - \frac{4}{3}\mu\frac{\partial u}{\partial x}u\Bigg) = 0,\end{aligned} \tag{3.3}$$

$$\frac{\partial}{\partial t}\left(\rho\lambda\right) + \frac{\partial}{\partial x}\left(\rho\lambda\left(u - D\right) - \rho D_\lambda\frac{\partial \lambda}{\partial x}\right) = \rho\left(1 - \lambda\right)aT^\beta\exp\left(\frac{-\overline{E}}{\mathcal{R}T}\right)H\left(p - p_s\right), \tag{3.4}$$

where $H\left(p - p_s\right)$ is the Heaviside function which suppresses the reaction when $p < p_s$ where p_s is a selected pressure.

3.2.2 Computational Methods

The unsteady dynamics of the one-dimensional detonation are predicted using a temporally explicit point-wise method of lines approach. The majority of the calculations presented here use the following method. The spatial discretization of the advective terms was accomplished using a combination of a standard fifth order Weighted Essentially Non-Oscillatory (WENO) and Lax-Friedrichs schemes in the manner of Xu et al. [173]; the diffusive terms were evaluated using sixth order central differences. Temporal integration is accomplished using a third order Runge-Kutta method.

In addition to the previously listed computational method used for viscous shock–capturing, in Section 3.3.1, the method of [47] for shock-fitting is used. Likewise, in Section 3.3.4, an Runge-Kutta-Legendre technique developed by Meyer et al. [87] is used. It makes use of a second-order operator split, but allows for larger explicit time steps.

A standard technique of code verification, the method of manufactured solutions [119], was performed, and a fifth order convergence rate was predicted as the grid was refined demonstrating that the code correctly solves the governing equations. In Section 3.3.6, the predictions of this scheme are compared to those from a simple sixth order central difference of the advective terms. It will be seen that ordinary central differencing suffices to describe detonation dynamics. Additionally, convergence in the presence of the Heaviside function is also discussed in Section 3.3.7.

All calculations in Sections 3.3.1 and 3.3.2 were performed in a single processor environment on an AMD 2.4 GHz processor with 512 kB cache. For a typical viscous calculation of 2.0 μs, the computational time required was two days. Some calculations presented in Section 3.3.2 took as long as eight days for full relaxation. A discussion of other computational times will be presented in Section 3.3.4.

3.2.3 Problem Parameters

As discussed in [47] in the inviscid limit, the activation energy plays a large role in determining the stability of the system. Moreover, the rate constant, a, merely introduces a length scale, the half-reaction length, $L_{1/2}$, (the distance between the inviscid shock and the location at which $\lambda = 1/2$). By fixing $L_{1/2}$ and thus allowing a to vary, the effect of diffusion on the system can be explored.

Here, the ambient state is given by the ambient density, $\rho_o = 1$ kg/m^3, and the ambient pressure, $p_o = 1$ atm, and the reaction progress variable, $\lambda_o = 0$. The following parameters will be used in this study, $q_r = 5066250$ m^2/s^2, $\gamma = 6/5$, $\beta = 0$, $c_p = \gamma\mathcal{R}/\left(\overline{M}\left(\gamma-1\right)\right) = 1000$ J/(kg K) meaning $\overline{M} = 49.9$ g/mole, and $p_s = 1.97$ atm. The selection of p_s is arbitrary, because there is minimal effect on the system over the range of 1.01 atm to 9.97 atm. With this heat release, ratio of specific heats, and ambient state, the CJ detonation velocity, D_{CJ}, for the inviscid problem is

$$D_{CJ} = \sqrt{\gamma\frac{p_o}{\rho_o} + \frac{q_r\left(\gamma^2-1\right)}{2}} + \sqrt{\frac{q_r\left(\gamma^2-1\right)}{2}} = 2167.56 \text{ m/s}. \tag{3.5}$$

A range of activation energies is explored for the long term behavior, $\overline{E} \in [2431800, 4053000]$ m^2/s^2. The values for γ and q_r were chosen to compare directly with the previous work of [47] in the inviscid limit. The energy release of the reaction scaled by the ambient pressure and density, $q_n = 50$, identical to that used in the previous study. Likewise, the activation energies will be presented in dimensionless form; thus, $E \in [24, 40]$.

Selecting the diffusion coefficient, $D_\lambda = 10^{-4}$ m^2/s, thermal conductivity, $\mathsf{k} = 10^{-1}$ W/(m K), and viscosity, $\mu = 10^{-4}$ N s/m^2 yields the Lewis, $Le = \mathsf{k}/\left(\rho_o c_p D_\lambda\right)$, Prandtl, $Pr = \left(c_p\mu\right)/\mathsf{k}$, and Schmidt, $Sc = \mu/\left(\rho_o D_\lambda\right)$, numbers to have a value of unity when evaluated at the ambient density. These diffusion parameters are within an order of magnitude of those of a slightly elevated temperature gas. Now by using simple dimensional analysis of advection and diffusion parameters ($U = 1000$ m/s is chosen as a typical velocity scale) gives rise to an approximate length scale of mass diffusion, $D_\lambda/U = 10^{-7}$ m, and likewise, for momentum and energy diffusion $\mu/\rho_o/U = 10^{-7}$ m, and $\mathsf{k}/\rho_o/c_p/U = 10^{-7}$ m. Therefore, because all the diffusion length scales are the same, this scale will be denoted as $L_\mu = 10^{-7}$ m. Using these parameters allows for the interaction of diffusion and reaction effects to be studied and induces a set of scales similar to those given in reactive Navier-Stokes models with detailed chemical kinetics. Unless otherwise stated, the calculations presented are for a ratio of $L_\mu/L_{1/2} = 1/10$, such that $L_{1/2} = 10^{-6}$ m, which is similar to the finest reaction length scale of hydrogen-air detonations.

The coarsest scales in hydrogen-air detonations are much larger than the chosen $L_{1/2}$; as shown by [108], a mixture of hydrogen-air at ambient conditions of atmospheric pressure has an induction zone of approximately 2×10^{-4} m. In the more realistic detailed kinetics systems, the main heat release occurs over the coarse length scales. Thus, it is recognized that the chosen length scale on which the heat is released is much finer than expected in a realistic physical system; the main reason for this choice is to lessen the stiffness of the system so as to enable a tractable computation of a fully resolved multiscale detonation. In Chapter 4, results will be presented where no such compromise is used for fully resolved viscous hydrogen-air detonations.

Unless otherwise stated, the simulations were initialized with the inviscid ZND solution in a reference frame traveling at the CJ speed. This choice of reference frame speed was made to reduce the length of the computational domain and thus, further reduce the computational cost of the simulations. Simulations are integrated in time to determine the long time behavior.

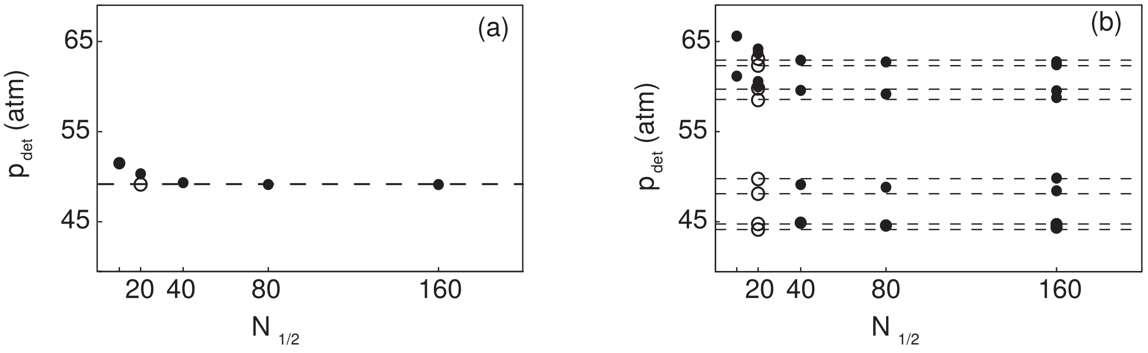

Figure 3.1. Peak inviscid detonation pressures versus $N_{1/2}$ for (a) $E = 26.64$, (b) $E = 27.82$. Shock-capturing predictions are given by the filled circles and the shock-fitting $\left(N_{1/2} = 20\right)$ prediction is represented by open circles and dashed lines.

3.3 Results and Discussion

In this section, the reactive Euler equations are first considered, and detrimental effects of shock-capturing on predicting the convergence of unstable inviscid detonations are examined. These defects are remedied by the addition of physical diffusion. In addition to examining the temporal behavior of the detonation, the frequency domain is also investigated. Furthermore, the way the half-reaction zone length zone varies in time is examined. Lastly, the unsteady solutions to the reactive Navier-Stokes equations are shown to converge, and it is demonstrated that ordinary central difference schemes can perform as well as more complex schemes such as WENO.

3.3.1 Inviscid Shock-Capturing versus Shock-Fitting

In addition to using the Euler equations for modeling detonations, the use of shock-capturing techniques and moving reference frames is also common. Quirk [111] reports that when using the Euler equations with any shock-capturing technique, a shock moving slowly relative to the numerical grid will have low frequency numerical perturbations. These low frequency perturbations can be lessened by refining the grid. To avoid this issue completely, [47] used a high accuracy shock-fitting technique to predict the behavior of the one step detonation. This method limits the artificial viscosity to negligible levels and thus, enables an accurate prediction with the number of points within the so called half-reaction zone width, $N_{1/2} = 20$. For an activation energy of $E = 26.64$, a simple period-1 limit cycle detonation is predicted using shock-fitting; using shock-capturing with the same resolution, the predicted behavior of a period-1 detonation is in agreement with that of shock-fitting with a relative difference of the peak pressure of 2.1%. Increasing the resolution lessens this relative difference as shown in Figure 3.1(a). At $E = 27.82$, shock-fitting predicts a period-8 limit cycle detonation, whereas shock-capturing, using the higher resolution of 40 points in the half-reaction length, predicts a period-4 detonation. This difference can be reconciled by increasing the resolution, demonstrated in Figure 3.1(b). The present study, in good agreement with [128], found that $N_{1/2} > 80$ was needed in this regime. The resolution requirement to accurately predict the correct dominant behavior including the correct number of local maxima may be even more stringent for detonations with more local maxima, as seen in [93]. This suggests that numerical diffusion is playing an important role in determining the behavior of the system at lower resolutions. A more in-depth analysis of the resolutions needed to capture the proper dynamics of the lead shock and trailing reaction wave is given in Section 3.3.4.

3.3.2 Effect of Physical Diffusion

The plausible yet erroneous predictions due to the inherent numerical diffusion in the model can be remedied by increasing the resolution of the scheme. However, for instabilities with many local maxima, the necessary resolution tends towards infinity for the inviscid model. A preferable approach is to include explicit physical diffusion and so introduce a cutoff length scale below which physical diffusion properly serves to dampen oscillations.

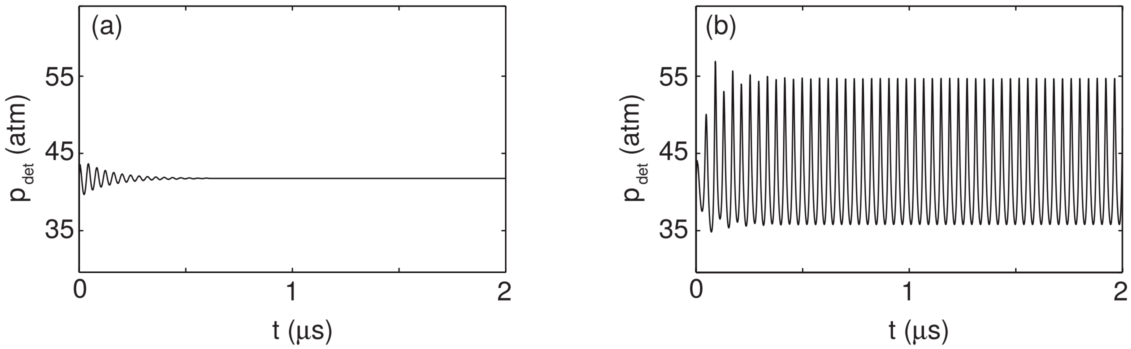

Figure 3.2. Detonation pressure versus time, $L_\mu/L_{1/2} = 1/10$, (a) $E = 26.64$, stable diffusive detonation, (b) $E = 29.00$, period-1 diffusive detonation.

3.3.2.1 Stability Limit

In the inviscid case, linear stability analysis by [68] revealed that for $E < 25.26$, the steady ZND wave is linearly stable and is otherwise linearly unstable. The activation energy at this stability boundary is labeled E_0. Henrick et al. [47] numerically found the stability limit, for the inviscid case, at $E_0^i = 25.265 \pm 0.005$. Here, a diffusive case well above the inviscid stability limit was examined, $E = 26.64$, which [47] found to relax to a period-1 limit cycle for an inviscid simulation. In the diffusive simulation, it can be seen in Figure 3.2(a) that there is no limit cycle behavior, and the detonation predicted by diffusive theory is in fact a stable steadily propagating wave. The stability boundary for the diffusive case was found at $E_0^d \approx 27.14$. A period-1 limit cycle may be realized in the diffusive case by increasing the activation energy above E_0^d; an example is shown in Figure 3.2(b) with an activation energy of $E = 29.00$.

It is expected that the onset of instability would be delayed more as the scale of diffusion approaches that of reaction. Figure 3.3 shows precisely this behavior. Furthermore, as the two scales approach one another, the onset of instability is delayed significantly in comparison with the inviscid case.

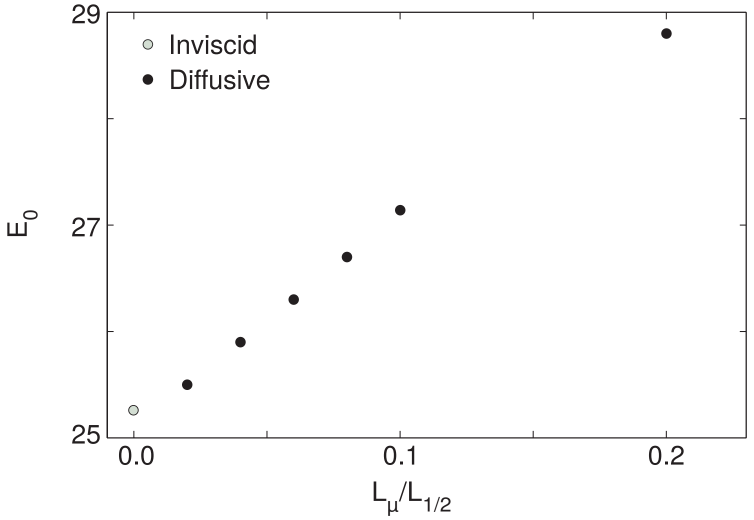

Figure 3.3. The value of the stability limit, E_0 versus the diffusion length scale, $L_\mu/L_{1/2}$.

3.3.2.2 Period Doubling and Transition to Chaos

As the activation energy increases, more complicated dynamics occur at long times. A period-doubling behavior and transition to chaos for unstable detonations are found to be remarkably similar to that predicted by the simple logistic map studied by May [83]. The activation energy at which the behavior switches from a period-2^{n-1} to a period-2^n solution is denoted as E_n, for $n \geq 1$. As predicted by [47, 93, 128], transition to a period-2 oscillation occurs at $E_1^i \approx 27.2$ for the inviscid case. In the diffusive case, it was found instead at $E_1^d \approx 29.32$. Figure 3.4(a) shows the time history of the detonation pressure for a slightly higher activation energy, $E = 29.50$. In the long time limit, there are two distinct relative maxima, $p \approx 60.370$ atm and $p \approx 52.879$ atm. Increasing further to $E = 29.98$, another period-doubling is realized, and a period-4 oscillating detonation is achieved as seen in Figure 3.4(b). The bifurcation points for both models are listed in Table 3.1

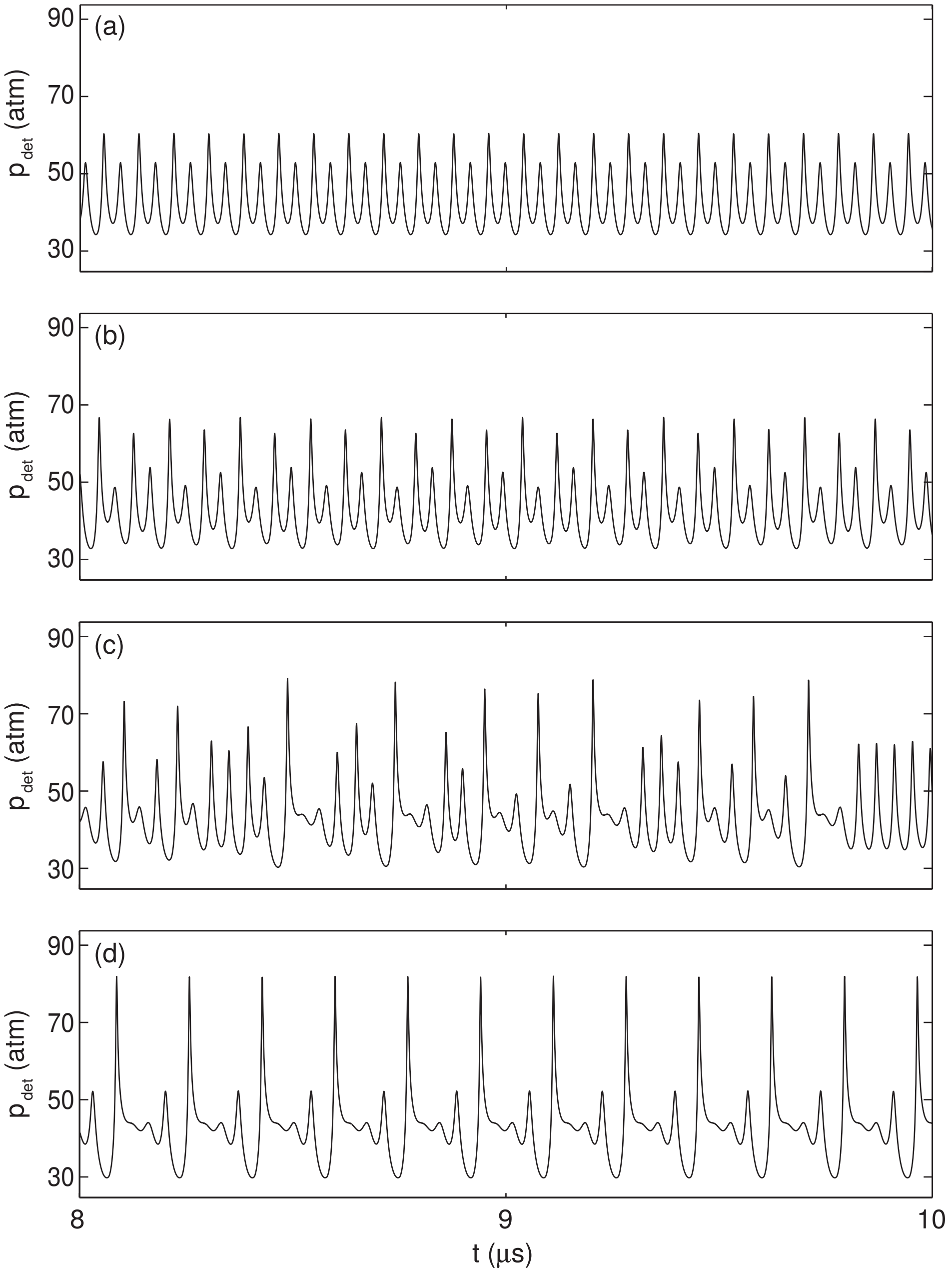

Figure 3.4. Detonation pressure versus time, $L_\mu/L_{1/2} = 1/10$:
(a) $E = 29.50$, period-2, (b) $E = 29.98$, period-4, (c) $E = 30.74$, chaotic,
(d) $E = 30.86$, period-3.

TABLE 3.1

BIFURCATION POINTS AND APPROXIMATION TO FEIGENBAUM'S CONSTANT

	Inviscid	Inviscid	Diffusive	Diffusive
n	E_n^i	δ_n^i	E_n^d	δ_n^d
0	25.2650	-	27.14	-
1	27.1875	3.86	29.32	3.89
2	27.6850	4.26	29.88	4.67
3	27.8017	4.66	30.00	-
4	27.82675	-	-	-

Numerically determined for both inviscid and diffusive detonations.

along with approximations for Feigenbaum's constant, δ_∞ :

$$\delta_\infty = \lim_{n\to\infty} \delta_n = \lim_{n\to\infty} \frac{E_n - E_{n-1}}{E_{n+1} - E_n}. \tag{3.6}$$

Feigenbaum predicted $\delta_\infty \approx 4.669201$. Diffusive and inviscid models predict δ_∞ well.

3.3.2.3 Chaos and Order

Figure 3.5(a) gives the bifurcation diagram for the case studied by [47] in the inviscid limit using a shock-fitting algorithm with negligible numerical diffusion. Figure 3.5(b) gives the diffusive analog. It was constructed by sampling 351 points with $E \in [25, 32]$, with a spacing of $\Delta E = 0.02$. Simulations were integrated to $t = 10$ μs, and relative maxima in detonation pressure were recorded for $t \geq 7.5$ μs. In the diffusive case, the period-doubling bifurcations occur up to $E_\infty^d \approx 30.03$. Beyond this point, there exists a region that is densely populated in relative maxima which is most likely a chaotic regime. Increasing the activation energy yet further, one comes

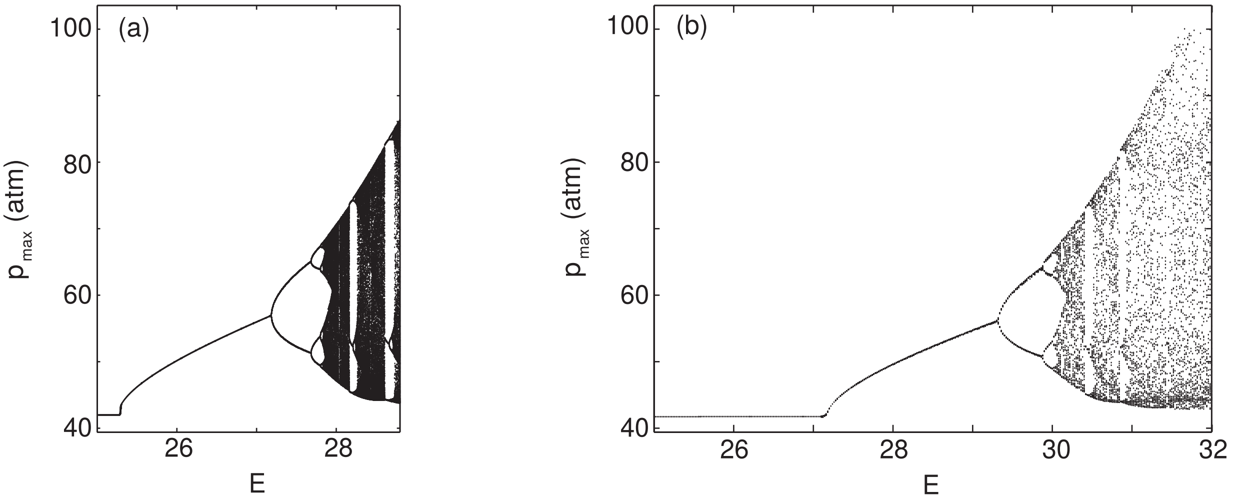

Figure 3.5. Comparison of numerical bifurcation diagrams: (a) inviscid detonation with shock-fitting, (b) diffusive detonation with $L_\mu/L_{1/2} = 1/10$.

to regions with a small number of oscillatory modes with periods of 3, 5, and 6. A chaotic detonation is shown in Figure 3.4(c). Yet, at a higher activation energy, a solution with period-3 is found, which is shown in Figure 3.4(d).

3.3.3 Harmonic Analysis

It can be useful to understand how the energy of the pulsation cycle is distributed. This is difficult to discern from the detonation pressure versus time plots. Furthermore, it can be difficult to discern if artificial viscosity or physical viscosity affects the frequency from these type of plots. To elucidate some of these ideas, harmonic analysis was used to examine the detonation pressure-time series away from initialization. This type of analysis can reveal important information about an individual signal, such as in which frequency is the majority of the energy being transmitted. It is also a powerful tool to analyze the differences and similarities between two signals.

To further clarify this issue, the power spectral density (PSD) is used. The PSD of a signal describes how the variance (or power) is distributed in frequency, and it is real-valued for any real signal. It can be used to reveal possible periodicities in a complex signal. The variation between two signals can also be studied using PSD by making a comparison between the two spectra. The PSD is simply defined as the Fourier Transform of the auto-correlation of a signal [7, 43]. Moreover, it can be written as the magnitude squared of the Fourier transform of the signal by using the Wiener-Khinchin theorem. For the work here, the discrete one-sided mean-squared amplitude PSD is used. The single-sided PSD is chosen so that the aliasing effect at high frequencies could be bypassed. This normalization is chosen such that, as Parseval's theorem states [100], the sum of Φ_d to equal the mean-squared amplitude of the discrete detonation pressure signal, where $\Phi_d(\nu_k)$ is the discrete PSD of the detonation pressure-time signal at frequency, ν_k. For more details on how the PSD is calculated see Appendix B.

The PSDs presented are the power-frequency spectrum for the detonation pressure time signal in decibels. The steady ZND detonation pressure has been used to non-dimensionalize pressure. All results presented for the inviscid model were calculated using shock-fitting with 40 points in the half-reaction length.

In order to better understand the use of harmonic analysis, a brief review of the well-known results from linear stability of the inviscid model is given. From Lee and Stewart [68] and Sharpe [127], as well as others, it is known that the first unstable mode for a CJ detonation in one step kinetics, for the parameters studied here, occurs at an activation energy of $E \approx 25.265$. At any activation energy above this critical point, the steady-state detonation profile is unstable at long times. For example, at an activation energy of $E = 26.0$, linear stability theory predicts an unstable mode at the non-dimensional fundamental frequency of $\nu_o \approx 0.0879$ [47]. The frequency has been non-dimesionalized by $\sqrt{p_o/\left(\rho_o L_{1/2}^2\right)}$. At early times, the linear stability frequency and growth rates were matched well by [47]. Furthermore at this activation energy in the inviscid limit, a period-1 detonation is in fact predicted at long times [47, 93].

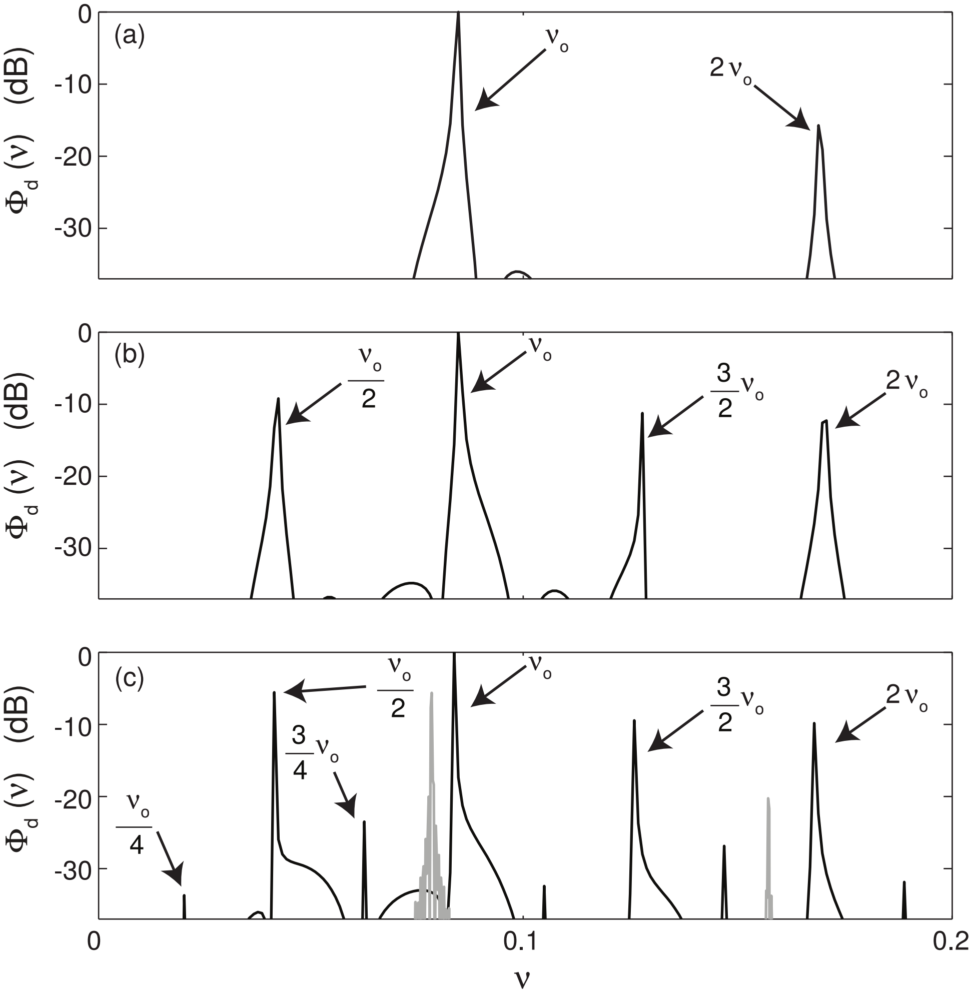

Figure 3.6. The PSD spectra in decibels of the long time behavior for (a) $E = 26.0$, (b) $E = 27.5$, (c) $E = 27.7$. The inviscid case is indicated by the black line and if present, the viscous case is indicated by the gray line.

Now, looking at the long time behavior at this activation energy in the frequency domain, it is clear from Figure 3.6(a) that nearly all of the energy is contained at a fundamental frequency, $\nu_o = 0.0849$. This fundamental frequency is also known as the first harmonic of the system. This is a relative difference of 3.41% versus the linear stability frequency. This difference is attributed to the saturation of nonlinear effects at long times. Additionally, the harmonics of the fundamental mode also contain energy of the detonation, though they show a power law decrease in energy carried.

Both [93] and [47] report a sub-harmonic bifurcation process in the inviscid limit; additionally Romick et al. [120] reports a similar behavior in the viscous case. This sub-harmonic bifurcation process is indicated by the appearance of lower frequencies developing as the activation energy is increased. As an example, for an activation energy of $E = 27.5$, a pulsating detonation with two distinct peaks in the detonation pressure-time signal is predicted. The inviscid PSD for this activation energy, which is shown in Figure 3.6(b), demonstrates the appearance of this sub-harmonic frequency. In fact these sub-harmonics are indicated by spikes at the odd multiples of $\nu_o/2$. The predicted fundamental frequency of $\nu_o = 0.0842$, is 6.23% larger relative to that predicted by linear stability of 0.0793. The nonlinear effect on the frequency has increased from the strictly period-1 detonation. Furthermore, it is manifested in the multi-mode nature of the detonation. As a brief aside, it should be noted that Massa et al. [80], who used an eigenvalue decomposition of perturbations to a multi-dimensional detonation wave in the one step model, found that the least stable perturbations occurred near this first sub-harmonic suggesting that even in multiple dimensions the dominant mechanism is similar to that seen in galloping case of one dimension.

At a slightly higher activation, $E = 27.7$, a period-4 detonation is predicted in the inviscid limit. This transition is indicated in the PSD spectrum by the appearance of a second sub-harmonic group as shown in Figure 3.6(c). This second set of sub-harmonics occur at the odd multiples of $\nu_o/4$. Furthermore, the first set of sub-harmonics now carries a more appreciable ratio of the energy.

As indicated earlier in Section 3.3.2, the addition of physical viscosity alters the long time behavior at a given activation energy. In addition to the changes in the time domain, there can be significant modifications of the behavior in frequency domain. At this activation energy of $E = 27.7$, the viscous PSD does not indicate any of the sub-harmonics predicted in the inviscid limit. Additionally, there is a shift in the fundamental frequency from 0.0839 in the inviscid case to 0.0787 in the viscous analog as shown in Figure 3.6(c). The addition of viscosity shifts the dominant frequency much closer to the prediction from linear stability theory of 0.0786. Moreover, there has also been a significant reduction in the amplitude of the peak in the spectrum. Note that here instead of the traditional definition of decibels $[10 \times \log_{10}(PSD/\max(PSD))]$, both spectra shown in Figure 3.6(c) have been scaled by the maximum of the inviscid spectrum so the magnitude of the different spectra would not be lost.

Figure 3.7 shows how the non-dimensional frequency spectra evolve versus the activation energy for the viscous case studied for $L_\mu/L_{1/2} = 1/10$. For detonation pressure time signals with deviations larger than 0.04 atm from the mean, the mean detonation pressure is subtracted for calculation of the PSDs. The strength of peaks are indicated by the shade of gray; the stronger the peak the darker the shade of gray is. The transition from a stable to an unstable detonation is indicated by the jump in the main frequency from 0 to approximately 0.0801. Within the region where the detonation pressure time signal has a single local maxima, the fundamental frequency shifts from 0.801 to 0.0771, which is the same trend that is predicted by linear stability theory. Moreover, as the activation energy increases, so does the energy ratio of the pulsations that higher harmonics of the fundamental frequency carry; this is indicated by the appearance of lines at $2\nu_o$, $3\nu_o$, and higher multiples.

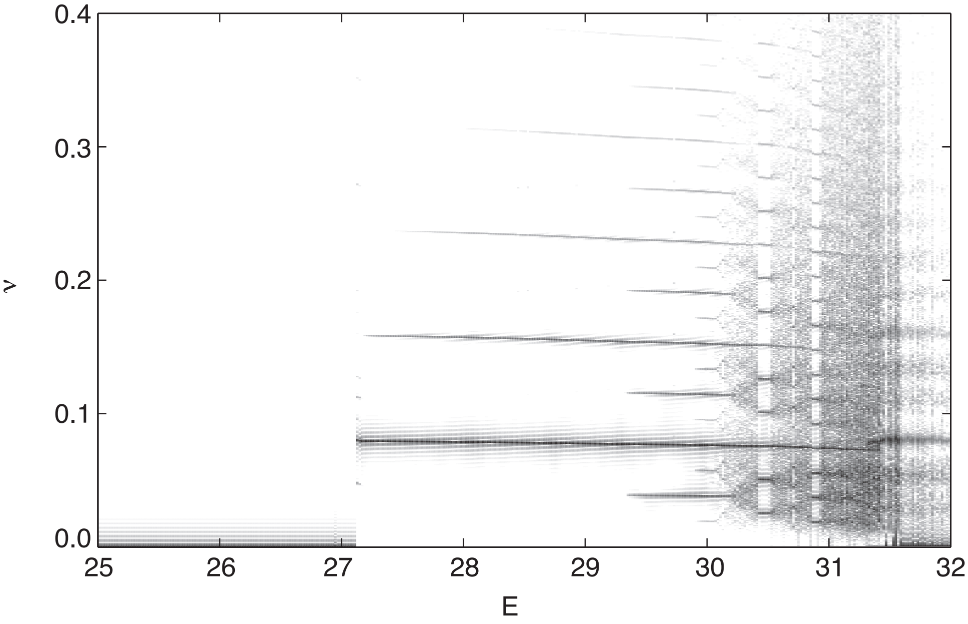

Figure 3.7. The bifurcation diagram of the non-dimensional frequency spectra for diffusive detonation with $L_\mu/L_{1/2} = 1/10$.

As mentioned previously, the second bifurcation is indicated by the appearance of sub-harmonic frequencies, which occurs at $E = 29.32$ in the viscous case studied here. In fact, the sub-harmonic frequency appears at $\nu_o/2 = 0.0382$. Furthermore, at the further bifurcations additional sub-harmonic frequencies begin to appear, at $\nu_o/4$ and $\nu_o/8$. Additionally, the fundamental frequency continues to shift to slightly lower frequencies; thus at $E = 30.00$, $\nu_o = 0.0756$.

After these sub-harmonic bifurcations, the behavior undergoes a transition to a detonation with many active frequencies, indicating most likely a chaotic detonation. Within likely chaotic domain, there are regions of order where only several frequencies are active; this is consistent with the local maxima in the detonation pressure bifurcation plot, shown in Figure 3.5(b). Even though there are many active modes, the fundamental frequency before this transition continues to carry a significant energy ratio.

Within in this region of likely chaotically propagating pulsating detonation, there are pockets of order. The largest of these ordered regions are for period-3 detonations, one pocket of order occurs near $E = 30.42$, and a second is near $E = 30.86$. These regions are indicated in the frequency spectra by the peaks at multiples of $\nu_o/3$ and $2\nu_o/3$. At the highest activation energies, there are many active modes though the strongest mode is near the zero frequency which is indicative of a detonation failing. This suggests that eventually the detonation becomes an uncoupled lead shock and a trailing reaction wave. This relationship between the lead shock and trailing reaction wave is discussed further for a range of activation energy in Section 3.3.4.

3.3.4 Variation in Half-Reaction Length

In this simple model of one step kinetics, the number of points in the steady $L_{1/2}$ is used as a standard reference for the resolution. However as briefly mentioned previously in Sections 3.3.1 and 3.3.3, there is a coupling between the lead shock and the reaction wave in a time-dependent calculation. Moreover, this means that the length from the leading shock-front to the location where the reaction progress variable, $\lambda = 1/2$, can vary in a time-dependent calculation. Fixing the strictly steady $L_{1/2} = 10^{-6}$ m by allowing a to vary as E varies in the inviscid limit, the evolution in the reaction zone length in a time-dependent calculation can be more easily studied. This examination gives insight why the resolution requirement to properly capture the detonation dynamics varies with the activation energy as demonstrated in Section 3.3.1.

At lower activation energies, the highly accurate shock-fitting technique of [47] can be used to predict the inviscid behavior and calculate the half-reaction zone length. The use of the shock-fitting technique also reduces the needed computational domain. Figure 3.8(a) shows the $x - t$ diagram in a reference frame traveling at the CJ speed for an inviscid stable detonation at $E = 25$. The location of $\lambda = 1/2$ is

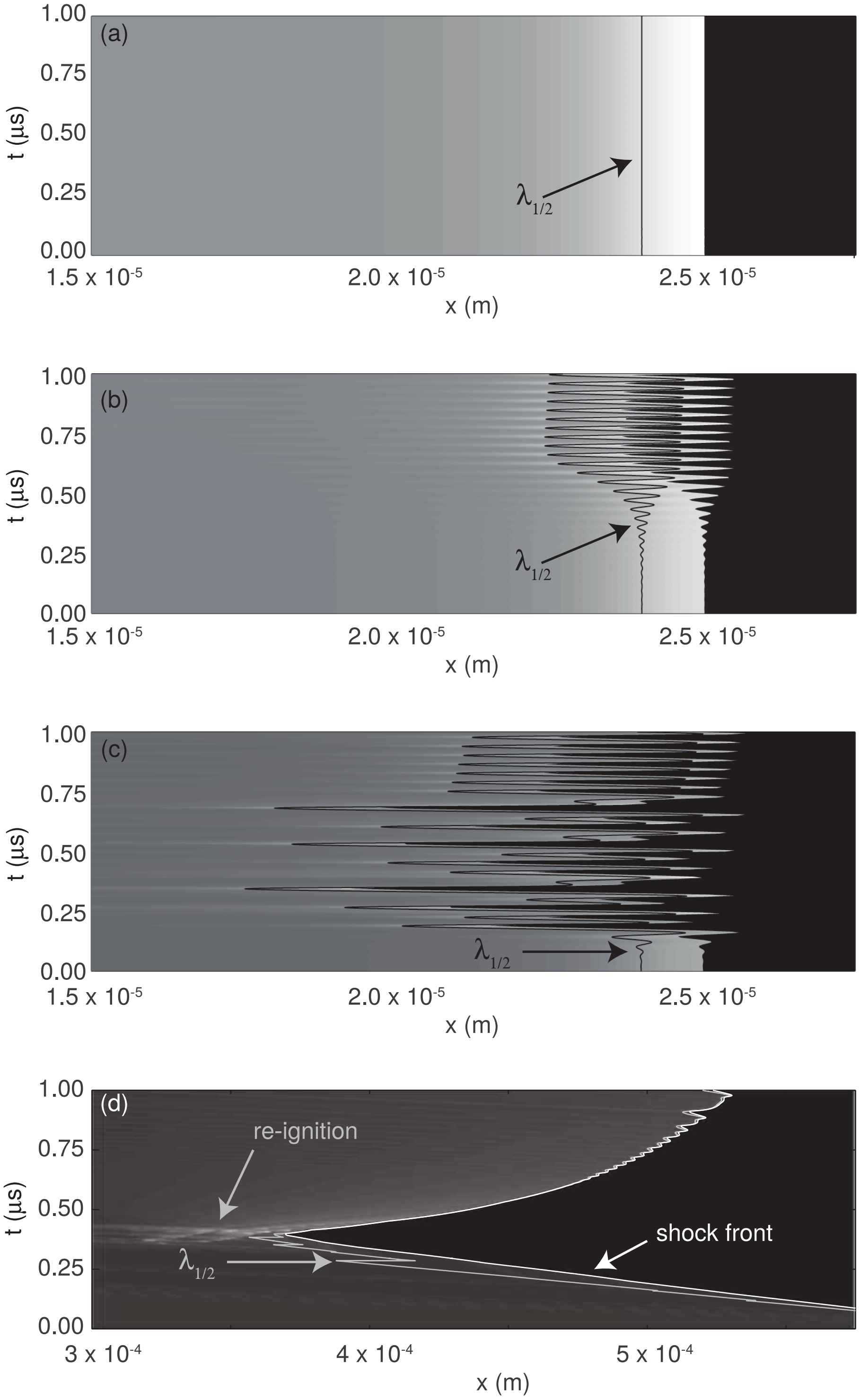

Figure 3.8. The $x - t$ diagrams of inviscid CJ detonations in a frame of reference traveling at the CJ speed for activation energies of (a) $E = 25$, (b) $E = 26$ (c) $E = 28$, (d) $E = 35$.

indicated by the line behind the shock front, and clearly, it stays at a constant distance behind the shock-front. Additionally, it is a stable steadily traveling detonation, which is consistent with the work of [47]. Examining an activation energy above E_0^i, a pulsating detonation is predicted, and Figure 3.8(b) show precisely this in an $x-t$ diagram. The half-reaction zone is also pulsating; however, it is slightly out of phase with the lead shock. Therefore, the half-reaction zone length evolves in time, with the minimum $L_{1/2_{min}} = 6.65 \times 10^{-7}$ m and the maximum $L_{1/2_{max}} = 1.355 \times 10^{-6}$ m. This yields a ratio between the maximum and minimum of 2.04. Now, for a higher activation energy, $E = 28$, a likely chaotic pulsating detonation is predicted. The $x-t$ diagram for this activation energy is shown in Figure 3.8(c). By this activation energy, the ratio has increased to 7.29 with $L_{1/2_{max}} = 2.18 \times 10^{-6}$ m and $L_{1/2_{min}} = 3.00 \times 10^{-7}$ m.

At even higher activation energies the shock-fitting technique can no longer be used. At an activation energy which is more representative of detailed mechanism for detonations [149], $E = 35$, the leading shock decouples from the trailing reaction wave. Figure 3.8(d) shows the detonation failing by decomposing into a weakened leading shock, contact discontinuity, and a rarefaction wave to the CJ state before the eventual re-ignition of the detonation. After re-ignition, the trailing reaction wave quickly reattaches the leading shock wave, leading to a strongly overdriven detonation and $L_{1/2_{min}} = 3.15 \times 10^{-8}$ m. At this high activation energy, the ratio of the maximum to minimum reaction zone lengths is 1524.

For greater comprehension of this process, several spatial profiles are shown in Figure 3.9. Figure 3.9(a) shows the initial ZND profile for pressure non-dimensionalized by the ZND shock pressure in black and the reaction progress variable in gray, zoomed at the shock front. After only 0.240 μs, the detonation has failed. The separation between the leading shock and the trailing reaction wave after this decoupling is shown Figure 3.9(b). Figure 3.9(c) shows the spatial profile after re-ignition, where

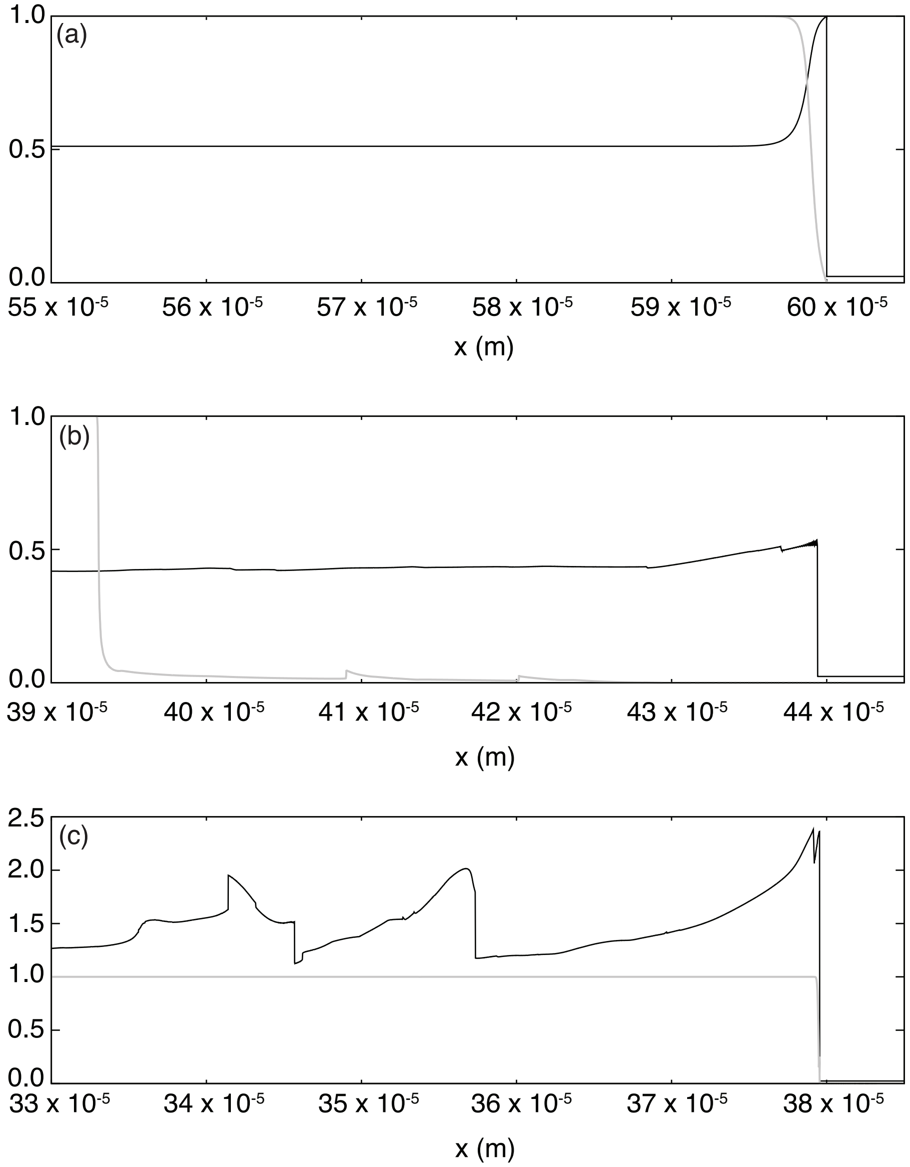

Figure 3.9. Spatial profiles for pressure non-dimensionalized by the ZND shock pressure (black line) and reaction progress variable (gray line) for an inviscid CJ detonation in reference frame traveling at the CJ speed for activation energy of $E = 35$ at (a) $t = 0$ μs, (b) $t = 0.240$ μs, and (c) $t = 0.415$ μs.

the half-reaction zone length is near its minimum at $t = 0.415\ \mu$s.

The maximum half-reaction zone length grows longer as the activation energy increases; likewise, the minimum half-reaction zone length becomes shorter. This means that as the activation energy increases, not only does the domain length of the calculation need to increase, but the resolution also must increase. Thus, the computational expense of the calculation does not increase linearly as activation energy increases.

An *a priori* bound for the longest half-reaction zone length can be obtained in this simple one step model by solving a Riemann problem between the ambient and CJ conditions. If inertial confinement is assumed, then it becomes an adiabatic, isochoric thermal auto-ignition problem behind the weakened leading shock and the governing equations reduce to

$$\frac{\partial \lambda}{\partial t} = (1-\lambda)\, a \exp\left(\frac{-\overline{E}}{(p/\rho)}\right), \tag{3.7}$$

$$\frac{p}{(\gamma-1)\,\rho} - q\lambda = c. \tag{3.8}$$

These can then be manipulated to get a time to auto-ignition,

$$t_{ign} = \int_0^{1/2} \frac{1}{a\,(1-\lambda)\exp\left(\frac{-E}{(p_S/\rho_S+(\gamma-1)q\lambda)}\right)} d\lambda, \tag{3.9}$$

where ρ_S, and p_S are the post-shock density and pressure, respectively. After the auto-ignition time is calculated it can be used in combination with the shock-speed, D_S, and the post-shock velocity, u_S, to calculate the length to auto-ignition,

$$L_{ign} = (D_S - u_S)t_{ign}, \tag{3.10}$$

which can be used as an approximation to the longest half-reaction zone length.

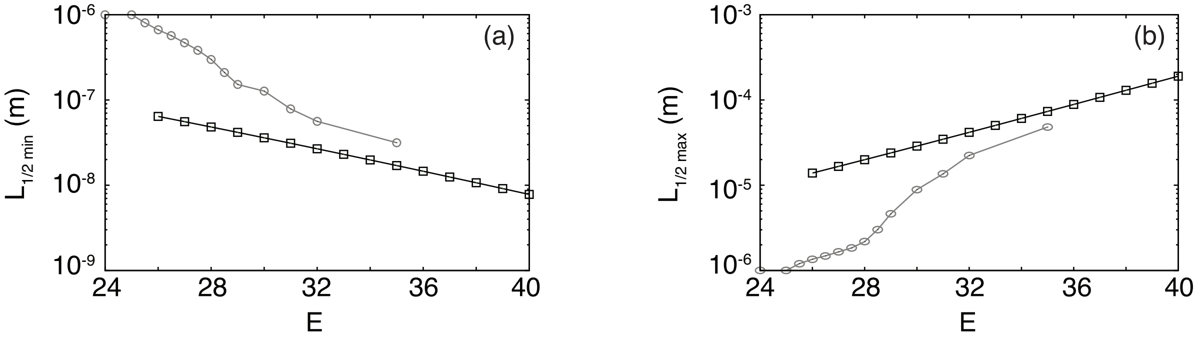

Figure 3.10. (a) Minimum half-reaction zone length and (b) maximum half-reaction zone length versus activation energy for inviscid calculations with the steady $L_{1/2} = 10^{-6}$ m (gray curve) and theoretical estimate (black curve).

Likewise, an *a priori* bound for the shortest half-reaction zone length can be obtained. As mentioned previously, after re-ignition the detonation becomes strongly overdriven, and at sufficiently high overdrives, the shocked temperature dominates the activation energy in the chemical reaction term. This causes the exponential in the Arrhenius kinetics to become approximately unity. Therefore, there is a specific overdrive at which the interaction between the rate of chemical reaction and the post-shock velocity yields a minimum $L_{1/2}$. Thus this overdrive and half-reaction zone length can be solved for numerically.

These theoretical bounds are compared with the values predicted directly from the inviscid calculations with the steady $L_{1/2} = 10^{-6}$ m in Figure 3.10. At activation energies where the predicted detonation behavior is unstable, the maximum half-reaction zone length begins to grow longer and eventually begins to approach the upper bound at sufficiently high activation energies as shown in Figure 3.10(a). Likewise, as shown in Figure 3.10(b), the minimum half-reaction zone length begins to follow the slope shown by the minimum bound. Additionally, as seen in Figure 3.11, the ratio of the maximum to minimum lengths begins to approach the ratio of the

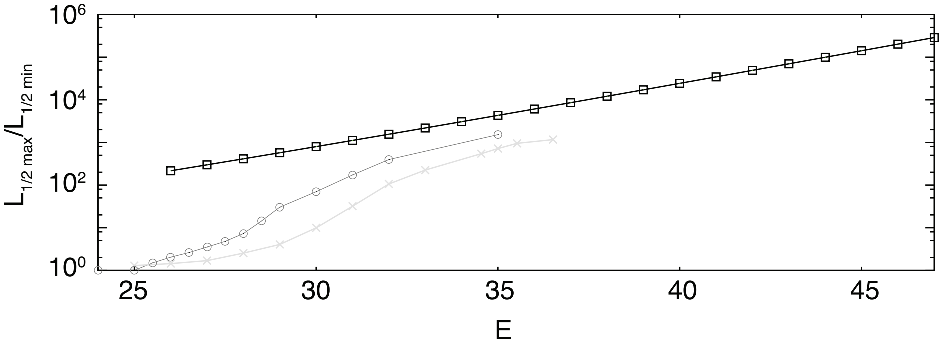

Figure 3.11. Ratio of the maximum to minimum half-reaction zone lengths versus activation energy for inviscid calculations with the steady $L_{1/2} = 10^{-6}$ m (dark gray curve), viscous calculations with $L_{\mu}/L_{1/2} = 1/10$, (light gray curve) and theoretical estimate (black curve).

bounds at higher activation energies in the inviscid limit. Furthermore, a study was performed with $L_{\mu}/L_{1/2} = 1/10$ for the diffusive case, and it is clear that the addition of viscosity reduces the ratio of the reaction length scales at a particular activation energy. Moreover, the addition of viscosity essentially shifts the curve to right in activation energy. Thus at sufficiently high activation energies, the finest reaction length scale becomes the scale which dictates the resolution necessary.

As a brief aside, the computational cost of two representative calculations are shown in Table 3.2. In addition to the two calculations listed, an approximation of the computational cost of a similar calculation to $E = 46.37$, which was suggested by [149] and references therein as more representative of a detailed hydrogen-air mixture. In Table 3.2, L_{d_D} is the length of the domain needed if the frame of reference moves at the CJ speed, L_{d_f} the length of the domain needed if distance from the leading shock to the end of the domain remains fixed, t_f the time at the end of integration, Δx_i the spatial resolution needed for the inviscid case, Δx_v the spatial resolution needed for the viscous case, N_{t_i} the number time steps needed in the inviscid case, $N_{t_{RK}}$ the number time steps needed in the viscous case using the Runge-Kutta integration

TABLE 3.2

COMPUTATIONAL COST OF ONE-DIMENSIONAL ONE STEP CJ DETONATIONS

	$E = 32$	$E = 35$	$E = 46.37$
L_{d_D} (m)	4.5×10^{-4}	6.5×10^{-4}	7.5×10^{-3}
L_{d_f} (m)	6×10^{-5}	1×10^{-4}	7.5×10^{-4}
Δx_i (m)	2.5×10^{-9}	1.67×10^{-9}	1.67×10^{-10}
Δx_v (m)	5×10^{-9}	2.5×10^{-9}	3.125×10^{-10}
t_f (μs)	2.5	2.5	5
$N_{t_{i/RK/RKL}}$	$(3.2/25.1/0.7) \times 10^6$	$(5/100/1.5) \times 10^6$	$(10/10000/50) \times 10^6$
CPUhrs	$(15/2.55/0.15) \times 10^2$	$(30/34/0.96) \times 10^2$	$(75/510/4.4) \times 10^5$
AMR CPUhrs	-	-	1.1×10^5

scheme, $N_{t_{RKL}}$ the number time steps needed in the viscous case using the Runge-Kutta-Legendre integration scheme, and the CPUhrs. listed are for the inviscid case for the steadily traveling frame of reference, the viscous case for the Runge-Kutta scheme for the fixed distance from the front boundary, and the viscous case for the Runge-Kutta-Legendre scheme for the fixed distance from the front boundary. Additionally, the adaptive mesh refinement (AMR) reduction factor is assumed to be 40 and the AMR CPUhrs estimate is based on the viscous case for the Runge-Kutta-Legendre scheme for the fixed distance from the front boundary. There is a dramatic increase in the computational cost as the activation energy increases. Furthermore, even in a single dimension with a simple one step model at sufficiently high activation energies, the computations become extremely expensive.

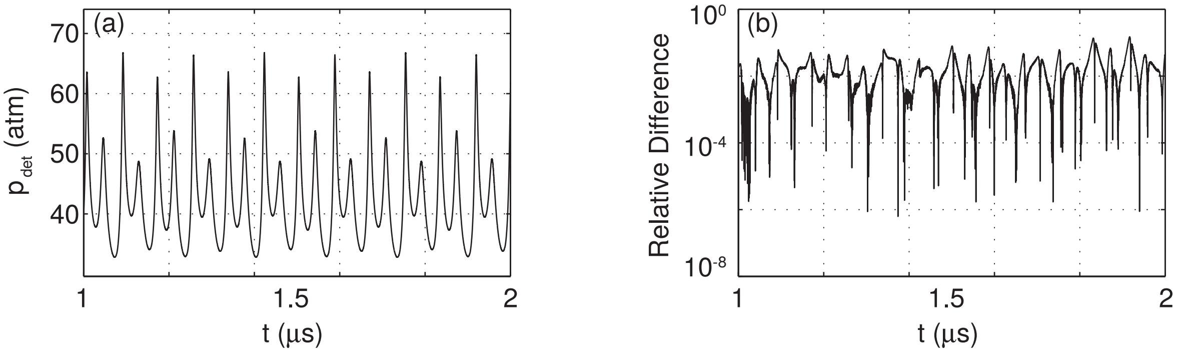

Figure 3.12. (a) Diffusive detonation pressure versus time for both the central differencing and WENO schemes for $E = 30.02$ and (b) the relative difference between the schemes.

3.3.5 Method Independence and Convergence

In this section, firstly, the predictions of the method that makes use of the WENO scheme for advective derivative calculations are compared to a method that use central differences to calculate the advective derivatives. Secondly, the convergence rate of WENO computational method is then discussed in the presence of the Heaviside function.

3.3.6 WENO versus Central Differences

For resolved diffusive detonations, the use of the ubiquitous WENO scheme is unnecessary. The simpler central difference of the advective derivative terms is sufficient. Even with complex behaviors, as in the period-8 behavior predicted for $E = 30.02$, which is shown in Figure 3.12(a), the use of a central difference for the advective terms yields results which agree with those of the WENO scheme. The relative difference between predictions of the two methods is shown in Figure 3.12(b). The values of the detonation pressure match up to a time-shift which originates at initialization.

TABLE 3.3

CONVERGENCE FOR DIFFUSIVE ONE STEP DETONATIONS

Δx (m)	$p_{29.0}$ (atm)	$r_{c_{29.0}}$	$\mathrm{T}_{29.0}$ (μs)	$r_{c_{29.0}}$	$p_{29.5}$ (atm)	$r_{c_{29.5}}$	$\mathrm{T}_{29.5}$ (μs)	$r_{c_{29.5}}$
2.50×10^{-8}	38.14	–	4.071×10^{-2}	–	53.77	–	8.205×10^{-2}	–
1.25×10^{-8}	36.88	2.07	4.062×10^{-2}	3.17	46.95	2.10	8.189×10^{-2}	3.00
6.25×10^{-9}	36.58	–	4.061×10^{-2}	–	45.36	–	8.187×10^{-2}	–

Rates of pressure and frequency for two activation energies.

3.3.7 Convergence Rate

The presence of the Heaviside function in the reaction source precludes the expected fifth order accuracy. The state variables do in fact converge at a lower order than that of the theoretical value. At a representative point in space/time, $x = 1.477 \times 10^{-4}$ m at $t = 1$ μs, the pressure converges at a rate of 2.07 and 2.10 for detonations with activation energies of $E = 29.0$ and $E = 29.5$, respectively. However, the state variables converge at rates larger than unity suggesting that the Heaviside function plays a small role. In addition to the state variables, the periods of oscillation, T, of the oscillation was examined for both cases and are listed in Table 3.3. The period of oscillation was taken starting at 1 μs, as the period-1 and period-2 detonations are within the limit cycle behavior, and going until 3.5 μs; the convergence rates for the periods are higher, 3.17 and 3.00, respectively.

CHAPTER 4

PISTON-DRIVEN HYDROGEN-AIR DETONATIONS

4.1 Introduction

As briefly alluded to in Chapter 1, there are indications that neglecting diffusion in modeling detonations may be problematic. Work done by Singh et al. [138] and Powers [107], demonstrated that the two-dimensional one step detonation patterns relaxed to a grid-independent structure while using the Navier-Stokes equations; however, these patterns remained grid-dependent when using the reactive Euler equations. Likewise, Mazaheri et al. [85] demonstrated that in regions of high resolution in a one step detonation in a channel, diffusion plays an important role. Moreover, it was demonstrated, in Chapter 3 and in [120], that for the one step kinetics model, the long time behavior of the detonation is affected by the addition of viscosity; these viscous effects delay the transition to instability, and in the regime where multiple frequency oscillations exist, viscosity can play a dramatic role. However, the coarsest scales in hydrogen-air detonations are much larger than the chosen $L_{1/2}$; as shown by [108], a mixture of hydrogen-air at ambient conditions of atmospheric pressure has an induction zone of approximately 2×10^{-4} m. It is at these coarser length scales that the main heat release occurs. Al-Khateeb et al. [2] suggest that hydrogen-air mixtures have reaction length scales present which have time scales associated with them over which both chemistry and diffusion can be important. This suggests that viscosity may have a role to play in the dynamics of hydrogen-air detonations; however, the role of viscosity in pulsating detonations of a detailed kinetics model has not been quantified in a detailed manner.

In this chapter, an extension to the results presented in Chapter 3 is presented and has been adapted from Romick et al. [121]. The detailed kinetics model examined in this work is for a hydrogen-air mixture. As opposed to the activation energy that is varied in the one step reaction model, the long time behavior of the detonation for the detailed kinetics model is examined as the overdrive is varied. The overdrive is defined as $f = (D/D_{CJ})^2$ where D and D_{CJ} are the detonation wave speed and the wave speed at which the detonation terminates at the sonic point, respectively. In this study, this is accomplished by using a supporting piston to drive the flow. The evolution of the long time behavior is investigated in the temporal and frequency domains as the supporting piston velocity is varied. Additionally, it will address how the addition of physical mass, momentum and energy diffusion affects the long time behavior in one-dimensional detonations of mixtures modeled by detailed kinetics and multicomponent transport.

The chapter is organized as follows. In Section 4.2, the mathematical model is presented followed by a description of the computational method and a brief description of the physical problem. This is followed by a brief validation of the model and verification of the computational method is discussed in Section 4.3. Next in Section 4.4, the model is used to predict the dynamics of a series of piston-driven hydrogen-air flows. It will be demonstrated that as the supporting piston velocity is lowered, the long time behavior becomes more complex in a similar manner to previous inviscid studies of hydrogen-based overdriven detonations [20, 26, 145, 175]. Furthermore, the addition of diffusive processes has a slightly stabilizing effect, shifting the transition to a pulsating detonation by less than 2% with respect to the supporting piston velocity. Moreover, the long time behavior is examined using harmonic analysis and with the use of the fine resolutions in this study, gives further insight into how the behavior changes as the supporting piston velocity is varied. Additionally, this analysis is used to find similarities and differences between the inviscid and viscous analogs. Lastly, in Section 4.5, a physics-based analysis of the detonation dynamics is discussed using both detailed kinetics and the simpler one step model.

4.2 Formulation

4.2.1 Mathematical Model

The model equations adopted in this chapter are the one-dimensional version of Equations (2.1)-(2.4). Additionally, the diffusive transport relations taken here are Equations (2.30),(2.31), and (2.32) for mass, momentum, and energy diffusion, respectively. The further constitutive equations are listed in Section 2.2. The reaction and mixture properties are evaluated using the `CHEMKIN` package [63], and the diffusive transport coefficients are evaluated `TRANSPORT` package [62].

To initiate a detonation in an initially quiescent fluid, an accelerating piston is positioned on the left side of the domain. For computational purposes, it is easier to use a domain attached to the face of the accelerating piston. Assuming the piston is initially located at $x = 0$ and the velocity of the piston is a known function of time, $u_p(t)$, the accelerating frame can be related to the laboratory frame as

$$\tilde{x} = x - \int_0^t u_p(\hat{t})d\hat{t}, \tag{4.1}$$

$$\tilde{t} = t, \tag{4.2}$$

where $\tilde{x}$ is the location in the accelerating frame, $\tilde{t}$ the time in the accelerating frame of reference, and $\hat{t}$ a dummy variable. Thus, the velocity in the accelerating frame, $\tilde{u}$, can be related to the laboratory frame particle velocity as

$$\tilde{u} = u - u_p(t). \tag{4.3}$$

Applying this transformation, the one-dimensional the governing Equations (2.1)-

(2.4) in the accelerating frame of reference become

$$\frac{\partial \rho}{\partial \tilde{t}} + \frac{\partial}{\partial \tilde{x}} \left(\rho \tilde{u}\right) = 0, \tag{4.4}$$

$$\frac{\partial}{\partial \tilde{t}} \left(\rho \tilde{u}\right) + \frac{\partial}{\partial \tilde{x}} \left(\rho \tilde{u}^2 + p - \tau\right) = -\rho \frac{du_p}{d\tilde{t}}, \tag{4.5}$$

$$\frac{\partial}{\partial \tilde{t}} \left(\rho \left(e + \frac{\tilde{u}^2}{2}\right)\right) + \frac{\partial}{\partial \tilde{x}} \left(\rho \tilde{u} \left(e + \frac{\tilde{u}^2}{2}\right) + \left(p - \tau\right) \tilde{u} + q\right) = -\rho \tilde{u} \frac{du_p}{d\tilde{t}}, \tag{4.6}$$

$$\frac{\partial}{\partial \tilde{t}} \left(\rho Y_i\right) + \frac{\partial}{\partial \tilde{x}} \left(\rho \tilde{u} Y_i + j_i\right) = \overline{M}_i \dot{\omega}_i. \tag{4.7}$$

For a more detailed derivation, the reader is referred to Appendix C. As $\tilde{t} = t$, from here on t will be used in place of $\tilde{t}$.

4.2.2 Computational Methods

The viscous calculations are performed using the Wavelet Adaptive Multiresolution Representation (WAMR) method, first developed by Vasilyev and Paolucci [157, 158]. This adaptive mesh refinement technique is enabled by wavelet functions. These functions have compact support in scale and space, allowing for a large compression of data. Therefore, to accurately represent flow fields with distinct features at fine scales, fewer points are needed compared with a wide variety of other approaches. The WAMR method is a method of lines approach at collocation points and utilizes central finite difference schemes to calculate derivatives with special one-sided differences near boundaries. Additionally, it utilizes a user-specified control threshold parameter that correlates to the error tolerated in the solution, allowing unnecessary points to be discarded. See Paolucci et al. [106] for a more detailed description of the method in its current form. It has been applied successfully to a number of fluids problems, *cf.* Singh et al. [139], Rastigejev [115], Wirasaet and Paolucci [170], Rastigejev and Paolucci [116], Rastigejev and Paolucci [117], Wirasaet [169], Zikoski [180], and Paolucci et al. [105]. The temporal integration is accomplished using an error-controlled nominally fifth order Runge-Kutta scheme [109].

In addition, inviscid calculations are compared directly with the viscous calculations. For these inviscid calculations, all diffusion coefficients, viscosity, and thermal conductivity are taken to be zero. A uniform finite difference grid is used for these calculations and utilizes a combination of a nominally second order mid-mod and Lax-Friedrichs scheme to calculate derivatives in a similar manner to that Xu et al. [173] implemented in their WENO and Lax-Friedrichs scheme. Temporal integration for the inviscid calculations is accomplished using a third order Runge-Kutta method.

For the viscous calculations the threshold used for the WAMR method is $\epsilon = 10^{-3}$ unless otherwise specified. This selection leads to a spatial resolution of $\mathcal{O}(3\times10^{-8}\text{ m})$ to be utilized which results in a time step of $\mathcal{O}(10^{-12}\text{ s})$. After the formation of the detonation, a typical simulation time for a viscous calculation of ~ 1 μs took $\mathcal{O}(300\text{ CPUhrs})$ on 32 cores. For the inviscid calculations a spatial discretization of 2.5×10^{-7} m is used which results in a time step of $\mathcal{O}(10^{-10}\text{ s})$.

4.2.3 Problem Parameters

In this study, a series of one-dimensional, piston-driven flows of an initially stoichiometric mixture of hydrogen-air ($2H_2 + O_2 + 3.76N_2$) at ambient conditions of 293.15 K and 1 atm is considered. The detailed kinetics mechanism employed is drawn from Miller et al. [89] and is used by Powers and Paolucci [108]. It contains 9 species, 3 elements and 19 reversible reactions where nitrogen is treated as a non-reacting species and is shown in Table 4.1.

The flow is accelerated using a piston with a velocity, $u_p(t)$, taking the form

$$u_p(t) = \frac{1}{2}\left(u_{p_o}\left(1 + \tanh\left(\mathsf{a}\left(t - \mathsf{t}_a\right)\right)\right) - \left(u_{p_o} - \overline{u_p}\right)\left(1 + \tanh\left(\mathsf{b}\left(t - \mathsf{t}_b\right)\right)\right)\right), \qquad (4.8)$$

where u_{p_o} is the initial plateau in piston velocity, $\overline{u_p}$ the final piston velocity, a the rate of acceleration to the initial plateau, t_a the time at which the acceleration is

TABLE 4.1

HYDROGEN-AIR REACTION MECHANISM

j	Reaction	a_j $\left(\frac{(\text{mole/cm}^3)^{\left(1-\sum_{i=1}^{N}\nu'_{ij}\right)}}{\text{K}^{\beta_j}\ \text{s}}\right)$	β_j	E_j $\left(\frac{\text{cal}}{\text{mole}}\right)$
1	$H_2 + O_2 \rightleftharpoons 2OH$	1.70×10^{13}	0.00	47780
2	$OH + H_2 \rightleftharpoons H_2O + H$	1.17×10^{9}	1.30	3626
3	$H + O_2 \rightleftharpoons OH + O$	5.13×10^{16}	−0.816	16507
4	$O + H_2 \rightleftharpoons OH + H$	1.80×10^{10}	1.00	8826
5	$H + O_2 + M \rightleftharpoons HO_2 + M^a$	2.10×10^{18}	−1.00	0
6	$H + O_2 + O_2 \rightleftharpoons HO_2 + O_2$	6.70×10^{19}	−1.42	0
7	$H + O_2 + N_2 \rightleftharpoons HO_2 + N_2$	6.70×10^{19}	−1.42	0
8	$OH + HO_2 \rightleftharpoons H_2O + O_2$	5.00×10^{13}	0.00	1000
9	$H + HO_2 \rightleftharpoons 2OH$	2.50×10^{14}	0.00	1900
10	$O + HO_2 \rightleftharpoons O_2 + OH$	4.80×10^{13}	0.00	100
11	$2OH \rightleftharpoons O + H_2O$	6.00×10^{8}	1.30	0
12	$H_2 + M \rightleftharpoons H + H + M^b$	2.23×10^{12}	0.50	92600
13	$O_2 + M \rightleftharpoons O + O + M$	1.85×10^{11}	0.50	95560
14	$H + OH + M \rightleftharpoons H_2O + M^c$	7.50×10^{23}	−2.60	0
15	$H + HO_2 \rightleftharpoons H_2 + O_2$	2.50×10^{13}	0.00	700
16	$HO_2 + HO_2 \rightleftharpoons H_2O_2 + O_2$	2.00×10^{12}	0.00	0
17	$H_2O_2 + M \rightleftharpoons OH + OH + M$	1.30×10^{17}	0.00	45500
18	$H_2O_2 + H \rightleftharpoons HO_2 + H_2$	1.60×10^{12}	0.00	3800
19	$H_2O_2 + OH \rightleftharpoons H_2O + HO_2$	1.00×10^{13}	0.00	1800

Enhanced third-body efficiencies with M:

M^a: $\alpha_{H_2O} = 21.0$, $\alpha_{H_2} = 3.30$, $\alpha_{N_2} = 0.00$, $\alpha_{O_2} = 0.00$

M^b: $\alpha_{H_2O} = 6.00$, $\alpha_{H} = 2.00$, $\alpha_{H_2} = 3.00$

M^c: $\alpha_{H_2O} = 20.0$

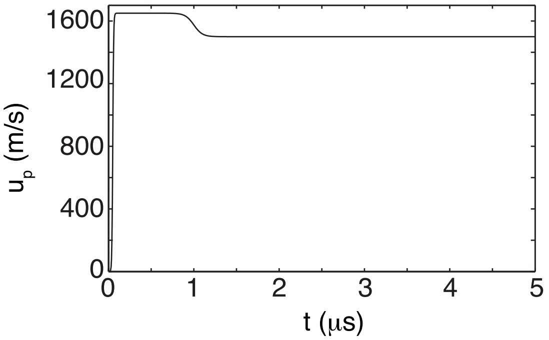

Figure 4.1. The supporting piston velocity versus time curve for $\overline{u_p} = 1500$ m/s.

centered, b the rate of acceleration to the final supporting piston velocity, and t_b the time at which the deceleration is centered. This form has two plateaus and is chosen to allow for a more rapid formation of the initial detonation. Figure 4.1 shows the chosen form of the piston velocity for case A in Table 4.2 for $\overline{u_p} = 1500$ m/s.

The form of the piston acceleration in the initialization of the detonation plays a significant role in the early time behavior, also known as the DDT problem. The compression wave pushed into the fluid by the piston causes a shock to form which then proceeds to propagate away from the piston face. The strength of this shock wave is dependent on the supporting piston velocity and gives rise to a reaction wave due to pre-heating. This reaction wave eventually gives rise to a localized explosion, which eventually develops into an overdriven detonation before relaxing at long times. This process is similar to that described by a localized thermal power deposition used by Kassoy et al. [61], Kassoy [60], and Regele et al. [118]. The weaker the inertial confinement of the initial reaction wave, the longer the initial detonation takes to form.

As this work focuses on the long time behavior of the detonation, the long time behavior of three piston acceleration profiles is examined with the same final supporting piston velocity of $\overline{u_p} = 1500$ m/s to examine whether this early time effect

TABLE 4.2

INITIALIZATION PARAMETERS

Case	u_{p_o} (m/s)	$\overline{u_p}$ (m/s)	a (1/s)	t_a (s)	b (1/s)	t_b (s)
A	1650	1500	10^8	5×10^{-8}	10^7	1×10^{-6}
B	1650	1500	10^7	1×10^{-6}	10^7	3×10^{-6}
C	1500	1500	10^7	1×10^{-6}	10^7	3×10^{-6}

continues to later times. The parameters for the three different initialization profiles are listed in Table 4.2. As shown in Figure 4.2, the inertial confinement of the initial reaction wave plays a dramatic role in the time to detonation. Additionally, the overpressure is much greater for the weaker driven shock, and it also takes longer to relax to a steady state. However, the long time behavior relaxes to a stable detonation in all three cases, with the local maximum pressure at the front, which is the detonation pressure, of $p_A = 36.75$ atm, $p_B = 36.76$ atm and $p_C = 36.73$ atm, meaning all three cases are within 0.1% of each other. For the remainder of the chapter, case A is used allowing only $\overline{u_p}$ to vary. Final piston velocities ranging from 1200 m/s to 1500 m/s are examined.

4.3 Validation of the Model and Verification of the Computational Method

The model has been restricted to one dimension; thus, there are limited means of validation. However, in experiments of shock-induced combustion flow around spherical projectiles in a hydrogen-air mixture at 0.421 atm and 293.15 K, Lehr [70] observed longitudinal oscillations. Figure 4.3 shows these oscillations in an image originally reported by Lehr. For an inflow condition corresponding to an overdrive $f \approx 1.10$, Lehr observed a frequency of $\nu_o = 1.04$ MHz. Starting the viscous calcu-

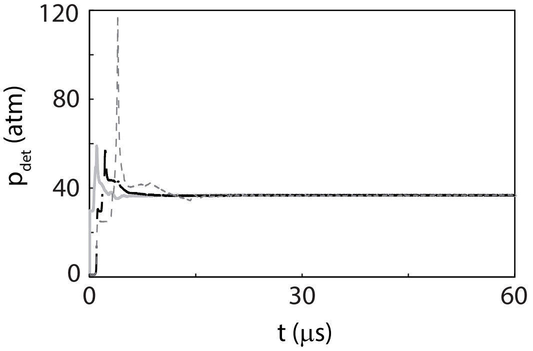

Figure 4.2. The detonation pressure versus time curve $\overline{u_p} = 1500$ m/s. (Case A - solid light gray line, Case B - dashed black line and Case C - dashed dark gray line).

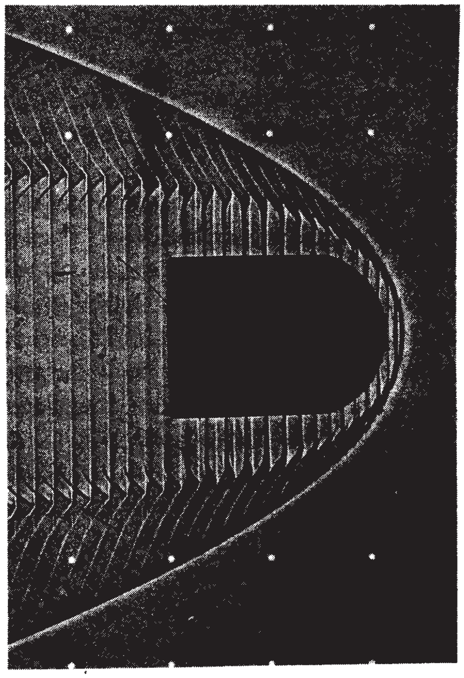

Figure 4.3. An image from Lehr [70] of the longitudinal oscillations in the shock-induced combustion around a projectile in a hydrogen-air mixture at 0.421 atm and 293.15 K.

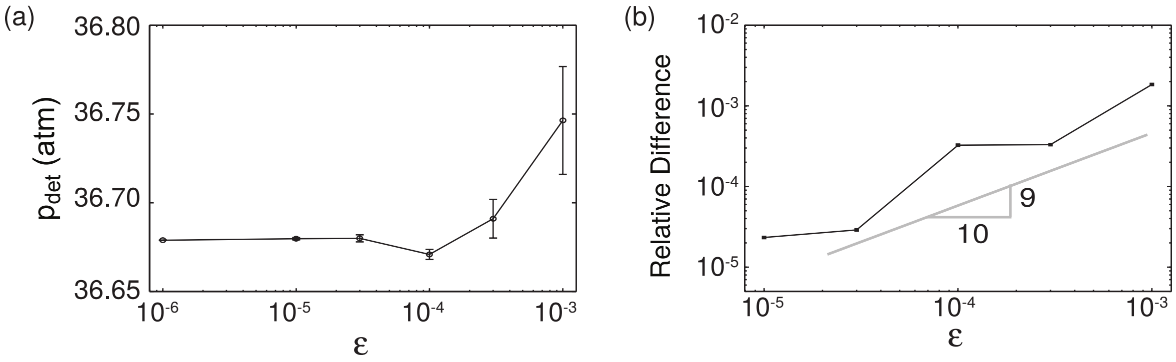

Figure 4.4. (a) Detonation pressure versus ϵ and (b) difference in detonation pressure between $\epsilon = 1 \times 10^{-6}$ and ϵ for $\overline{u_p} = 1500$ m/s.

lation with the inviscid steady state profile with a superimposed smooth transition from the shocked state to the ambient condition over 5×10^{-6} m, a frequency of $\nu_o = 0.97$ MHz is predicted. Thus, it seems that the instability observed by Lehr in multiple dimensions is captured well by a one-dimensional model. This is similar to results reported by Yungster and Radhakrishan [175] of $\nu_o = 1.06$ MHz for an overdrive of $f = 1.09$ with an ambient temperature of 298 K and Daimon and Matsuo [20] who do not report frequency explicitly, but visual inspection suggests that the frequencies are in the 1 MHz range. The predicted frequency here is only 6.7% different from that measured by Lehr; the discrepancy is likely due the one-dimensional assumption and uncertainty in chemical kinetic parameters. Only a minimal effect on the frequency was predicted using several other hydrogen-based chemical mechanisms.

The WAMR procedure is a self-converging method, which means that as the error-threshold parameter, ϵ, is reduced, the overall error is reduced. To verify that in fact the procedure is convergent regime, several values of ϵ are examined for $\overline{u_p} = 1500$ m/s. The long time behavior at this supporting piston velocity is a stable, steadily traveling detonation as shown in Figure 4.2. Figure 4.4(a) shows the long time detonation pressure versus ϵ. The detonation pressure is converging to 36.68 atm. It should be noted the standard deviation on the detonation pressure is indicated by the vertical lines. As the error-threshold parameter is reduced, the standard deviation is reduced around the detonation pressure point indicated by the dots. In fact at the two most accurate solutions, the standard deviation in the detonation pressure is difficult to identify. Additionally, the difference in the long time detonation pressure is calculated from the most accurate solution; this is shown in Figure 4.4(b). As the error-threshold parameter is reduced the difference decreases near $O\left(\epsilon^{0.9}\right)$, as indicated on the log-log plot. Furthermore, the largest percent difference is a 0.2% giving a good indication that the WAMR method is in the convergent regime.

4.4 Results

In this section, a study of the long time behavior of the propagating detonation is performed as the final supporting piston velocity, $\overline{u_p}$, is varied. This is done first in the time domain, and then harmonic analysis is used to examine the active frequencies of the pulsating detonations in Section 4.4.5. Lastly, in Section 4.4.7, several comparisons between the viscous and inviscid calculations are performed in both the time and frequency domains.

4.4.1 Stable Detonations

For sufficiently high $\overline{u_p}$, a steadily traveling detonation arises and persists at long times. The detonation pressure versus time curve for a stable detonation, at $\overline{u_p} = 1500$ m/s, is shown in Figure 4.1. For case A, by 10×10^{-6} s the detonation relaxes to a steadily traveling piston-supported detonation traveling to the right at 2244 m/s. Spatial pressure profiles after the detonation relaxes to the stable detonation are shown in Figure 4.5(a) for $t = 10 \times 10^{-6}$ s, $t = 35 \times 10^{-6}$ s and $t = 60 \times 10^{-6}$ s. The later time profiles have been shifted in space using the steady wave speed. There are only

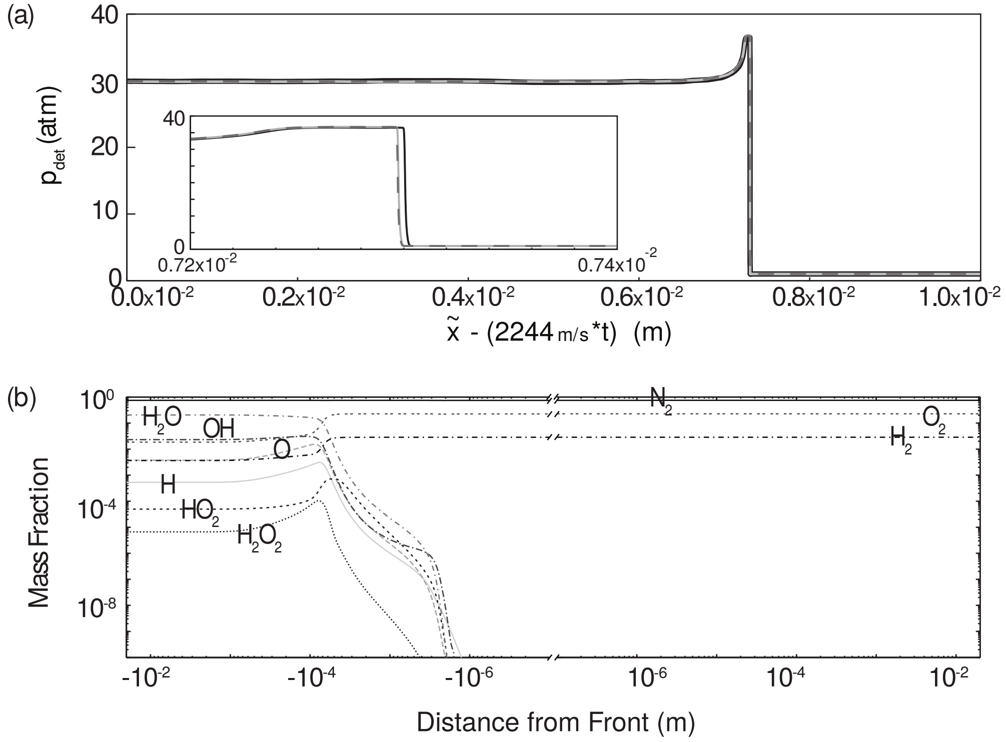

Figure 4.5. (a) Several time shots of the spatial pressure profile (solid black line - 10×10^{-6} s, solid light gray line - 35×10^{-6} s and dashed gray line - 60×10^{-6} s) and (b) typical spatial profile of mass fractions at a $\overline{u_p} = 1500$ m/s.

minuscule differences between the front locations; these differences are more clearly shown in the insert. However, the largest difference between the front locations is still only 2.5×10^{-6} m. Figure 4.5(b) shows the spatial mass fraction at $t = 50 \times 10^{-6}$ s which is representative of the steadily traveling detonation front. As a particle passes through the detonation, it first encounters a thin viscous shock accompanied by rapid pressure and temperature rise. Then, its pressure and temperature remain relatively constant as it traverses a short induction zone. In this zone radicals are generated. When a sufficient number of radicals are present, the fluid particle enters a thin zone in which vigorous reaction commences. Here pressure and temperature vary rapidly. Finally, it passes into a thick relaxation zone, where all state variables equilibrate.

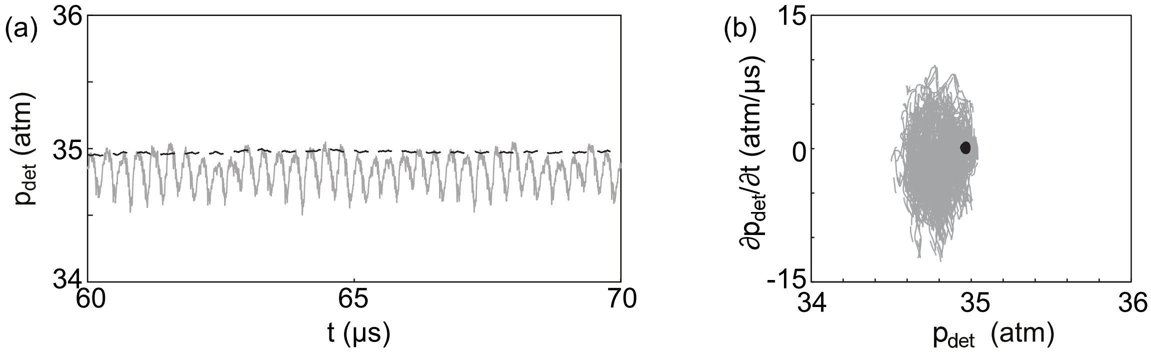

Figure 4.6. (a) Detonation pressure versus time and (b) phase space plot for both $\overline{u_p} = 1420$ m/s (dashed black line) and $\overline{u_p} = 1410$ m/s (solid gray line). Note the phase space plot for $\overline{u_p} = 1420$ m/s has been enlarged by a factor of ten.

4.4.2 High Frequency Pulsating Detonations

After $\overline{u_p}$ is lowered below a critical value, the long time behavior of the propagating detonation undergoes a transition from a steadily traveling wave to a pulsating detonation. This transition occurs between $\overline{u_p} = 1420$ m/s and $\overline{u_p} = 1410$ m/s. Figure 4.6(a) shows the detonation pressure versus time curves for a supporting piston velocity just above and just below the transition point. These pulsations are caused by the slight detachment between the pressure wave and the reaction wave, which in turn elongates the induction zone. The phase space plot for both the stable and unstable case for both the stable and unstable case is shown in Figure 4.6(b). For the stable case, the phase space plot is a black dot located at $p = 34.95$ atm, the dot is enlarged by 10 times for ease of viewing. At $\overline{u_p} = 1410$ m/s, it becomes clear that detonation is pulsating; however, it is difficult to extract whether it is near cyclic from the phase space plot. This case will be examined further in Section 4.4.5 to extract more information about the pulsations.

In contrast to the clear periodic limit cycles predicted by Henrick et al. [47] for the simple one step model in the CJ limit, the pulsating detonations here do not produce

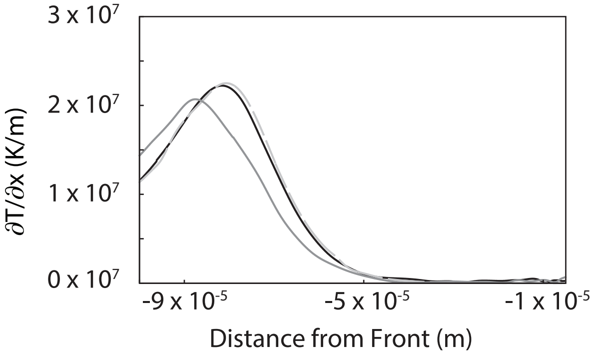

Figure 4.7. The temperature gradient through the induction zone for a stable detonation at $\overline{u_p} = 1420$ m/s (black solid line), at the peak detonation pressure (dashed light gray line) and at the minimum detonation pressure (dark gray line) for an unstable detonation at $\overline{u_p} = 1410$ m/s.

nearly as smooth limit cycles. This is likely influenced by several factors. First, the piston-driven flows in this study are overdriven in nature; as such, the positively moving characteristic waves travel through different decaying N-waves in the negatively moving characteristic field emanating from the detonation front. The likelihood of these positively moving characteristic waves and decaying negatively moving characteristic N-waves being synchronized is extremely low, and thus precludes precisely periodic cycles. These positively moving characteristics in the overdriven case clearly reach the detonation shock front. In the CJ case, there is a sonic locus that remains a finite distance behind the front. As demonstrated by Kasimov and Stewart [59] for the one step model, this sonic locus acts as an information barrier. It only allows characteristics in front of it to propagate towards the front. Additionally, the one step model has only a single length scale of reaction, whereas the detailed hydrogen-air mechanism has reaction length scales that span several orders of magnitude. Furthermore, the one step model is irreversible, while the detailed kinetics model has reversible reactions.

The induction zone length changes in the pulsating detonations due to slight separation between the pressure wave and the reaction front. For $\overline{u_p} = 1410$ m/s, the minimum induction zone length is 8.06×10^{-5} m during the cycle which corresponds to the point of peak detonation pressure. The maximum temperature gradient behind the front is used as the indicator for the end of the induction zone length. The maximum induction zone length occurs at the minimum detonation pressure in the cycle and is 8.73×10^{-5} m. As Figure 4.7 shows, the stable detonation just above the bifurcation point, at $\overline{u_p} = 1420$ m/s, has a induction zone length of 8.11×10^{-5} m. This induction zone length is close to the minimum of that of the pulsating detonation because the detonation pressure for the stable case is similar to the peak detonation pressure in the pulsating case. At the minimum detonation pressure in the cycle, it is clear that the gradient in temperature is delayed and decreased in magnitude; likewise, at the peak detonation pressure the peak is slightly greater than that in the stable case.

As shown in Figure 4.8(a), when $\overline{u_p}$ is lowered further below the bifurcation point, the oscillations grow in amplitude. Additionally, the frequency shifts towards lower frequencies. As the pulsations become larger in amplitude, it becomes clearer that they are nearly periodic, as demonstrated by successive pulsations nearly coinciding in the phase plot of Figure 4.8(b).

4.4.3 Multiple Mode Pulsating Detonations

The behavior becomes even more complex at lower supporting piston velocities with a dual mode behavior arising below a second bifurcation point. An example of this type of propagating detonation is shown in Figure 4.9(a) for $\overline{u_p} = 1310$ m/s. It is apparent that the dual mode behavior persists at long times. Although these dual mode detonations do not repeat in a clean limit cycle, it is still obvious that it is stably bounded at long times which is demonstrated by the phase plane plot shown in Figure 4.9(b).

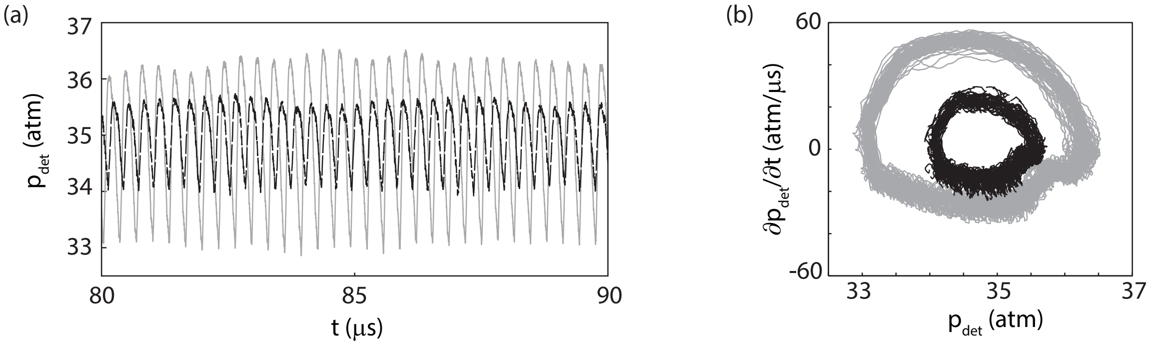

Figure 4.8. (a) Detonation pressure versus time and (b) phase space plot for both $\overline{u_p} = 1400$ m/s (dashed black line) and $\overline{u_p} = 1370$ m/s (solid gray line).

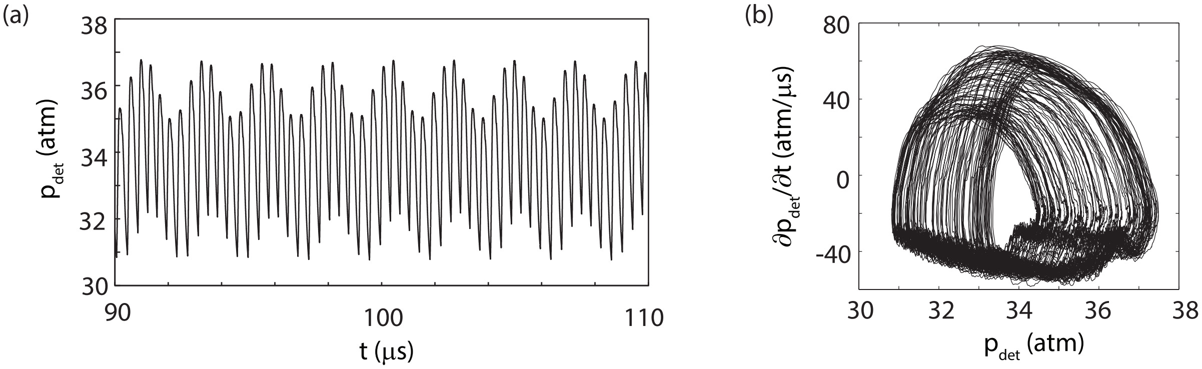

Figure 4.9. (a) Detonation pressure versus time and (b) phase space plot for a $\overline{u_p} = 1310$ m/s.

4.4.4 Low Frequency Dominated Pulsating Detonations and Chaos

At yet even lower supporting piston velocities, this dual mode behavior relaxes into a mode that is dominated by a single low frequency pulsating flow. Figure 4.10(a) shows this relaxation to a nearly periodic limit cycle at long times. However, the phase space plot, shown in Figure 4.10(b), indicates that even at long times there is still some variation in the cycle. Once this low frequency mode becomes the dominant mode, a behavior similar to period-doubling is predicted. As shown in Figure 4.10(c), a nearly period-2 detonation is predicted at $\overline{u_p} = 1230$ m/s. At this supporting piston velocity, the relative maxima can be grouped into two distinct groups; the first at $p_1 = 47.56 \pm 0.68$ atm and the second being $p_2 = 50.9 \pm 0.84$ atm. Figure 4.10(d) clearly exhibits the distinct two-lobe phase space for a period-2 detonation. This phenomenon is exhibited even more prominently at $\overline{u_p} = 1220$ m/s, as shown in Figure 4.10(e). However, the higher relative maxima is more erratic as indicated by the wider spread in right-most lobe shown in the phase space plot of Figure 4.10(f). This period-doubling behavior is more clearly seen in the frequency domain and will be discussed further in Section 4.4.5. After this period-doubling regime, the detonation pressure versus time curve exhibits many more relative maxima, which is shown in Figure 4.10(g) for $\overline{u_p} = 1200$ m/s. This is further elucidated by examining the phase space plot, shown in Figure 4.10(h), where no consistent cycle is visible. The system likely underwent a transition to chaos. However, to definitively categorize the system as chaotic further analysis would be needed.

4.4.5 Harmonic Analysis

Next, the detonation pressure versus time behavior is examined using harmonic analysis. As in Chapter 3, in this study the discrete one-sided mean-squared amplitude PSD, $\Phi_d(\nu_k)$, is used to extract the dominant frequency and a ratio of energy carried at various frequencies. The PSD of a signal reveals periodicities that can be

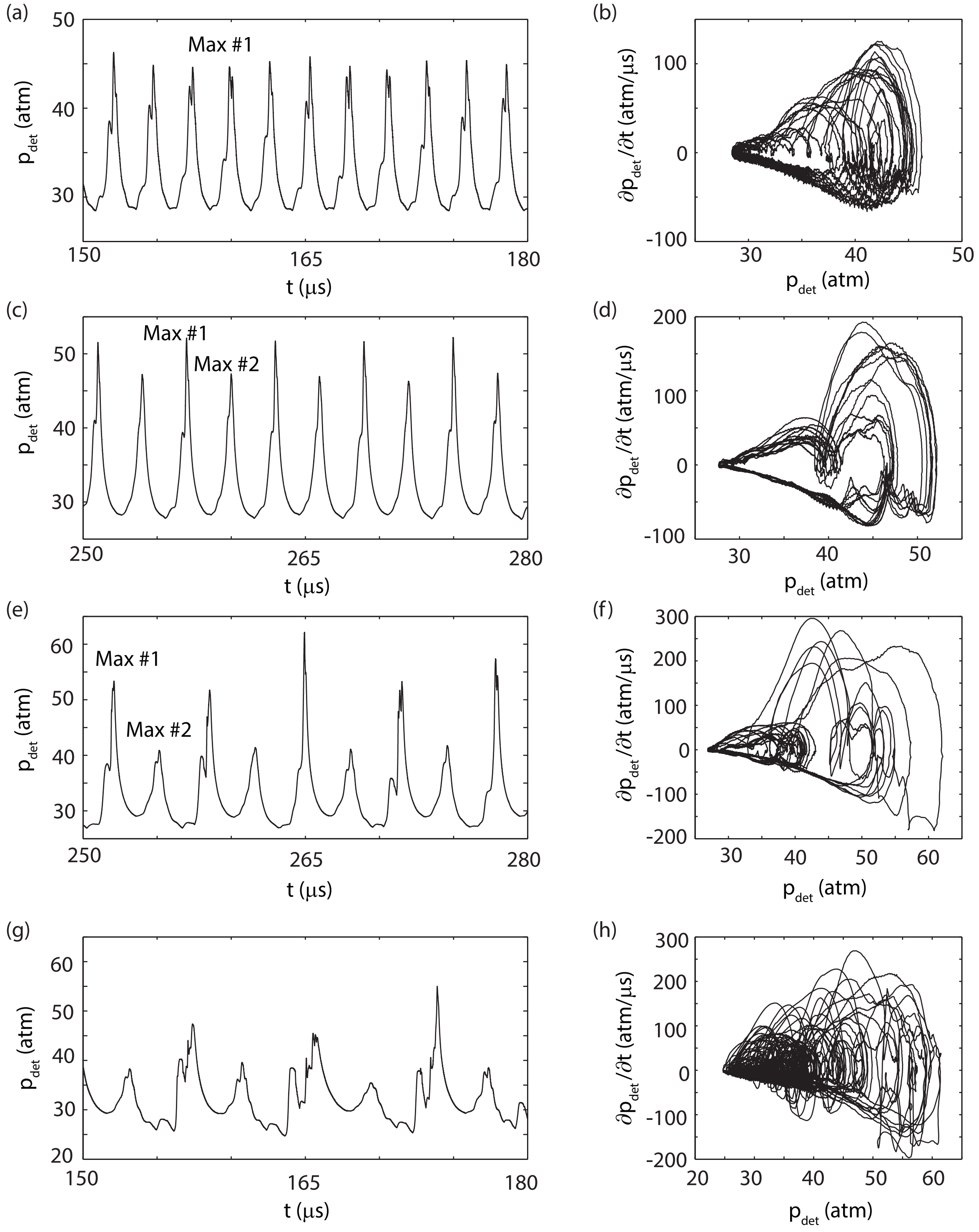

Figure 4.10. Detonation pressure versus time and the respective phase plots for (a-b) $\overline{u_p} = 1250$ m/s, (c-d) $\overline{u_p} = 1230$ m/s, (e-f) $\overline{u_p} = 1220$ m/s and (g-h) $\overline{u_p} = 1200$ m/s.

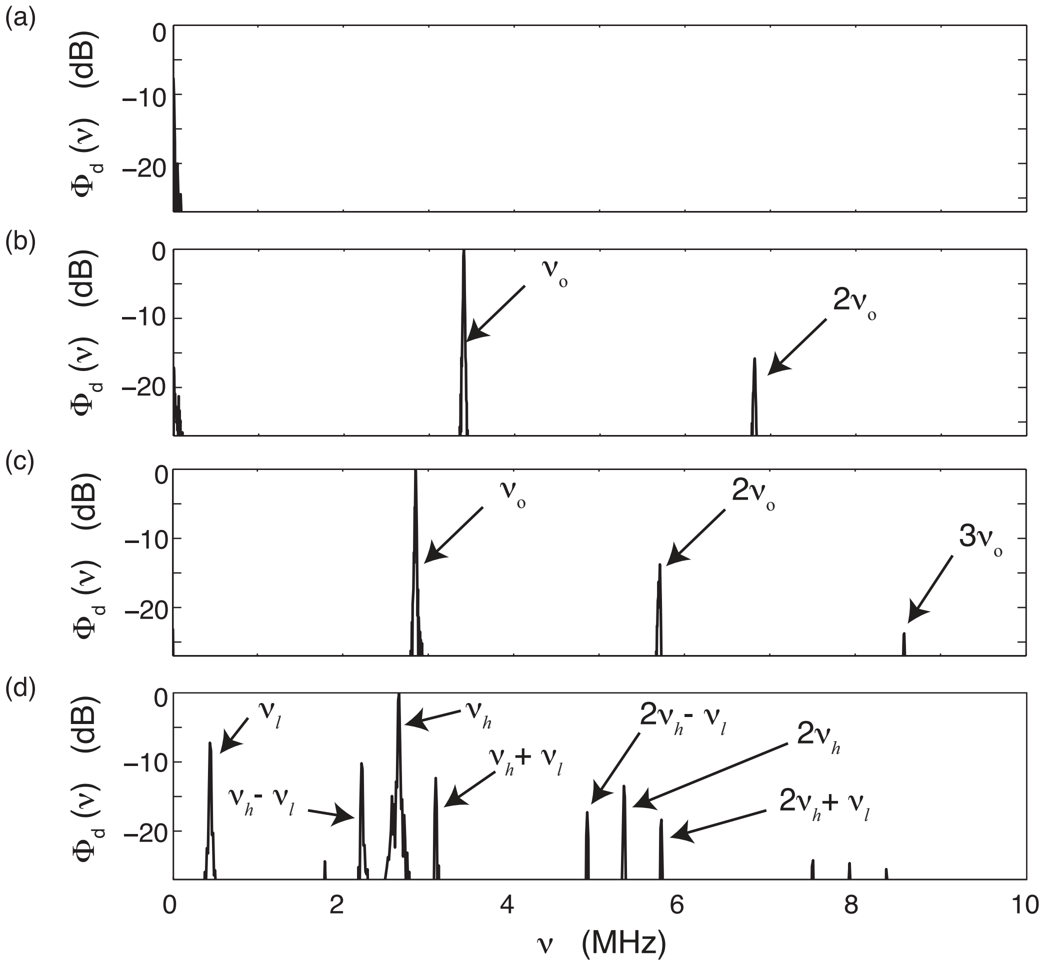

Figure 4.11. PSD viscous spectra at (a) $\overline{u_p} = 1500$ m/s, (b) $\overline{u_p} = 1410$ m/s, (c) $\overline{u_p} = 1340$ m/s and (d) $\overline{u_p} = 1310$ m/s.

hidden in a complex signal, in particular the dual mode pulsating behavior. Furthermore, it can be helpful to discern how the frequency of the pulsations is affected by changing the supporting piston velocity. The detonation pressure time series curves are analyzed after the initialization period. In this work, signals with deviations larger than 0.04 atm from the mean have the mean detonation pressure subtracted out for the calculation of PSD. For more details on how the PSD is calculated see Appendix B.

As discussed previously in Section 4.4.1, when the supporting piston velocity is sufficiently high, the long time behavior is a steadily traveling detonation wave. As depicted in the frequency domain as shown in Figure 4.11(a), the PSD spectrum demonstrates all the energy is concentrated near the zero frequency. Lowering $\overline{u_p}$ below the first bifurcation point, gives rise to a pulsation at $\nu_o = 3.41$ MHz at $\overline{u_p} = 1410$ m/s. In Figure 4.11(b) it is clear that the majority of the pulsation energy is carried at a single frequency. However, the second harmonic frequency also carries energy; this results in slight differences in the relative maxima in detonation pressure in cycle. As the supporting piston velocity is lowered, the frequency spectrum blue shifts. At $\overline{u_p} = 1.340$ m/s, shown in Figure 4.11(c), the fundamental frequency is now located at $\nu_o = 2.85$ MHz, and the harmonics have shifted as well. In fact the ratio of the amount of energy being concentrated at higher harmonics has increased, which is demonstrated by the appearance of the third harmonic in the plot. Examining a $\overline{u_p}$ further below the neutral stability boundary, it becomes clear there is a low frequency mode that is now playing an important role in the long time behavior of the pulsations as shown for $\overline{u_p} = 1310$ m/s in Figure 4.11(d). At this $\overline{u_p}$, the low frequency mode occurs at $\nu_l = 0.44$ MHz and carries a significant amount of energy. However, the high frequency mode, which occurs at $\nu_h = 2.65$ MHz, is still the dominant mode. These modes remain stationary at a smaller error-threshold parameter, once again confirming the WAMR is capturing the long time behavior. Furthermore in this regime where there are two dominant modes; the modes interact giving rise to many more modes that carry energy.

This interaction of the two dominant modes gives rise to a modulation instability. This modulation instability phenomenon occurs in many other physical systems due to the inherent nonlinearity of the physical world [177]. In these pulsating detonations it manifests itself as active modes, called sidebands, at multiples of the low frequency around the high frequency and its harmonics. These active modes surrounding the high frequency mode and its harmonics form envelope waves that persist at long

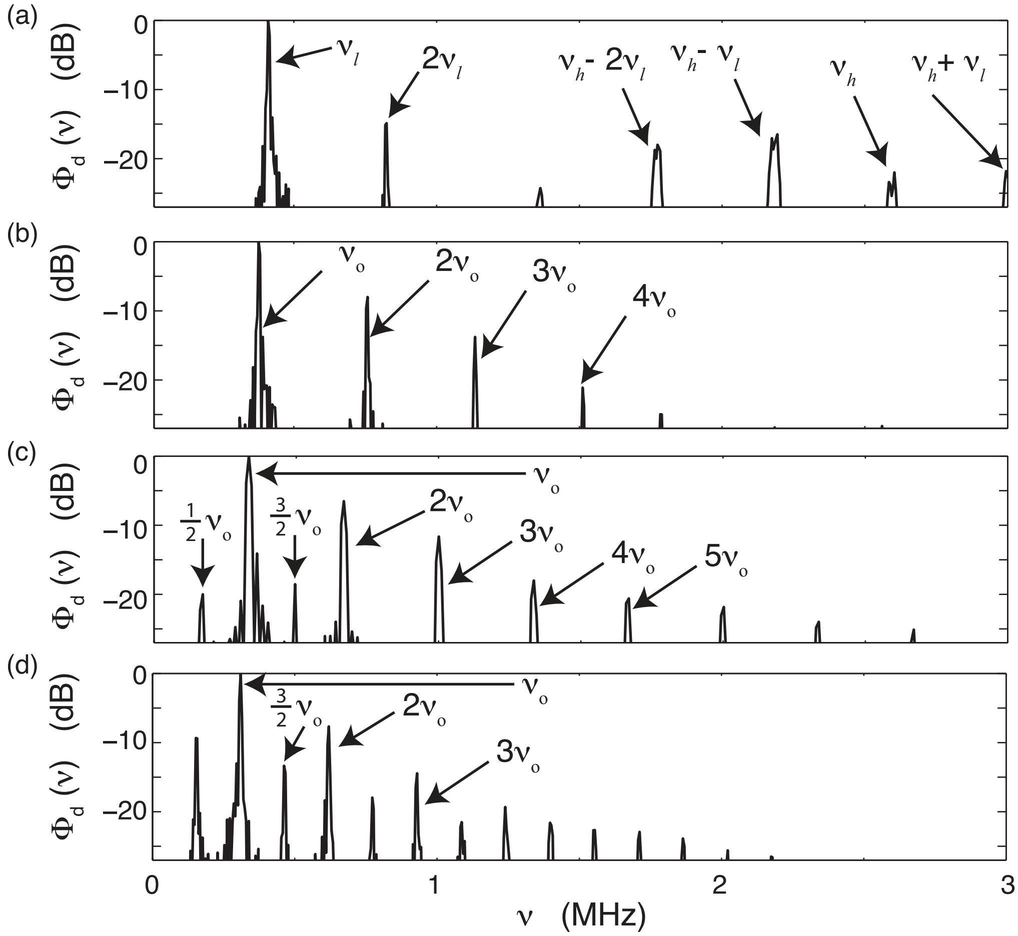

Figure 4.12. PSD viscous spectra at (a) $\overline{u_p} = 1290$ m/s, (b) $\overline{u_p} = 1260$ m/s, (c) $\overline{u_p} = 1230$ m/s and (d) $\overline{u_p} = 1220$ m/s.

times.

After the appearance of the dual mode behavior, the ratio of the energy present in the pulsation carried at the high fundamental frequency continues to decrease as $\overline{u_p}$ is lowered further. Figure 4.12(a) shows the PSD for a $\overline{u_p} = 1290$ m/s and demonstrates that a much more dominant low fundamental frequency at 0.41 MHz exists compared with that of Figure 4.10(d). However, the high frequency mode, which is located at 2.64 MHz, still carries energy. In fact, the lower side bands around the high frequency mode carries a similar order of magnitude of energy as the second harmonic of the low frequency mode. However, it is also clear the side bands have also been reduced, indicating further that the high frequency modes have weakened. Even as more energy is shifting to the lower frequency, the spectrum continues to blue shift towards lower frequencies as the supporting piston velocity is lowered, but at a slower rate than predicted in the high frequency mode. Eventually the low frequencies become so dominant that the high frequency mode and side bands carry less energy than the fourth harmonic of the low frequency mode, as shown Figure 4.12(b) by the PSD at $\overline{u_p} = 1260$ m/s, where $\nu_o = 0.38$ MHz. Nonetheless, there is a side band frequency mode that still persists at long times, but at a lower energy state. This is likely a manifestation of the multiple reaction length scales interacting with each other as well as the diffusion length scales.

As briefly mentioned in Section 4.4.4, after the low frequency mode has become dominant, the long time behavior goes through a phenomenon similar to period-doubling. This is more clearly illustrated in the frequency domain shown in the two PSD spectra in Figure 4.12(c) and (d) for $\overline{u_p} = 1230$ m/s and $\overline{u_p} = 1220$ m/s, respectively. This near period-doubling is illustrated by the appearance of sub-harmonics of the fundamental frequency. As an example, in Figure 10(c) the fundamental frequency is located at 0.34 MHz, but there are peaks in the PSD spectrum at 0.17 MHz and 0.49 MHz, which 1/2 and 3/2 the fundamental frequency, respectively. These are sub-harmonic frequencies, which indicates that the long time behavior of the pulsations is near a limit cycle with two distinct relative maxima in the detonation pressure time curve. Figure 4.12(d) shows that the first set of sub-harmonics have grown in amplitude indicating the strength of the period-2 detonation has grown.

4.4.6 Bifurcation Diagram

A bifurcation diagram is constructed showing the various propagation modes. It has been created with 31 supporting piston velocities spaced at 10 m/s and as such is a coarse approximation of the full diagram. Figure 4.13(a) shows how the maximum detonation pressure evolves versus the supporting piston velocity. Note the peak detonation pressure has been scaled by the average detonation pressure. As the peak detonation pressure varies from cycle to cycle, the standard deviation of peaks in the stable, high frequency dominated, and low frequency dominated modes are indicated by vertical lines. In both the stable and high frequency dominated modes, the standard deviations are difficult to distinguish from the peak detonation pressure. The region in which there are two active modes is indicated by the dense number of points near $\overline{u_p} = 1300$ m/s; likewise, the dense region near $\overline{u_p} = 1200$ m/s is indicative of a detonation with many active modes, which is likely chaotic. This is more clearly understood by looking at the bifurcation plot of the active frequencies, shown in Figure 4.13(b), in which the shade of the points indicates the magnitude with the darkest being the most dominant mode and the lightest being the weakest. In the high frequency mode, there are three active frequencies: the fundamental frequency, the second harmonic, and the third harmonic. The blue shift of the frequency spectrum is most clearly seen in the third harmonic. In the dual mode region, it is apparent that side banding occurs near the high frequency mode and its harmonics; however, there are still just two dominant modes. The side banding continues in the low frequency mode, but at weaker strengths than that of the dual mode. Additionally, sub-harmonics appear at 1/2 and 3/2 at both $\overline{u_p} = 1230$ m/s and $\overline{u_p} = 1220$ m/s. At this lower supporting piston velocity, further sub-harmonics appear at the half intervals as well as the previously mentioned sub-harmonics grow in strength. In the lowest supporting piston velocities studied, many frequencies are active indicating that it is likely that the detonation is in a chaotic regime.

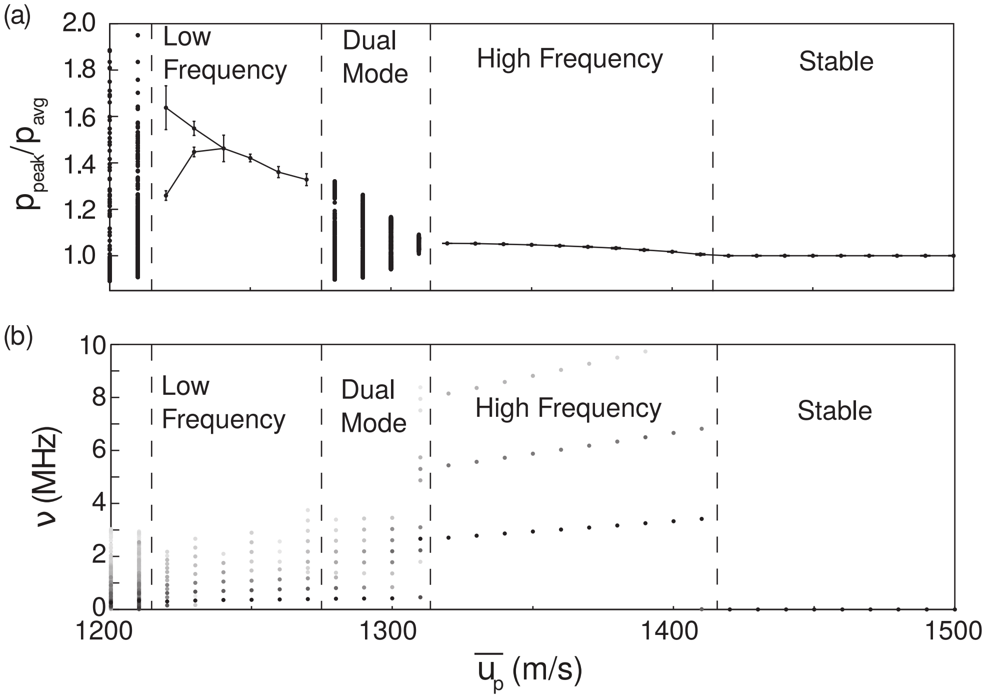

Figure 4.13. Bifurcation plot of (a) the maximum detonation pressure scaled by the average detonation pressure (b) active frequencies versus supporting piston velocity where the darker shade of the point indicates larger magnitude.

4.4.7 Comparison to Inviscid Analog

Several supporting piston velocities are examined in the inviscid limit to elucidate the effects of physical diffusion on a one-dimensional detonation of detailed kinetics mechanism where instabilities are manifested as pulsations. As in the viscous case, when the supporting piston velocity is sufficiently high, a stable steadily traveling detonation is formed and persists at long times. Figure 4.14(a) shows both the viscous and inviscid detonation pressure versus time curves at $\overline{u_p} = 1500$ m/s. The inviscid case relaxes to a detonation pressure of 36.68 atm which is less than 0.1% different from the viscous analog at this piston velocity. However, at $\overline{u_p} = 1430$ m/s the inviscid detonation begins to pulsate with an oscillation amplitude of ~ 1 atm whereas the viscous analog remains stable as shown in Figure 4.14(b). This pulsation amplitude is larger than that of the viscous case at $\overline{u_p} = 1410$ m/s. Thus, the addition of diffusion to the model has added a slightly stabilizing effect, shifting the transition to a pulsating detonation by greater than 1.5%, but less than 2% with respect to the supporting piston velocity. Figure 4.14(c) shows the long time behavior at $\overline{u_p} = 1400$ m/s for both the inviscid and viscous cases. The relative maxima in detonation pressure are $p = 35.66 \pm 0.10$ atm and $p = 36.62 \pm 0.005$ atm, for the viscous and inviscid cases, respectively. In addition to the reduction of the maximum detonation pressure, the amplitude of oscillations has also been reduced by 40% by the addition of viscosity. However, as the pulsations become stronger, the effect of viscosity is reduced as demonstrated in Figure 4.14(d) for $\overline{u_p} = 1320$ m/s. The pulsation amplitude reduction due to diffusion is weakened to less than 0.1% near the transition point to the dual mode behavior. Figure 4.14(e) shows the detonation pressure versus time curve for both the inviscid and viscous cases at $\overline{u_p} = 1310$ m/s, which is in the dual mode pulsating behavior in both cases. It is difficult to identify differences in the time domain due to the interacting modes; the frequency domain will be discussed later. The average detonation pressure and the average maximum detonation for the viscous case are $p = 34.32$ atm and $p = 36.2 \pm 0.7$ atm. Likewise for the inviscid case, the average detonation pressure and the average maximum detonation are $p = 34.33$ atm and $p = 36.1 \pm 0.7$ atm. In the low frequency dominated mode the effect of viscosity is nearly negligible, which is demonstrated in Figure 4.14(f) for $\overline{u_p} = 1250$ m/s. The local maxima are $p = 46.5 \pm 0.4$ atm and $p = 46.6 \pm 0.5$ atm, for the viscous and inviscid cases; respectively. This is a relative difference of 0.2%, and it is clear that the maxima overlap.

The PSD spectra are calculated and compared using the average inviscid detonation pressure to scale both the inviscid and viscous detonation pressures; furthermore, the PSD is calculated in decibels using the maximum value of either case. Supporting piston velocities ranging from 1250 m/s to 1500 m/s are shown in Figure 4.15. At $\overline{u_p} = 1500$ m/s, both of the PSD spectra are concentrated around the zero frequency, as shown in Figure 4.15(a), indicating that the detonation is stable at long times. Figure 4.15(b) shows the PSD spectra at $\overline{u_p} = 1430$ m/s; it is clear the inviscid case is pulsating at $\nu_o = 3.60$ MHz, but the viscous PSD is still concentrated around the zero frequency indicating a stable detonation. At $\overline{u_p} = 1400$ m/s, the fundamental frequency in the inviscid case is $\nu_o = 3.36$ MHz, whereas in the viscous case it is minimally shifted to a lower frequency by 1%. The shift is more apparent in the second harmonic, which is shifted by 0.06 MHz. Figure 4.15(c) shows that the magnitude of fundamental frequency is larger in the inviscid case indicating the reduction in pulsation amplitude. The addition of viscosity affects more the size of the pulsation than the frequency of pulsations. Near the transition point to the dual mode behavior, at $\overline{u_p} = 1320$ m/s, the frequency shift is reduced to 0.01 MHz. Figure 4.15(d) indicates that the fundamental frequency peaks in the inviscid and viscous case are closer in magnitude than at the higher supporting piston velocities, giving another indication that the pulsation amplitude is nearly identical. In the dual mode, as shown in Figure 4.15(e) the active modes are only barely distinguishable from each

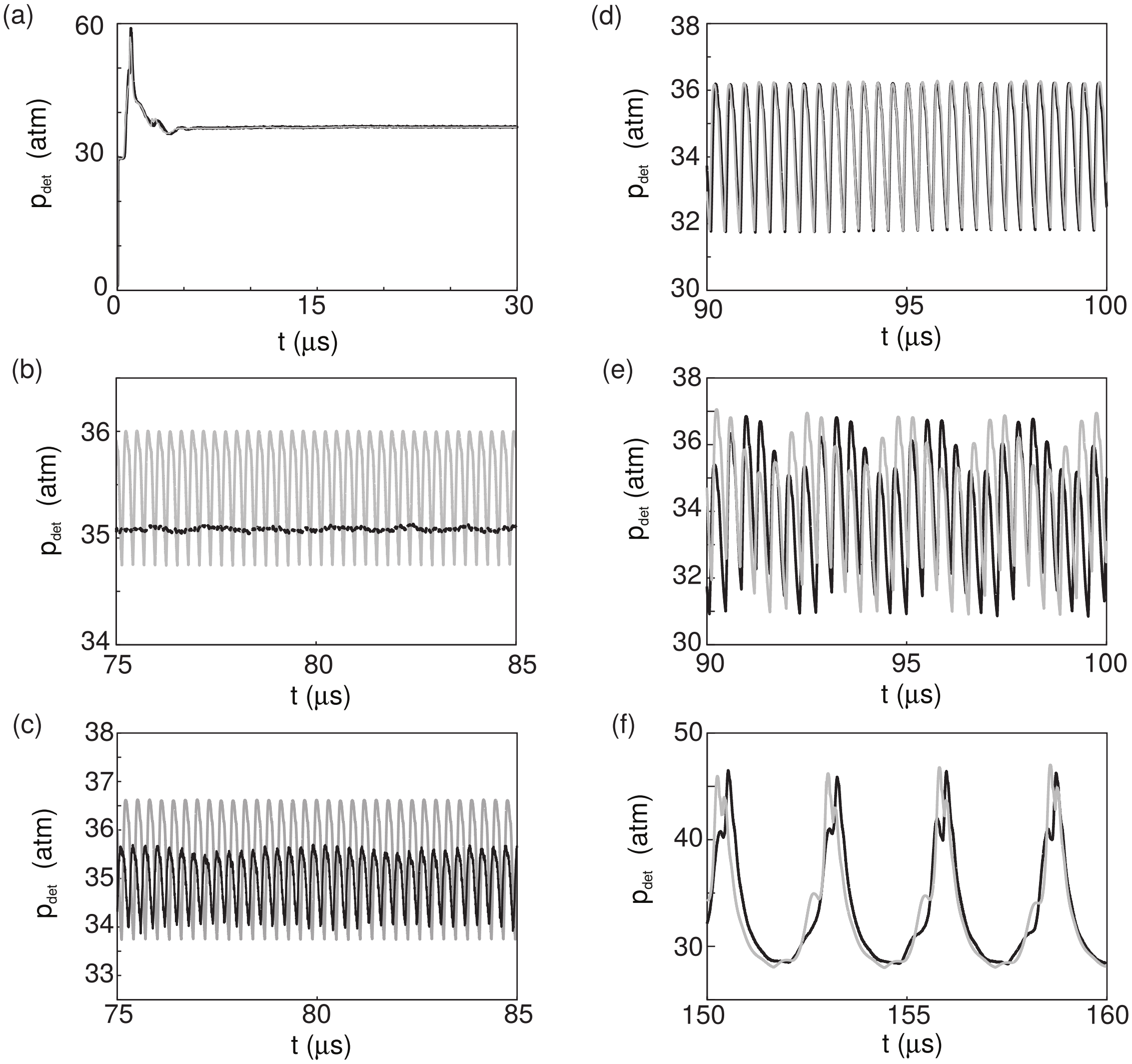

Figure 4.14. Detonation pressure versus time for both viscous (black lines) and inviscid (gray lines) cases at (a) $\overline{u_p} = 1500$ m/s, (b) $\overline{u_p} = 1430$ m/s, (c) $\overline{u_p} = 1400$ m/s, (d) $\overline{u_p} = 1320$ m/s, (e) $\overline{u_p} = 1310$ m/s and (f) $\overline{u_p} = 1250$ m/s.

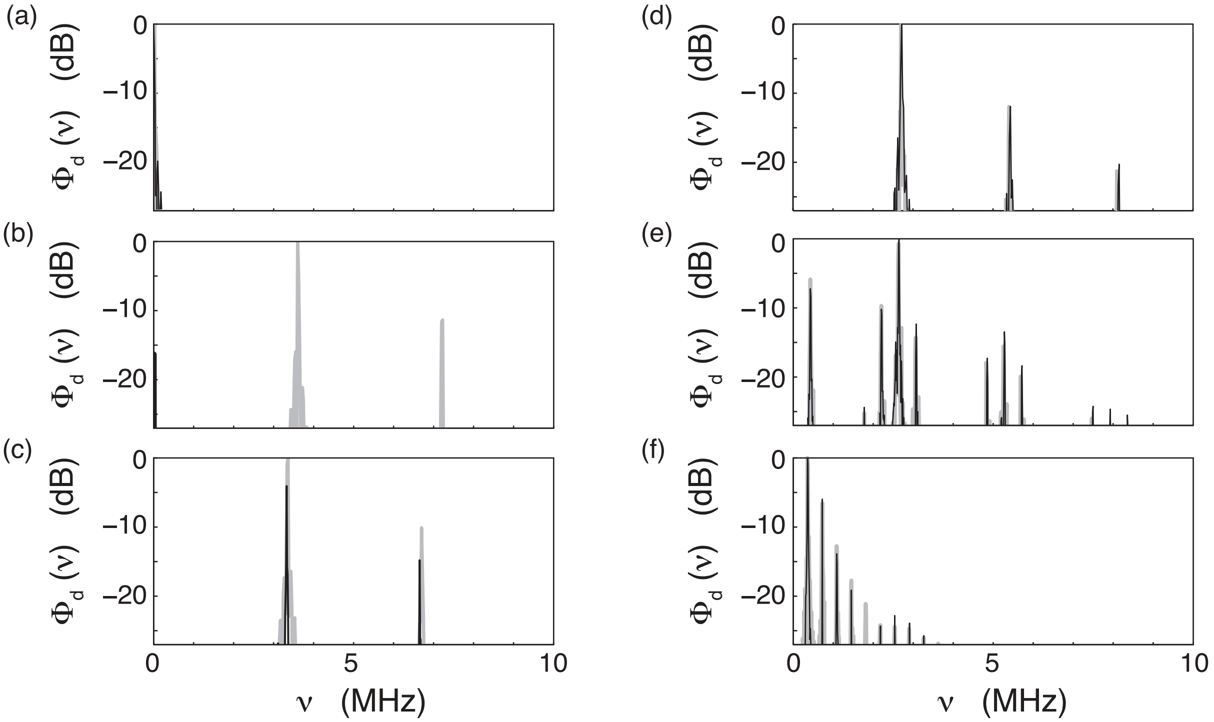

Figure 4.15. PSD spectra for both viscous (black lines) and inviscid (gray lines) cases at (a) $\overline{u_p} = 1500$ m/s, (b) $\overline{u_p} = 1430$ m/s, (c) $\overline{u_p} = 1400$ m/s, (d) $\overline{u_p} = 1320$ m/s, (e) $\overline{u_p} = 1310$ m/s and (f) $\overline{u_p} = 1250$ m/s.

other; however, the strength of the low frequency mode is stronger in the inviscid case, and the high frequency mode is weaker. This indicates that, though small, the addition of physical viscosity to the model is still playing a role and slightly delays the transition to the dual mode behavior. Additionally, the high frequency mode is shifted, but only by 0.3%. When a low-frequency dominated mode ($\overline{u_p} = 1250$ m/s) is examined, it is seen that the PSD spectra, shown in Figure 4.15(f), are nearly indistinguishable from each other. The fundamental frequencies are identical, and as the magnitude of the pulsations are the same, the magnitude of the PSD at this frequency are also identical. However, the PSD for the viscous case is missing the fifth harmonic and has minimally more energy carried at the higher frequencies.

The amplitude reduction present in the high frequency mode is weakened as the supporting piston velocity is lowered. At lower piston velocities the intrinsic instability grows stronger, and thus, the effect of physical viscosity is weaker. The addition of physical viscosity to the model has an overall stabilizing effect, delaying the initial transition to instability and reducing the amplitude of oscillations in the pulsating mode dominated by high frequency oscillations. This suggests that in multiple dimensions, that diffusion can play an important role in the formation and propagation in detonations in narrow channels, where the transverse waves can possibly be damped. The formation of the detonation will be examined with detailed kinetics in Chapter 5. However, the further away from this transition, physical viscosity plays a less important role in determining the long time behavior at least in one dimension.

4.5 Discussion

It is useful to consider a physics-based interpretation of these detailed unsteady detonation dynamics. This interpretation is supported either directly by the current results or plausible hypotheses that could guide future studies. The discussion will be mainly cast in the framework of the current one-dimensional piston-supported detonations in a viscous hydrogen-air mixture; to quantitatively illustrate these important points for viscous limit cycle detonations, an appeal is made to a simpler model of one step kinetics where the CJ limit cycle is well quantified [120]. It is well understood that the compressible reactive Navier-Stokes equations admit steady traveling wave solutions in response to a driving piston. The steady wave is driven by a combination of mechanical energy input from the driving piston and chemical energy input from the exothermic heat release in the subsonic region following the thin lead shock. For sufficiently high piston speeds such that the kinetic energy imparted by the piston is much greater than the chemical energy, the wave behaves similarly to an inert shock wave. As the piston velocity is lowered, the chemical energy makes an ever-increasing relative contribution to driving the wave. At a critical CJ piston velocity, all of the energy to drive the wave is available from the chemical energy, and the wave becomes self-propagating.

These steady waves can respond differently to small perturbations in the various regimes of supporting piston velocity. The key question is whether such perturbations grow or decay, and if they initially grow, what physical mechanisms prevent unbounded growth. In general terms, there are two physical mechanisms present which induce dissipation of structured mechanical and chemical energy into unstructured thermal energy: diffusion and the irreversible part of chemical reaction. Simultaneously, there are physical mechanisms present which induce the growth and resonance of various oscillatory structures predicted in some cases: amplification of selected modes by exothermic reaction combined with the effects of advection and diffusion. Ultimately, nonlinearity has a role. It is often the case that modes which grow linearly away from equilibrium can move into a region where nonlinear effects become important and serve to either suppress further growth or induce some variety of catastrophic growth. The action of these various physical mechanisms is a strong function of the various length and time scales in play as the driving piston velocity is varied.

For sufficiently high piston velocity, the effect of exothermic chemistry is minimal. One might imagine that a small sinusoidal disturbance near the shock front would segregate into one entropic and two acoustic modes, traveling near the local particle and acoustic speeds, respectively. Diffusion would act to reduce the amplitude of the disturbance. High frequency modes would dissipate more rapidly than low frequency modes, but ultimately all would stabilize, and the system would relax to a steady propagating wave. Such is what is predicted for $\overline{u}_p > 1.420 \times 10^3$ m/s.

For lower piston velocities, e.g. 1.400×10^3 m/s, it is obvious that limit cycle-like behavior is predicted. Thus, at this piston velocity, nature favors a partition of the chemical and kinetic energy of the fluid into a pattern in which some of the energy resides in the two modes displayed in figure 4.15(c). Under these conditions, there is little difference between the viscous and inviscid predictions, so it is inferred that the physics are best understood in the context of a reactive Euler model. This piston velocity is likely favorable for the establishment of an organ-pipe type resonance influenced by a balance between reaction and advection. The relevant length is the induction zone, that is, the region between the lead shock and the point where significant chemical reaction commences. Good estimates for a similar mixture are given by Powers and Paolucci [108]. The reaction kinetics are such that the induction zone length $\ell_{ind} \simeq 10^{-4}$ m. The material properties are such that the post-shock acoustic speed $c \simeq 10^3$ m/s. A rough estimate of the fundamental resonant frequency is thus $\nu \simeq c/\ell_{ind} = 10$ MHz. This is of the same order of magnitude as that predicted. This scaling argument is consistent with the results of Short [133], who showed that perturbations within the induction zone were linearly unstable while examining one step square wave detonations at high activation energy. Moreover for this case, figure 4.15(c) reveals that diffusion induces a small amplitude reduction in the resonant modes, as well as a small shift in the resonant frequencies. This is consistent with what is found in ordinary nonlinear mass-spring-damper systems [144]. Again, similar to what is found in a nonlinear mass-spring-damper system, it is most likely that nonlinear effects serve a much stronger role in suppressing the growth of the resonant modes. For higher frequency modes, it is likely that diffusion plays the dominant role in amplitude suppression. With the finest length scale of reaction given by Powers and Paolucci [108] for this mixture $\ell_{finest} \simeq 10^{-6}$ m, and the diffusivity of the mixture $D_{mix} \simeq 10^{-3}$ m^2/s, one can estimate the frequency of the disturbance for which diffusion clearly dominates as $\nu \simeq D_{mix}/\ell_{finest}^2 = 1$ GHz. Useful insights on the relative importance of advection, reaction, and diffusion in hydrogen-air chemistry is given by Al-Khateeb et al. [2] in the context of a laminar flame. There, it is shown that diffusion clearly influences the various reaction time scales on length scales given by a classical Maxwellian model, $\ell_i \simeq \sqrt{D_{mix}\tau_i}$, where ℓ_i is the reaction length scale associated with the chemical time scale τ_i.

As the piston velocity is lowered further, nonlinearity plays a more prominent role, especially as seen in figures 4.11(d) and 4.12(a-d). As the oscillatory modes are dominated here by ever-lower frequencies as the piston velocity is lowered, it is likely that diffusion is playing even less of a role in the dominant low frequency dynamics, with its main effect being confined to much higher frequency modes. Even then, the presence of diffusion is important in providing a physically based cutoff mechanism for high frequency modes. As documented by Powers [107], lack of such a cutoff mechanism can then admit approximations which do not converge as the grid discretization scale is reduced, thus rendering the results to be potentially strongly influenced by the size of the discretization and the selected numerical method. Moreover, Mazaheri et al. [85] demonstrated that, in regions that have large gradients in the flow, diffusion plays an influential role.

As it is prohibitively expensive to fully relax detonations with detailed kinetics to limit cycles, these notions of piston-driven detonations are verified using a one

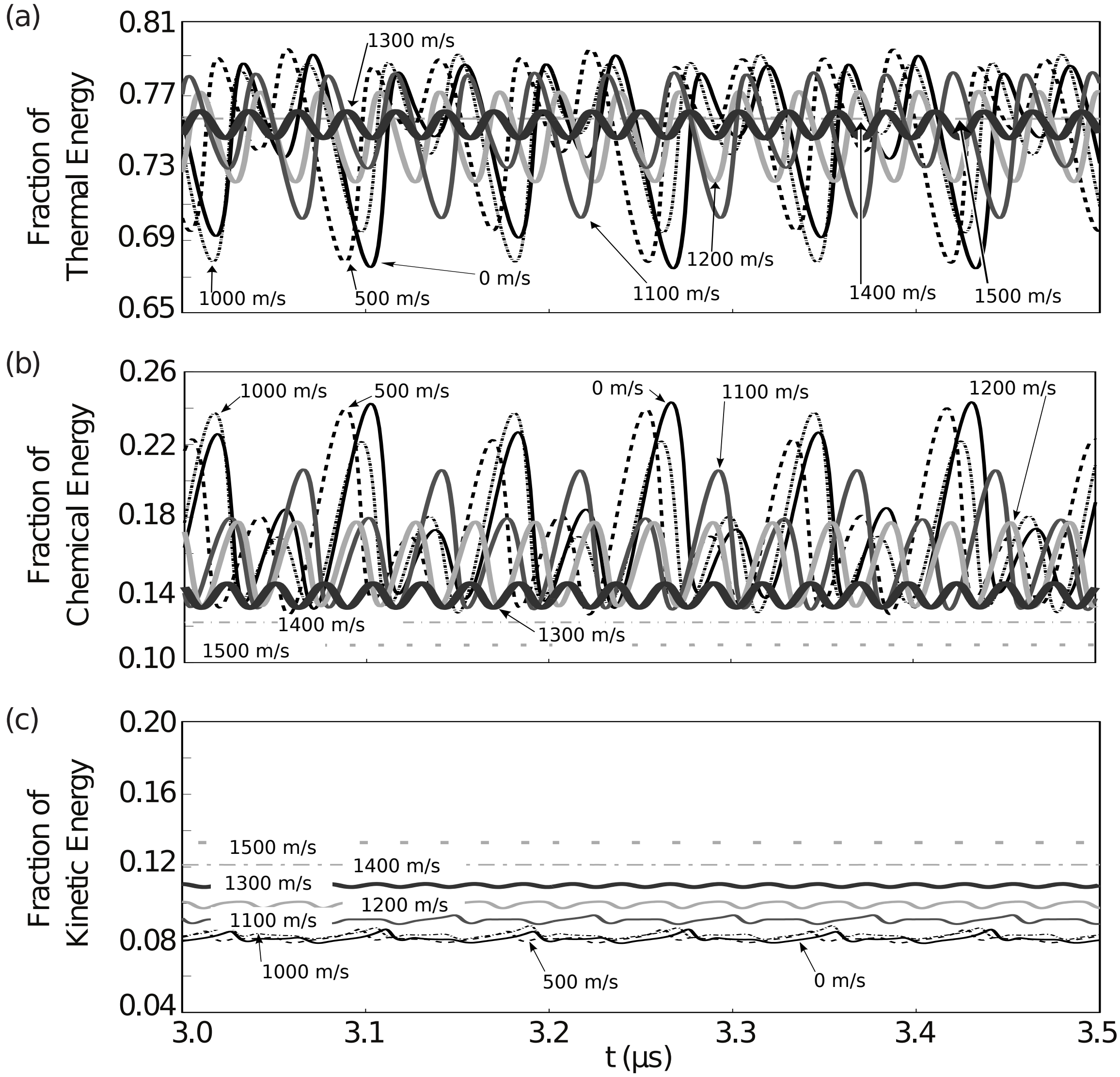

Figure 4.16. Fraction of total energy within the integration domain for (a) thermal, (b) chemical, and (c) kinetic energies in the one step model with $E_a = 29.98$ for several piston velocities.

step viscous detonation model previously examined by Romick et al. [120] in the CJ limit. Here, a simple study was performed at several piston velocities, for a fixed non-dimensional activation energy of $E_a = 29.98$ which predicted a period-4 detonation in the CJ case. As the focus of this examination is the energy composition driving the detonation at late times, only a domain near the front traveling at an average detonation velocity is considered. The domain is taken to be sufficiently large to encompass several half-reaction zone lengths. This domain has chemical energy entering from the unreacted ambient upstream conditions. Energy leaves the domain behind the front due mainly to thermal energy released from the reaction, as well as a small contribution from energy associated with viscous stresses. Additionally, depending on the magnitude of the piston velocity, kinetic energy either propagates out of the domain or enters the domain emanating from the energy inputted from the piston. However, only the composition of energy within this domain is of interest in this case; thus, by integrating the individual amounts of these three (thermal, chemical, and kinetic) energies as well as the sum over this domain at each time, the evolution of the energy composition driving the detonation at the different piston velocities can be obtained. The sum of the energies in the domain can be written as:

$$E(t) = \int_{x_1}^{x_1+L_d} \left(\rho c_v T + \rho \left(1 - \lambda\right) q_r + \rho \frac{u^2}{2} \right) \, dx, \tag{4.9}$$

where $E(t)$ is the total energy per unit area in the domain, x_1 the position of the left end of the domain, L_d the fixed length of the domain, c_v the specific heat at constant volume for the mixture in this one step model, λ the reaction progress variable, and q_r the heat release per unit mass of the reaction. The total domain length chosen for integration is 50 steady half-reaction zone lengths with 35 steady half-reaction zone lengths behind the front at the peak detonation velocity in the late time behavior. This choice allows for an almost complete reaction to occur within the domain at any period of the cycles predicted.

Figure 4.16 shows the fraction of the total energy each component carries for piston velocities of $\overline{u}_p = 0.0,\ 0.5,\ 1.0,\ 1.1,\ 1.2,\ 1.3,\ 1.4,\ 1.5 \times 10^3$ m/s in the late time behavior of the propagating detonation. In the ZND profile for this activation energy, the CJ particle velocity is $\sim 960 \times 10^5$ m/s; therefore, it is anticipated piston velocities above this velocity would have an effect on the late time behavior. The majority of the energy is carried in the thermal mode due to the energy released by the reaction, depicted in figure 4.16(a), with all piston velocities predicting a mean contribution near 75.5% of the total energy. At sufficiently high piston velocities, a stable detonation is formed. This can be most easily seen in figure 4.16(b) and (c), where the chemical and kinetic modes are shown, respectively. In figure 4.16 the light gray dashed horizontal lines are for the highest piston velocities. For these stable detonations, the kinetic mode carries more energy than the chemical mode due the high piston velocities. However, as the final piston velocity is lowered, a period-1 detonation propagates at late times as seen in figure 4.16 by the thick dark gray curve for $\overline{u}_p = 1.3 \times 10^3$ m/s and the solid light gray curve for $\overline{u}_p = 1.2 \times 10^3$ m/s. Furthermore, at the higher piston velocity $\overline{u}_p = 1.3\times10^3$ m/s, the kinetic and chemical modes are nearly identical in magnitude.

At an even slower piston speed, a period-2 detonation is predicted, depicted by the thinner dark gray curve. In this case, $\overline{u}_p = 1.1 \times 10^3$ m/s, the chemical mode is now dominant over the kinetic mode. Moreover, the ratio between the chemical and kinetic modes at its maximum is 2.24. The lowest three piston velocities examined, $\overline{u}_p = 0.0,\ 0.5,\ 1.0 \times 10^3$ m/s, exhibit period-4 CJ behavior. The separations between these CJ detonations are almost exclusively temporal offsets, and the curves would nearly be coincident if these offsets were removed. As the $\overline{u}_p = 1.0 \times 10^3$ m/s case is minutely above the CJ particle velocity for the ZND profile, there is only a weak contribution from the piston affecting the energy composition. These piston velocities are shown in figure 4.16 by the solid, dashed, and dashed-dotted curves, respectively. For the CJ case, which is present for the $\overline{u}_p = 0.0,\ 0.5 \times 10^3$ m/s cases, the maximum ratio between chemical and kinetic modes grows to 2.95 which is the maximum for this particular activation energy.

As discussed earlier, identifying the beginning and end of the limit cycle is challenging for multistep kinetics. However, given sufficiently long computation time it is presumed that fully relaxed limit cycles would be predicted. Therefore, it is hypothesized that these explanations which hold for one step kinetics also extend to multistep kinetics.

CHAPTER 5

ACCELERATION OF HYDROGEN-OXYGEN FLAMES IN NARROW CHANNELS

5.1 Introduction

In this chapter, a two-dimensional investigation into flame acceleration in a channel with smooth no-slip walls is performed for premixed $H_2 - O_2 - N_2$ mixtures. The aim is to gain a greater understanding into the acceleration of hydrogen-oxygen flames in channels and the possible DDT. This study will give insight into the effects of channel width and amount of diluent in the mixture on the rate of acceleration of the flame. These type of flows are relevant for safety issues due to the high laminar flame speeds, the relatively low ignition energy, and the amount of destruction a detonation can cause. Moreover, the diffusive processes can play a crucial role in flame acceleration. This work aims to broaden the knowledge of the hydrogen-oxygen flame acceleration in channels in several ways: 1) examining narrow channels, 2) the effect of varying diluent, and 3) to try to provide bounds on the formation and propagation by studying both adiabatic and ambient temperature isothermal no-slip walls.

The chapter is organized as follows. In Section 5.2, the mathematical model is presented along with a brief description of the computational method and physical problem. Next in Section 5.3, an examination of flame accelerations in channels with no-slip walls is performed. First, the effect of varying the channel width is explored; this is followed by a study on the effect of the amount of diluent in the mixture. Lastly, a brief investigation into the formation of a flame in the presence of adiabatic and isothermal walls is presented.

5.2 Formulation

5.2.1 Mathematical Model

The model equations taken here are the two-dimensional version of Equations (2.1)-(2.4). The diffusive transport relations adopted in this chapter are Equations (2.30), (2.31), and (2.32) for mass, momentum, and energy diffusion, respectively. To initialize a flame in the initially cool quiescent fluid, a transient thermal power deposition pulse, which weakly approximates a spark, Q, is used. The specific form used will be discussed further in Section 5.2.3. Thus with the addition of the initialization energy source, the governing energy equation becomes

$$\frac{\partial}{\partial t}\left(\rho\left(e+\frac{\mathbf{u}\cdot\mathbf{u}}{2}\right)\right)+\nabla\cdot\left(\rho\mathbf{u}\left(e+\frac{\mathbf{u}\cdot\mathbf{u}}{2}\right)+(p\mathbf{I}-\boldsymbol{\tau})\cdot\mathbf{u}+\mathbf{q}\right)=\mathsf{Q}. \tag{5.1}$$

Additionally, the constitutive equations are listed in Section 2.2. The reaction and mixture properties are evaluated using the `CHEMKIN` package [63], and the diffusive transport coefficients are evaluated using the `TRANSPORT` package [62].

5.2.2 Computational Method

The Wavelet Adaptive Multiresolution Representation (WAMR) method in combination with an error-controlled nominally fifth order Runge-Kutta scheme for temporal integration was used to perform the flame acceleration calculations. The calculations were performed using a threshold of $\epsilon = 10^{-3}$. Several mixtures and channel widths are investigated in this study. Thus to illustrate the computational requirements for these type of calculations an example for a mixture of $0.6H_2+0.3O_2+0.1N_2$ will be presented. The selection of $\epsilon = 10^{-3}$ leads to a necessary spatial resolution of $\mathcal{O}(2\times10^{-7}$ m) during the flame propagation stage which results in a time step of $\mathcal{O}(8\times10^{-11}$ s). Moreover, the total number of collocation points utilized during early flame propagation depends on the channel width examined. The number of points generally ranged between $\mathcal{O}(2\times10^5)$ to $\mathcal{O}(5\times10^5)$. During the later flame acceleration stage as the pressure builds, the necessary spatial resolution shifts to $\mathcal{O}(1\times10^{-8}\text{ m})$ which results in a time step of $\mathcal{O}(1\times10^{-12}\text{ s})$. Likewise, the total number of points also increases, with a range of $\mathcal{O}(4\times10^5)$ to $\mathcal{O}(2\times10^6)$. This results in a simulation time of ~ 1 μs between $\mathcal{O}(3.5\times10^3\text{ CPUhrs})$ and $\mathcal{O}(2.25\times10^5\text{ CPUhrs})$ on 512 Intel Xeon 2.6 GHz cores with 16 cores per node and an Infiniband connection between the nodes.

5.2.3 Problem Parameters

In this study, a series of two-dimensional flame acceleration flows in initially quiescent premixed hydrogen-oxygen-nitrogen mixtures at ambient conditions of 298.15 K and 1 atm is considered. The detailed kinetics mechanism employed is the same used by Powers and Paolucci [108], in Chapter 4, and is drawn from Miller et al. [89]. It contains 9 species, 3 elements and 19 reversible reactions where nitrogen is treated as a non-reacting diluent species and is shown in Table 4.1.

The computational domain is a rectangular channel with no-slip walls at the bottom and top surfaces, and a symmetry condition is applied at the left surface. The right boundary surface is a no-slip surface, but the domain length is chosen such that the acoustic waves do not reach the right end of the domain. The left symmetric boundary condition was chosen instead of a no-slip wall, as a corner created from two perpendicular no-slip walls creates a singularity in density in compressible flow; this leads to computational difficulties for the WAMR method. Furthermore as the reflections off the top and bottom boundaries have minimal effect on the formation, propagation, and acceleration of the flame, it is likely that the possible reflection would have little to no effect. Both adiabatic and isothermal walls are examined. These boundary conditions are detailed further next and are shown in Figure 5.1.

The no-slip wall boundary condition consists of a mixture particle velocity equal

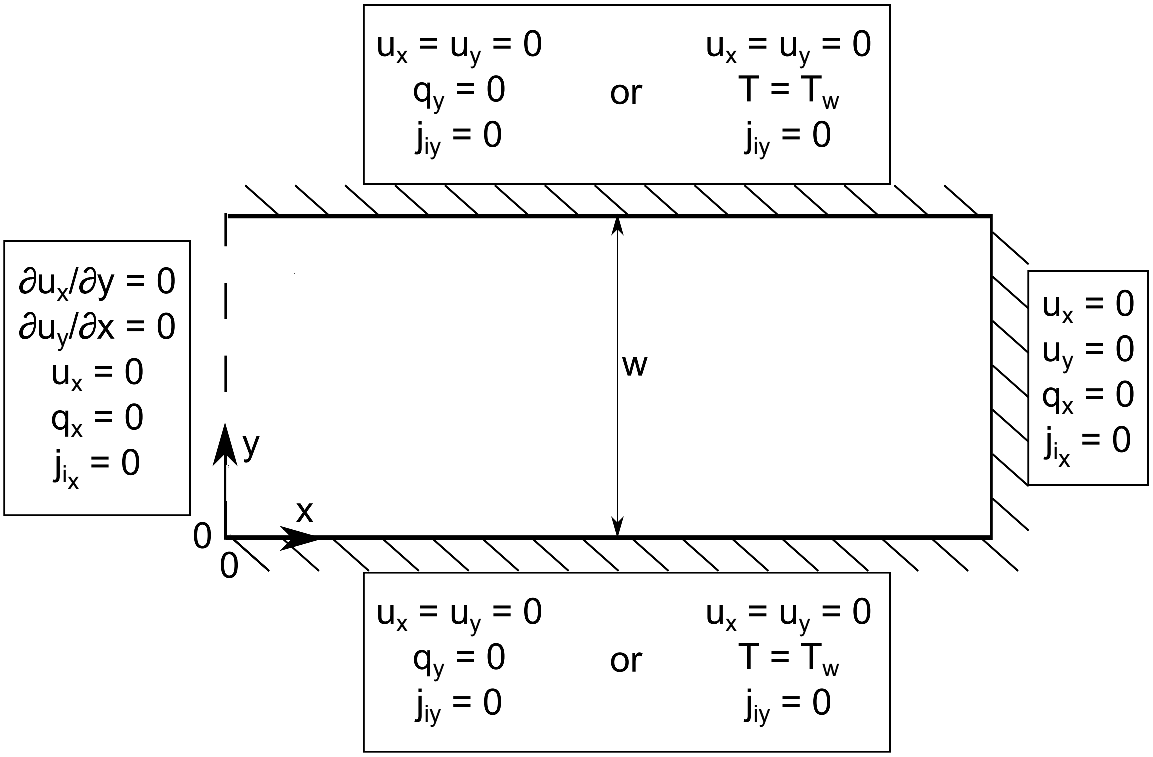

Figure 5.1. The channel's boundary conditions for the flame acceleration cases examined.

to the wall velocity, for this work the wall velocity is zero, $u_t = u_n = 0$, where u_t and u_n are the velocities in tangential and normal directions. Additionally in this work, the walls are taken to be impermeable and solid, thus no normal mass flux is allowed through, $j_{i_n} = 0$. Finally, a condition on energy is necessary, and therefore, a normal heat flux or a wall temperature can be specified. In the case of an adiabatic wall there is null normal heat flux $q_n = 0$, and in the case of isothermal wall, the fluid temperature is equal to the constant wall temperature, $T_f = T_w$. As there are no-slip walls parallel to each other along the x-horizon, the tangential and normal direction for these walls are the x- and y-directions, respectively. However for the no-slip wall at the right boundary, the tangential and normal directions are the y- and x-directions, respectively. These tangential and normal directions are shown in Figure 5.1.

All of the conditions but the last can be directly applied to the governing equations except for the isothermal condition. The mixture temperature does not explicitly appear in the governing equations and must be found through an iterative process using internal energy as mentioned in Section 2.2. As such the isothermal condition must be applied using the energy equation. Utilizing the no-slip solid wall velocity conditions ($u_x = u_y = 0$), the time dependency term of the energy equation can be reduced

$$\frac{\partial}{\partial t}\left(\rho\left(e + \frac{u_i u_i}{2}\right)\right) = \frac{\partial}{\partial t}\left(\rho e\right), \tag{5.2}$$

and by using the definition of the mixture internal energy, Equation (2.23), this becomes

$$\frac{\partial}{\partial t}\left(\rho\left(e + \frac{u_i u_i}{2}\right)\right) = \frac{\partial}{\partial t}\left(\rho\left(\sum_{i=1}^{N} Y_i e_i\right)\right). \tag{5.3}$$

The internal energy of the i^{th} specie is only a function of temperature, which is constant at the wall; therefore,

$$\frac{\partial}{\partial t}\left(\rho\left(e+\frac{u_i u_i}{2}\right)\right)=\sum_{i=1}^{N}\left(e_i\frac{\partial}{\partial t}\left(\rho Y_i\right)\right). \tag{5.4}$$

This means the time evolution of the energy equation along the isothermal no-slip wall can be evaluated using the evolution of the species.

At a symmetry surface, all of the normal gradients of flow variables vanish. Thus, both the normal velocity, $u_n = 0$, and the shear stress in the normal direction, $\partial\left(u_t\right)/\partial x_n = 0$, vanish; by utilizing the symmetry of the viscous stress tensor, the shear stress in the tangential direction, $\partial\left(u_n\right)/\partial x_t = 0$, vanishes. Moreover, both the normal mass flux, $j_{i_n} = 0$, and normal heat flux, $q_n = 0$, also vanish. As the symmetry boundary in along the vertical direction, the tangential and normal directions are the y- and x-directions, respectively. These tangential and normal directions are also shown in Figure 5.1.

These flows are initiated using a transient thermal power deposition pulse situated at the left boundary in the form of

$$\begin{aligned}\mathsf{Q}=\frac{\rho_o a_o^2}{8t_a}&\left[\tanh\left(\frac{5}{2t_a}\left(2t-t_a\right)\right)-\tanh\left(\frac{5}{2t_a}\left(2t-2\mathsf{t}_m t_a\right)\right)\right]\times\\ \sin&\left(\frac{\pi}{8}\left\{\left[\tanh\left(4\left(\frac{(x-x_c)}{L_x}+2\right)\right)-\tanh\left(4\left(\frac{(x-x_c)}{L_x}-2\right)\right)\right]\times\right.\right.\\ &\left.\left.\left[\tanh\left(4\left(\frac{(y-y_c)}{L_y}+2\right)\right)-\tanh\left(4\left(\frac{(y-y_c)}{L_y}-2\right)\right)\right]\right\}\right),\end{aligned} \tag{5.5}$$

where a_o is the ambient sound speed, ρ_o the ambient density, L_x the characteristic length scale of the deposition in the x-direction, L_y the characteristic length scale of the deposition in the y-direction, x_c the center of the deposition in the x-direction, y_c the center of the deposition in the y-direction, t_a the acoustic time scale associated with L_x, and $\mathsf{t_m}$ the number of acoustic time scales over which deposition is applied. This form is similar to that used by [60, 61, 118] in their one-dimensional DDT studies using the one step model. The chosen form weakly approximates a spark and gives rise to mild inertial confinement, leading to a moderately localized pressure increase in spite of simultaneous expansion. This is due to the time scale of heat addition being of a similar magnitude to the local ambient acoustic time scale. Eventually, behind this pressure pulse, a reaction wave begins to form. This initial pressure pulse spreads to fill the full channel width and decays as it propagates down the channel away from the source. The trailing reaction wave either develops into a flame front trailing the weak leading pressure wave or given insufficient initialization energy decays to extinction.

In this work, the center of the deposition is positioned on the symmetry boundary at the center of the channel $(x_c = 0,\ y_c = w/2)$. The characteristic lengths for this work were $L_x = 5$ μm and $L_y = w/5$; this yields a 80% filling of the channel width no matter the width. Therefore, the percentage of energy deposited into the system remains the same across all widths examined enabling easier comparison. The total number of acoustic time scales over which the energy is deposited was 100. These choices allow for the enough energy to be deposited for the establishment of a symmetric flame in both the narrowest and widest cases examined with adiabatic walls.

The investigation into the effect of channel width was performed using an initial mixture of $0.6H_2+0.3O_2+0.1N_2$. For this mixture, the ambient acoustic speed is $a_o =$ 505.15 m/s and thus, the acoustic time scale is $t_a \approx 10^{-2}$ μs. This initial channel study includes widths of $w = [100, 200, 400, 800]$ μm. This will be later expanded to include channel widths of $w = [150, 160, 170, 180, 190, 250, 300, 1600]$ μm. The examination into the effect of varying the amount of diluent was performed in a 800 μm wide channel. In this study, all of the mixtures examined combined hydrogen and oxygen in the molar stoichiometric ratio of 2 : 1 with the molar percentage of nitrogen varying from $[1\%, 10\%, 25\%, 40\%, 55.6\%]$; this last case is a stoichiometric mixture of

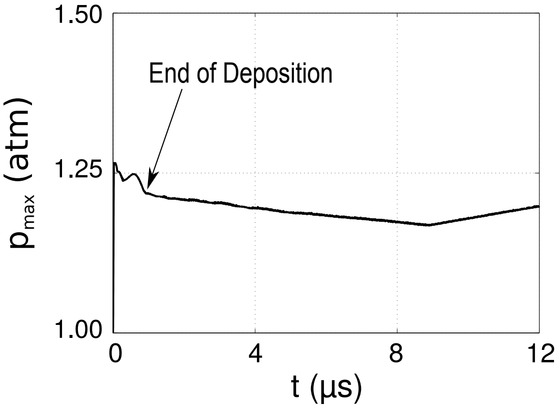

Figure 5.2. The maximum pressure in a 200 μm wide channel versus time during and shortly after the energy deposition for initializing the flame for an initial mixture of $0.6H_2 + 0.3O_2 + 0.1N_2$.

hydrogen and air. In the limited study using ambient temperature isothermal walls of the initialization stage of the flame the original channel widths and initial mixture were again used.

5.3 Results and Discussion

As mentioned previously in Section 5.2.3, the energy deposition creates an initial small pressure pulse which then begins to decrease, as demonstrated in Figure 5.2 for a 200 μm wide channel for a mixture of $0.6H_2 + 0.3O_2 + 0.1N_2$. The maximum pressure within the domain during the deposition and initialization of the flame is 1.28 atm. There are oscillations due to the initial reflections of the initial pressure wave propagating out from the region of energy deposition. These are then significantly attenuated by viscous effects, for this particular case by $t = 2$ μs. This initial pressure pulse continues to decrease until ~ 10 μs. After this decaying stage, the maximum pressure shifts from the leading front of the pressure pulse to the flame front.

This shift is demonstrated in Figure 5.3, which shows three snapshots in time at

(a) $t = 8$ μs, (b) $t = 10$ μs, and (c) $t = 12$ μs of pressure and Y_{OH} on the top and bottom halves of the channel, respectively. Due to the symmetry of the problem, the flow variables would be mirrored across the centerline; thus, to reduce the space taken by figures, only half of the full channel will be presented. The mass fraction of OH was chosen as its maximum gives a good indication of the end of the induction zone. The leading pressure pulse decays due to both the spreading of the energy and viscous dissipation from the front interacting with the no-slip walls as it propagates along the channel; whereas the pressure grows at the flame front due to compression of the fluid as the flame begins to accelerate slowly.

The pressure at the flame front grows in a initially slow manner up until $t \approx 40$ μs, as seen in Figure 5.4(a). This growing pressure pulse sends acoustic waves towards the leading pressure front. As the pressure builds at flame front, stronger and stronger acoustic waves are sent towards the leading front. These acoustic waves coalesce and form a weak leading shock ahead of the flame front. After the pressure pulse has grown slowly to a substantial size, there is a transition in behavior and the pulse begins to grow exponentially. As this flame's pressure grows exponentially, the maximum particle velocity also increases accelerating the flame and increasing the strength of the leading shock. The maximum particle velocity of the domain shifts to the centerline of the flame front at $t \approx 8$ μs, which is similar to when the pressure shifts; from $t \approx 40$ μs to $t \approx 70$ μs, the nonlinear interaction between reactive, advective, and diffusive processes manifests itself in nearly linear growth of the maximum particle velocity, as demonstrated by the Mach number (Ma) versus time curve shown in Figure 5.4(b).

Even though the flame front is stretched near the boundaries due the reduction in the mixture particle velocity in the boundary layer, as indicated by the Y_{OH} plots in the lower halves of Figure 5.5, the pressure pulse at the flame front remains nearly constant across the channel. Additionally during the buildup, the pressure at front

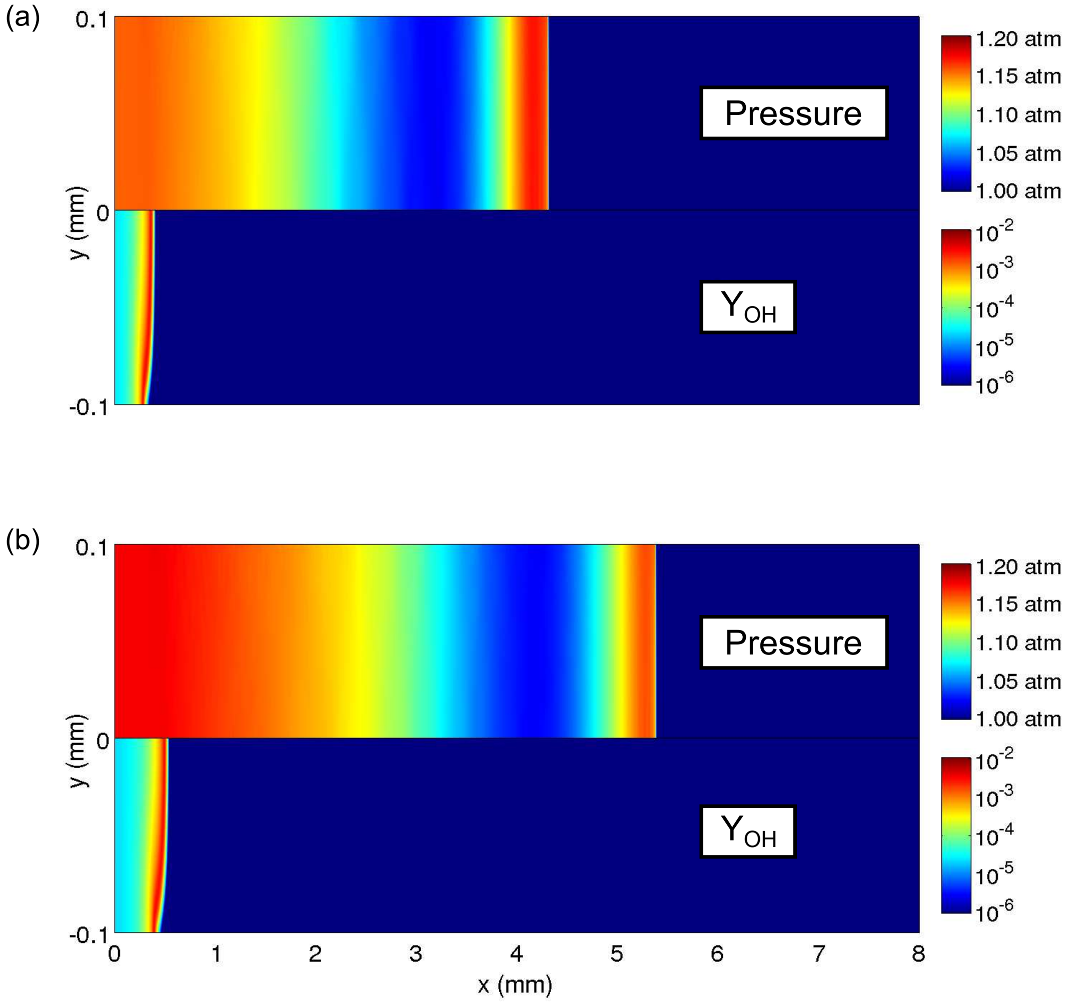

Figure 5.3. The pressure (upper half of channel) and Y_{OH} (lower half of channel) flow fields at (a) $t = 8$ μs, (b) $t = 10$ μs, and (c) $t = 12$ μs for an initial mixture of $0.6H_2 + 0.3O_2 + 0.1N_2$ in a 200 μm wide channel (continued on page 102).

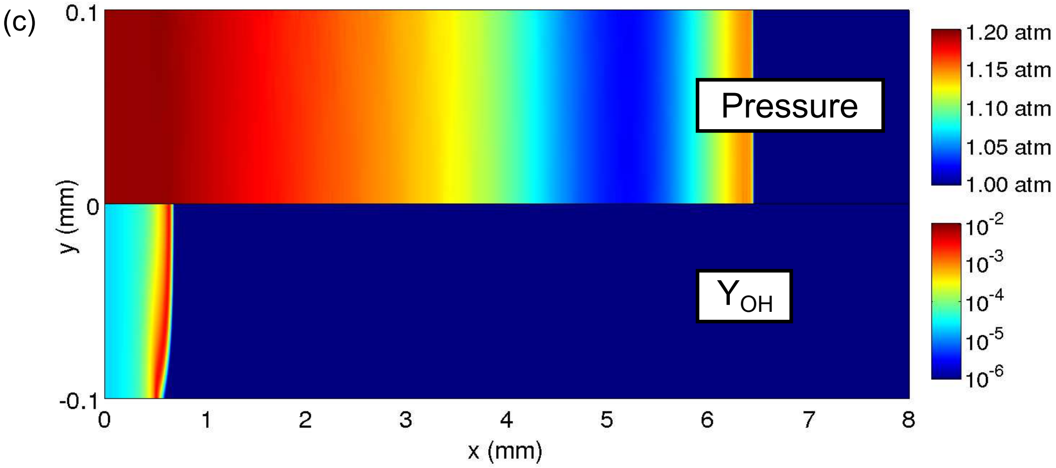

Figure 5.3. The pressure (upper half of channel) and Y_{OH} (lower half of channel) flow fields at (a) $t = 8$ μs, (b) $t = 10$ μs, and (c) $t = 12$ μs for an initial mixture of $0.6H_2 + 0.3O_2 + 0.1N_2$ in a 200 μm wide channel (continued from page 101).

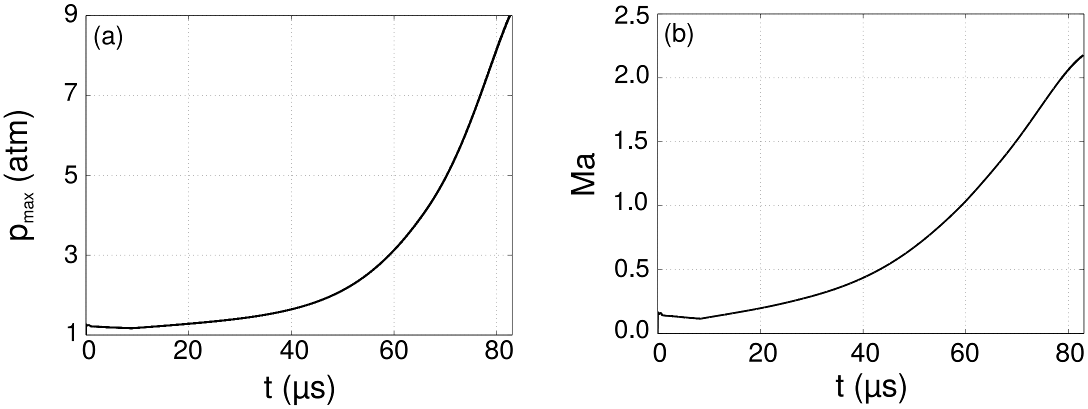

Figure 5.4. (a) The maximum pressure and (b) the maximum Mach number in a 200 μm wide channel versus time for an initial mixture of $0.6H_2 + 0.3O_2 + 0.1N_2$.

weak shock also remains nearly constant across the channel, as shown in the upper halves at the channels in Figure 5.5 at (a) $t = 52$ μs, (b) $t = 62$ μs, (c) $t = 72$ μs, and (d) $t = 82$ μs.

This stretching of the flame near the boundaries due to velocity boundary layer is further elucidated by examining the temperature and x-velocity profiles, which are shown in Figure 5.6 at (a) $t = 62$ μs and (b) $t = 82$ μs. The high temperature contours curve towards the back of the channel as edges are dragged along by the bulk flow in the center of the channel until the second shock is formed. Moreover from the velocity field, it is clear that a second shock front has been created behind the weak leading pressure wave near the flame front. Once this second shock forms, a heating along the adiabatic no-slip walls begins helping the flame to accelerate faster; these two-dimensional effects will be discussed further in Section 5.3.1 and eventually compared to an infinitely wide channel.

5.3.1 Effect of Channel Width

The $0.6H_2{+}0.3O_2{+}0.1N_2$ mixture was examined further in several channel widths. Figure 5.7 shows the maximum pressure versus time curves for channel widths of $w = [100, 200, 400, 800]$ μm. As the channel width decreases from 800 μm (indicated by the thin, dashed, black line) to 200 μm (indicated by the thick, light gray line), the time for the pressure pulse to build to 3.5 atm is dramatically reduced from $t = 417.2$ μs to $t = 62.6$ μs. This growth in the pressure coincides with an increase in the mixture particle velocity and thus, an acceleration of the flame front. This trend is in agreement with the work in a pure hydrogen oxygen mixture studied by Ivanov et al. [54]. The increase in the rate of pressure buildup, which is exponential in nature, is likely caused by the conversion of the mechanical energy of the leading pressure pulse and forward moving acoustic waves emanating from the flame front to thermal energy being trapped in a narrower channel by the adiabatic walls. This

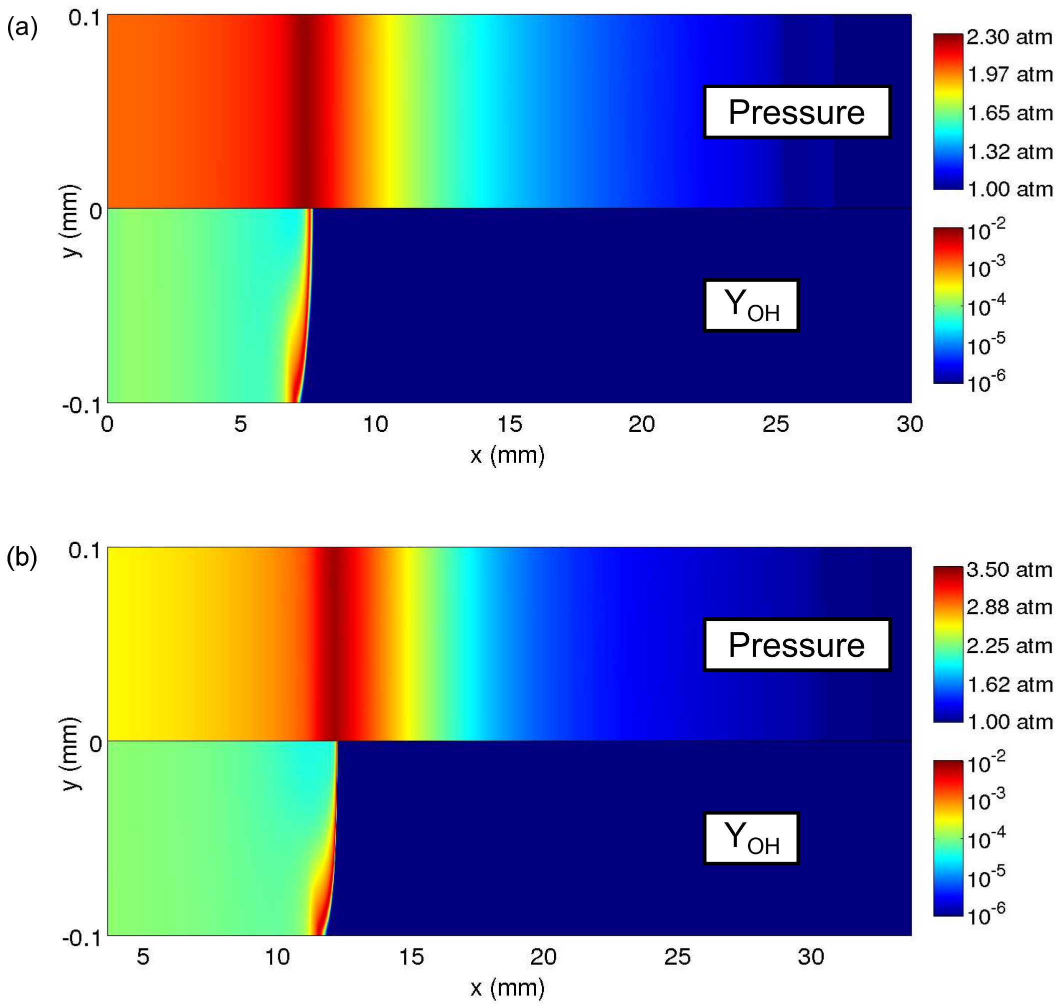

Figure 5.5. The pressure (upper half of channel) and Y_{OH} (lower half of channel) flow fields at (a) $t = 52$ μs, (b) $t = 62$ μs, (c) $t = 72$ μs, and (d) $t = 82$ μs for an initial mixture of $0.6H_2 + 0.3O_2 + 0.1N_2$ in a 200 μm wide channel (continued on page 105).

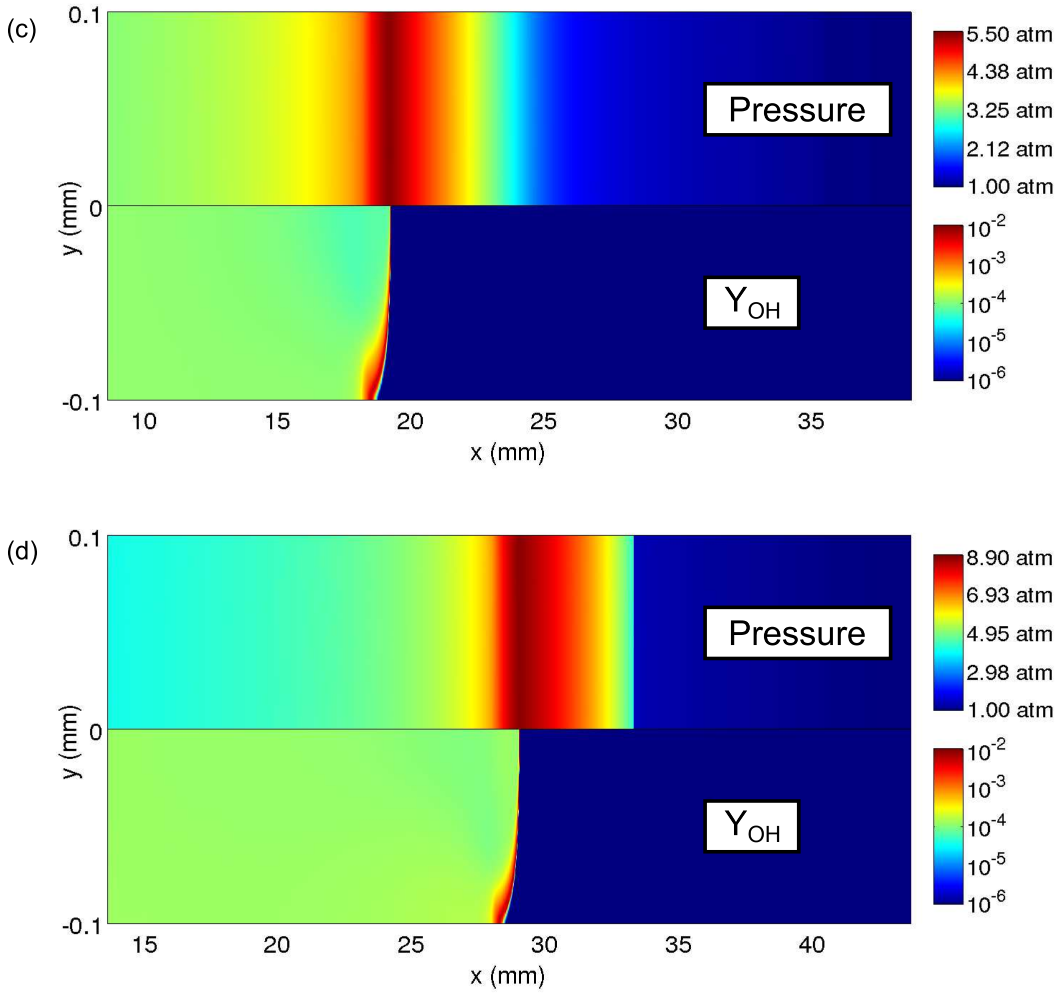

Figure 5.5. The pressure (upper half of channel) and Y_{OH} (lower half of channel) flow fields at (a) $t = 52$ μs, (b) $t = 62$ μs, (c) $t = 72$ μs, and (d) $t = 82$ μs for an initial mixture of $0.6H_2 + 0.3O_2 + 0.1N_2$ in a 200 μm wide channel (continued from page 104).

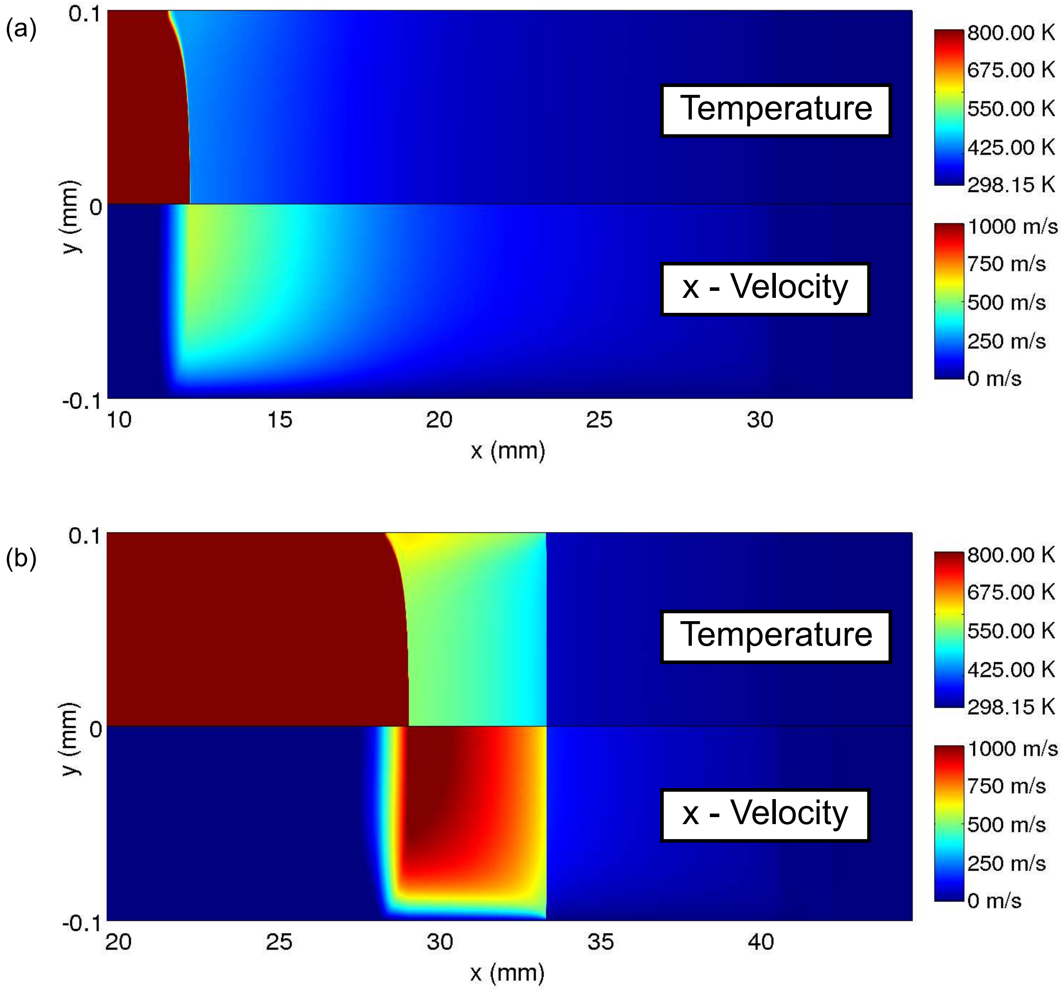

Figure 5.6. The temperature (upper half of channel) and x-velocity (lower half of channel) flow fields at (a) $t = 62$ μs and (b) $t = 82$ μs for an initial mixture of $0.6H_2 + 0.3O_2 + 0.1N_2$ in a 200 μm wide channel.

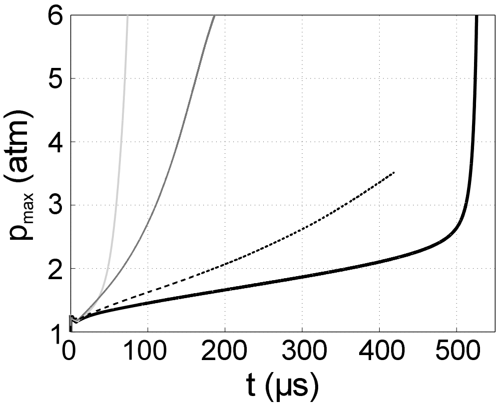

Figure 5.7. The maximum pressure versus time for an initial mixture of $0.6H_2 + 0.3O_2 + 0.1N_2$ in channels with widths of 100 μm (solid, black line), 200 μm (light gray line), 400 μm(dark gray line), and 800 μm (dashed, black line).

idea will be examined further with a simulation with isothermal walls at early time in Section 5.3.3.

However, in the narrowest case shown in Figure 5.7, $w = 100$ μm, there is a significant delay in the pressure pulse growth. This indicates that below some threshold in channel width, the capillary effects of viscosity become more important. In this capillary channel, there are two distinct phases. The first is a very slow growth phase followed by an exponential phase. The delay of the flame acceleration when compared with wider channels, is due to more of the channel being affected by the no-slip wall boundaries. This adds a significant percentage of viscous resistance to the acceleration of the flame.

This slowing of the pressure buildup is more clearly seen in Figure 5.8, which shows the maximum pressure versus time for $w = [100, 150, 160, 170, 180, 190, 200, 250, 300]$ μm channels. The transition between the flows dominated by viscous resistance (narrow channels) and the flows with a mainly slow exponential growth of the flame's pressure pulse occurs between the $w = 200$ μm (indicated by solid, light gray curve) case and $w = 250$ μm (indicated by thin, medium gray curve) case for

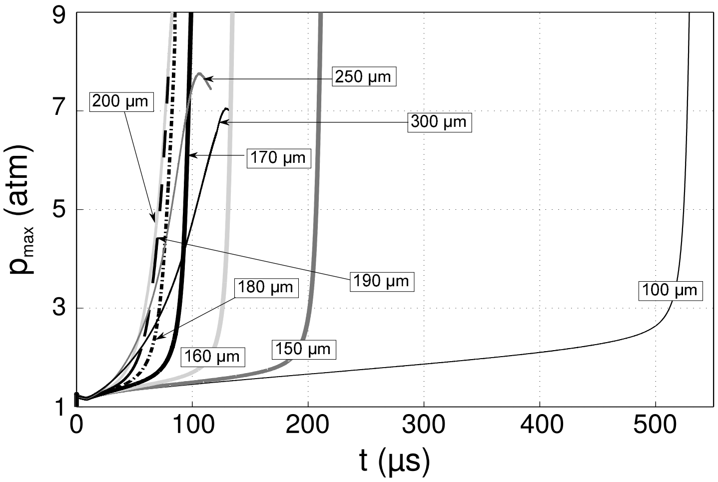

Figure 5.8. The maximum pressure versus time for an initial mixture of $0.6H_2 + 0.3O_2 + 0.1N_2$ in channels with widths of 100 μm (medium thick, black curve), 150 μm (thick, dark gray curve), 160 μm (thick, light gray curve), 170 μm (thick, black curve), 180 μm (dot-dashed black curve), 190 μm (thin, dashed black curve), 200 μm (solid, light gray curve), 250 μm (thin, medium gray curve), and 300 μm (thin, black curve).

a $0.6H_2 + 0.3O_2 + 0.1N_2$ mixture. The initial growth rate of the pressure pulse is clearly reduced below a channel width of 200 μm; however, due to the much stronger exponential second stage of the $w = 200$ μm case, the maximum pressure traces of $w = 200$ μm and $w = 250$ μm cases cross. As the channel width is reduced, the time of the transition between the two stages is delayed further still. In fact, in a $w = 100$ μm channel, the pressure of the flow builds to 3.5 atm only by $t = 518$ μm, which is within this second phase of exponential growth. This is 8.3 times longer than it takes the pressure pulse to build to this same pressure in the $w = 200$ μm case; moreover, this is still longer than the time for the much weaker exponential growth of the pressure pulse exhibited in the $w = 800$ μm channel.

The cusps in the $w = 250$ μm and $w = 300$ μm (indicated by the thin, black curve) channels pressure traces are due to the pressure pulse separating from the flame front and propagating forward towards the now stronger leading front. This stage slows the flame acceleration as the shock that has formed at the leading front grows in strength, as shown in Figure 5.9 for a $w = 250$ μm channel at (a) $t = 101$ μs, (b) $t = 106$ μs, (c) $t = 111$ μs, and (d) $t = 116$ μs.

In contrast to the behavior seen in the narrower channels, like that demonstrated in Figure 5.6 for the $w = 200$ μm case, the temperature profile forms a tulip like shape during the acceleration stage without a second shock formation, as seen in Figure 5.10. This is due to the adiabatic walls trapping the thermal energy, which is generated by converting the mechanical energy in the boundary layer. Here, the acoustic waves emanating from the flame front are attenuated only near the boundary. In contrast, in the narrower channels, the acoustic waves are more uniformly attenuated throughout the channel width before the exponential growth of the pressure pulse. This strong exponential growth leads to the creation of the second shock. Moreover, in the $w = 250$ μm case as the pressure pulse propagates from the flame front towards the leading shock front, the magnitude of the tulip shape the temperature field intensifies which is shown in the top halves of the channels in Figure 5.10 at (a) $t = 106$ μs and (b) $t = 116$ μs. Additionally, this is accompanied by the magnitude of the x-velocity increasing in front the flame front as well, which is shown in the bottom halves of the channels in Figure 5.10. It is probable that this stage is followed by a slower acceleration of the flame front while the pressure rebuilds, and eventually, a final acceleration to detonation.

Another indication that the dominant processes during the acceleration in narrower channels ($w \leq 200$ μm) is different from that of wider channels is exemplified by examining the pressure and the OH specie field in a $w = 100$ μm channel. In Figure 5.11 the pressure pulse at the flame front grows exponentially fast, as demonstrated by the flow fields at (a) $t = 520$ μs, (b) $t = 525$ μs, (c) $t = 530$ μs, and (d) $t = 535$ μs. This yields the second shock formation in front of the flame yet trailing well behind the weak initial pressure wave.

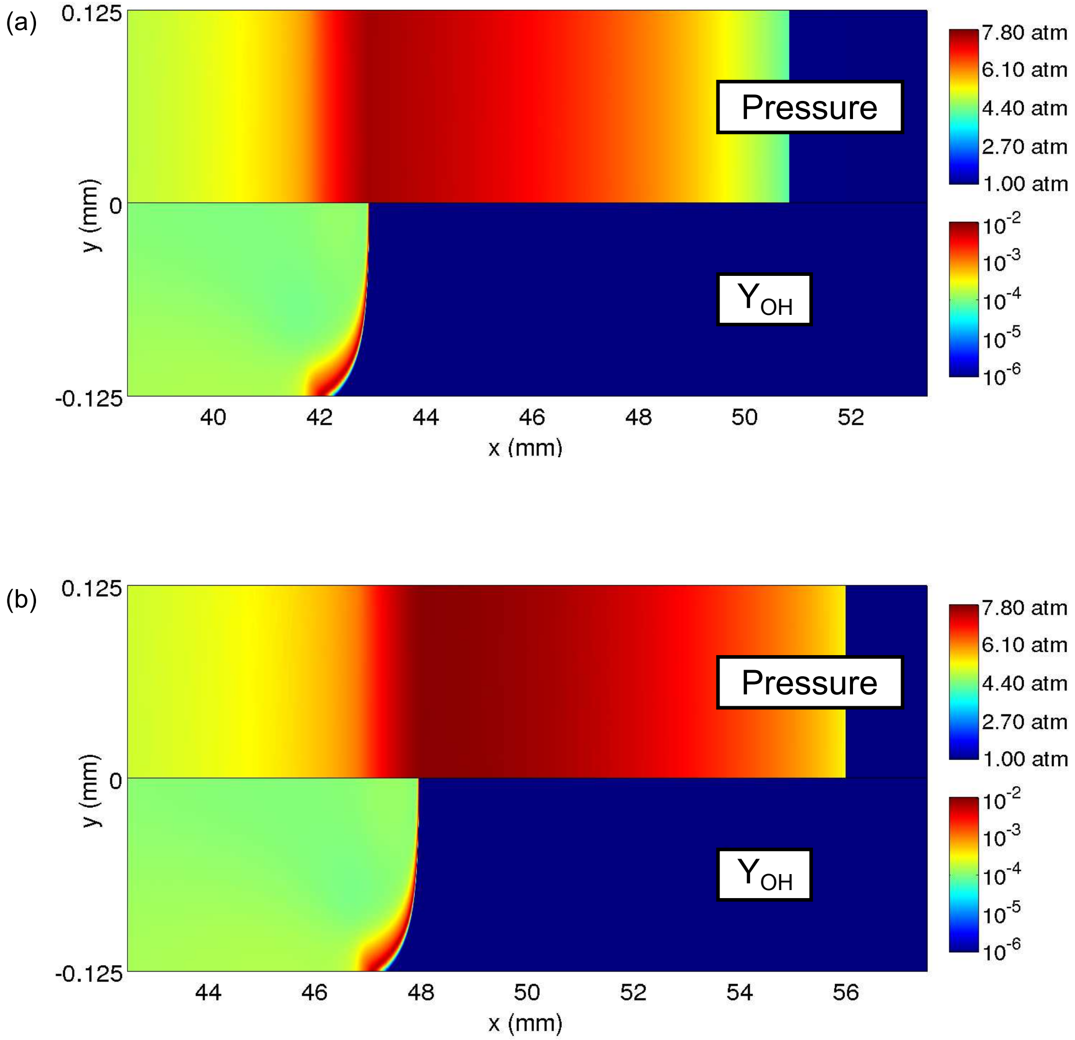

Figure 5.9. The pressure (upper half of channel) and Y_{OH} (lower half of channel) flow fields at (a) $t = 101$ μs, (b) $t = 106$ μs, (c) $t = 111$ μs, and (d) $t = 116$ μs for an initial mixture of $0.6H_2 + 0.3O_2 + 0.1N_2$ in a 250 μm wide channel (continued on page 111).

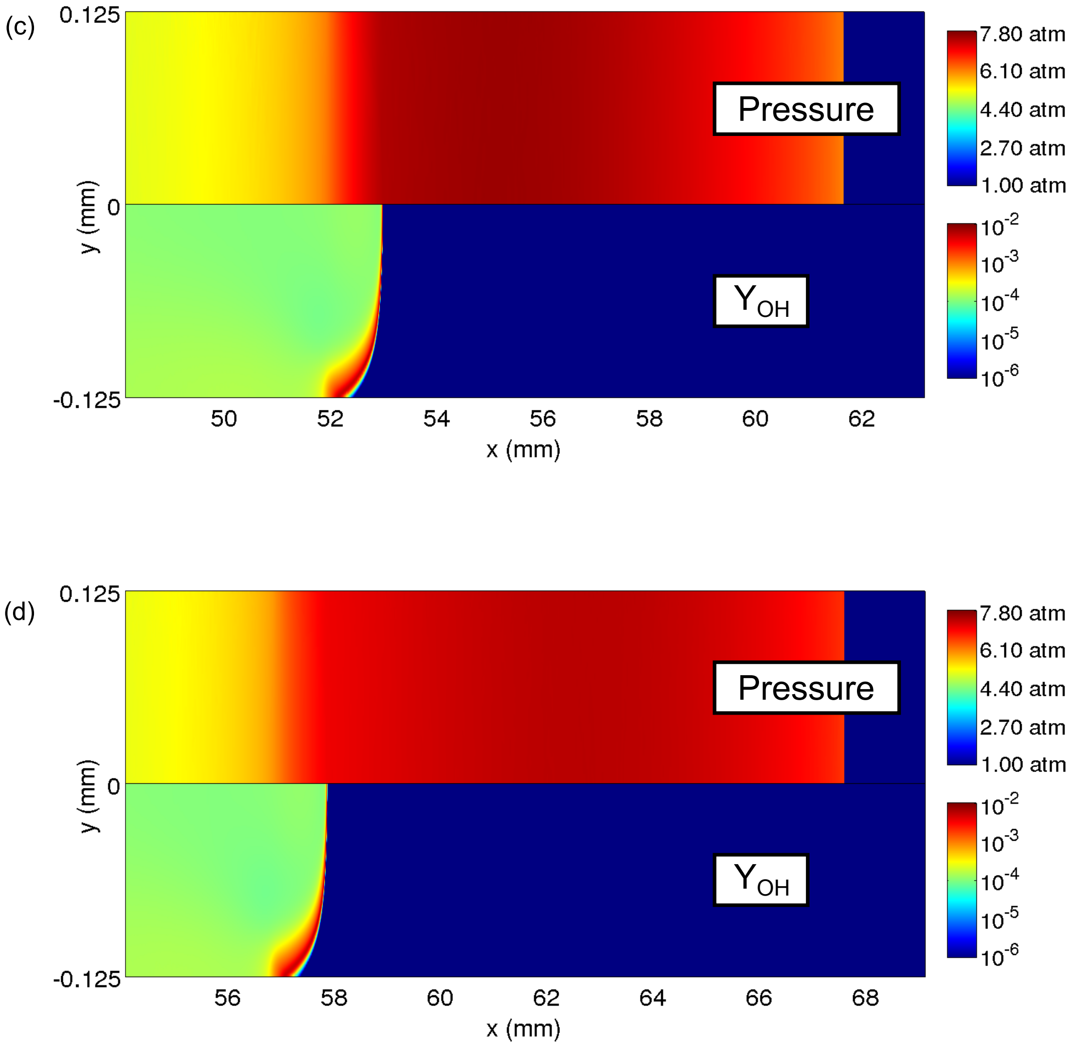

Figure 5.9. The pressure (upper half of channel) and Y_{OH} (lower half of channel) flow fields at (a) $t = 101$ μs, (b) $t = 106$ μs, (c) $t = 111$ μs, and (d) $t = 116$ μs for an initial mixture of $0.6H_2 + 0.3O_2 + 0.1N_2$ in a 250 μm wide channel (continued from page 110).

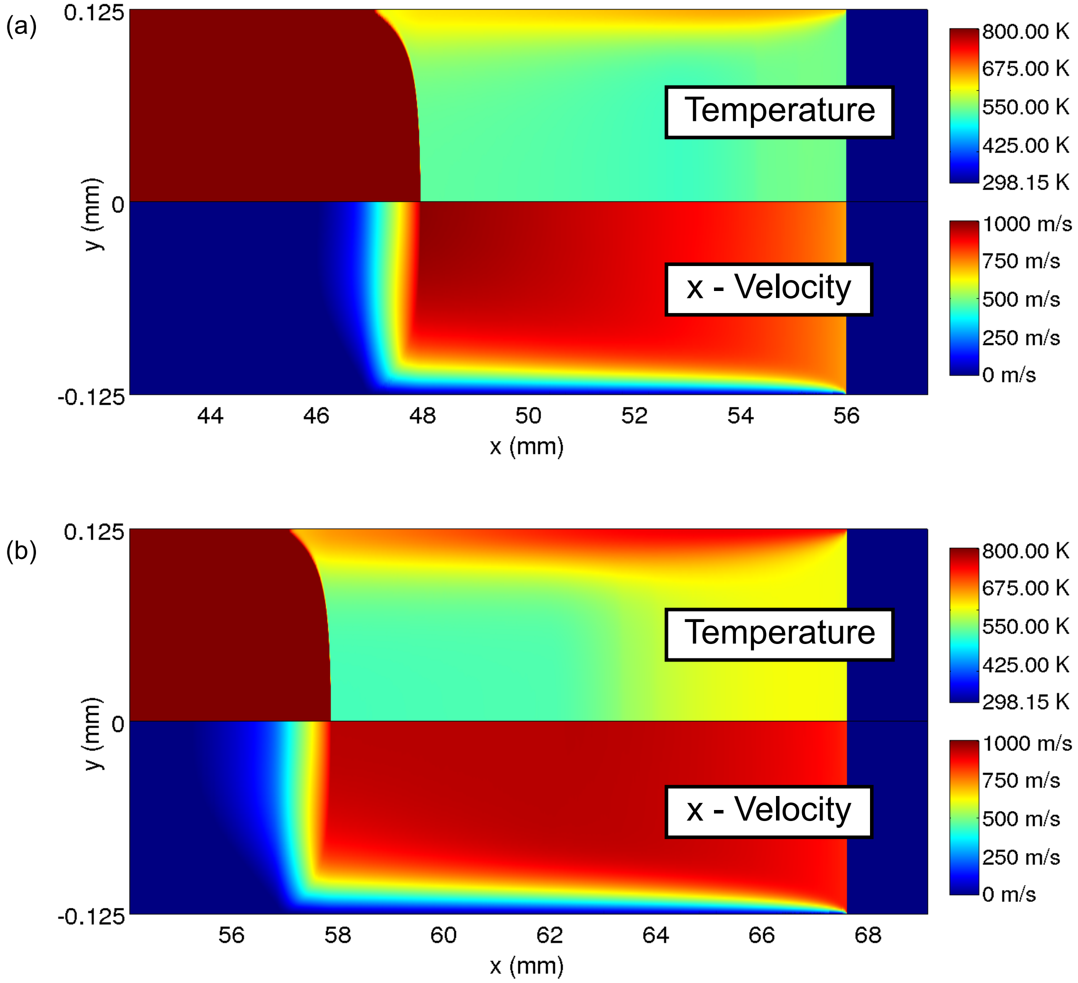

Figure 5.10. The temperature (upper half of channel) and x-velocity (lower half of channel) flow fields at (a) $t = 106$ μs and (b) $t = 116$ μs for an initial mixture of $0.6H_2 + 0.3O_2 + 0.1N_2$ in a 250 μm wide channel.

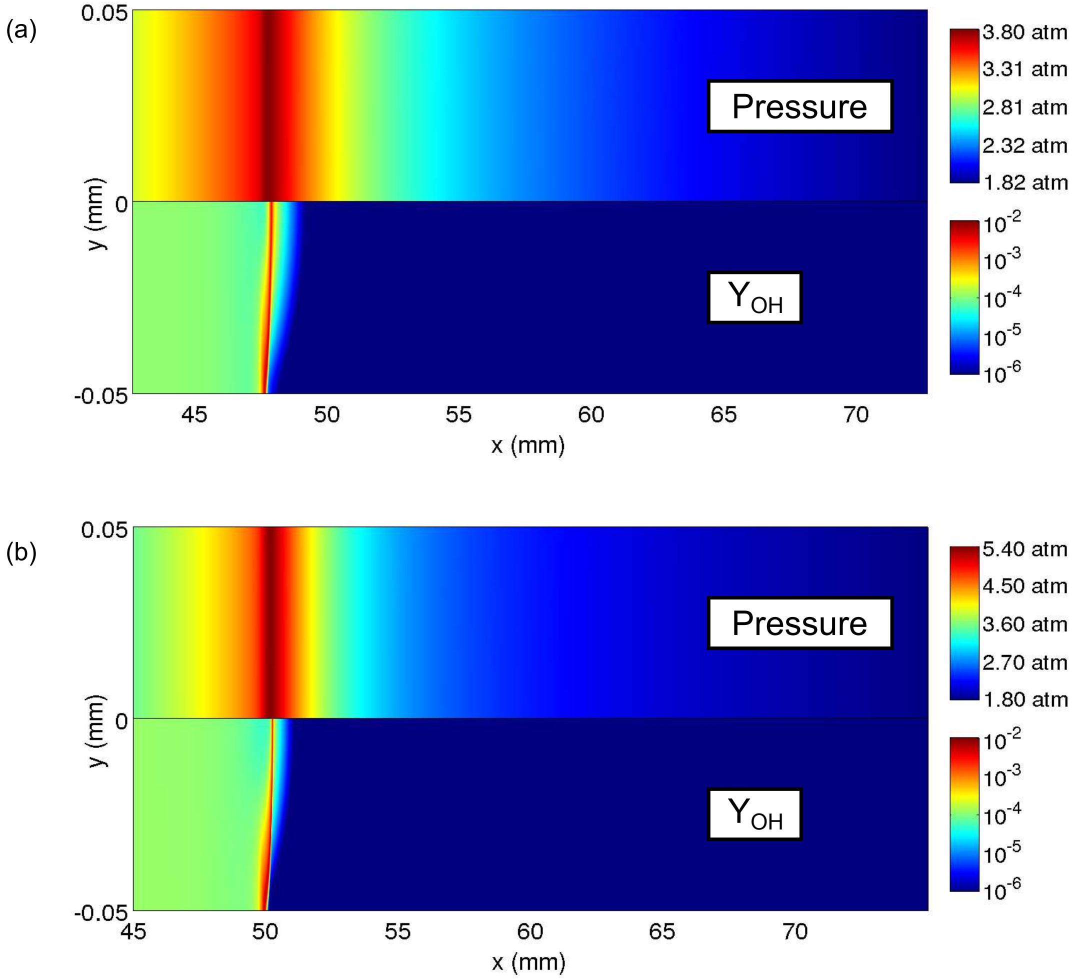

Figure 5.11. The pressure (upper half of channel) and Y_{OH} (lower half of channel) flow fields at (a) $t = 520$ μs, (b) $t = 525$ μs, (c) $t = 530$ μs, and (d) $t = 535$ μs for an initial mixture of $0.6H_2 + 0.3O_2 + 0.1N_2$ in a 100 μm wide channel (continued on page 114).

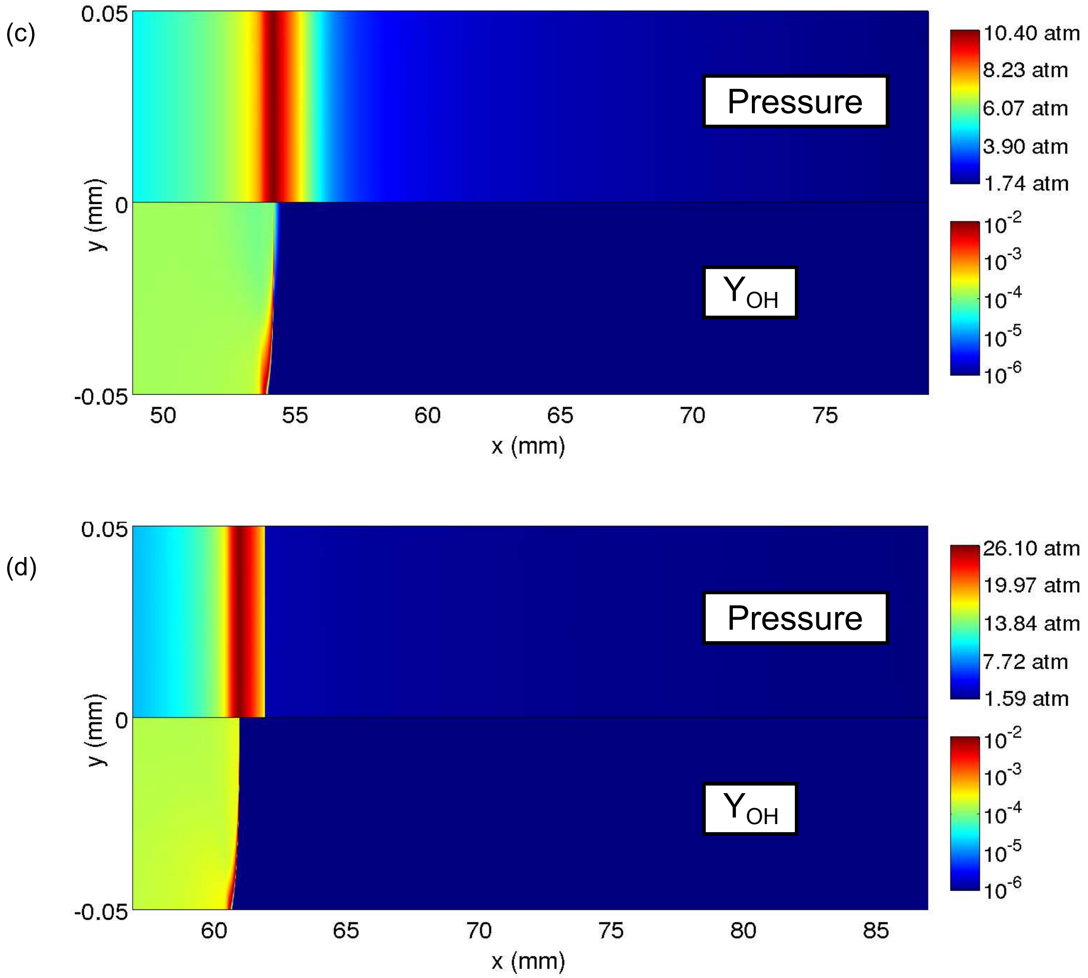

Figure 5.11. The pressure (upper half of channel) and Y_{OH} (lower half of channel) flow fields at (a) $t = 520$ μs, (b) $t = 525$ μs, (c) $t = 530$ μs, and (d) $t = 535$ μs for an initial mixture of $0.6H_2 + 0.3O_2 + 0.1N_2$ in a 100 μm wide channel (continued from page 113).

In the wider channels examined, the dominant process is one in which the mechanical energy of the weak leading pressure front and acoustic waves propagating forward from the flame front is converted to thermal energy due the no-slip walls which subsequently trap this energy inside the channel by their adiabatic nature. In the narrower channels this process is counter-acted by the capillary effect of viscosity which is eventually overcome and exponential pressure growth is realized. This transition can be seen more easily in Figure 5.12, which shows (a) the time for the pressure to build to pressures of $p = [1.25, 1.5, 1.75, 2.0, 2.5, 3.0, 4.0, 6.0, 8.0]$ atm and (b) the growth rates of the exponential pressure increase phase as well as the growth phase for the maximum flow velocity are shown versus inverse channel width. The transition between the two distinct propagation and acceleration regimes is clear in both the exponential growth rates of pressure (black curve with open squares) and the growth rates of the the Mach number, which is approximated by a line, of the flows (light gray curve with open circles), as seen Figure 5.12(b). Near the $w = 250$ μm case, there is shift from the power law rate at which the growth rates change. Additionally, there is a dramatic slowing of the rate of change of the growth rates.

By fitting the growth rate curves for both the exponential pressure growth (black, dashed line) and the buildup of the maximum flow velocity (light gray, dashed line) in the wider channels ($w \leq 250$ μm), an estimate can be obtained for how long it would take to reach the various levels in progressively wider channels. These estimates are shown in Table 5.1. The curve fits and estimates give insight into the effects of adiabatic no-slip wall in progressively wider channels. Based on these estimates, a true infinitely wide channel would take equally long to accelerate the flame towards detonation. This means that the adiabatic walls play a dramatic effect in determining the behavior of the flame, as without their presence the detonation would never form.

To test these estimates, both a $w = 1600$ μm channel and infinite channel test

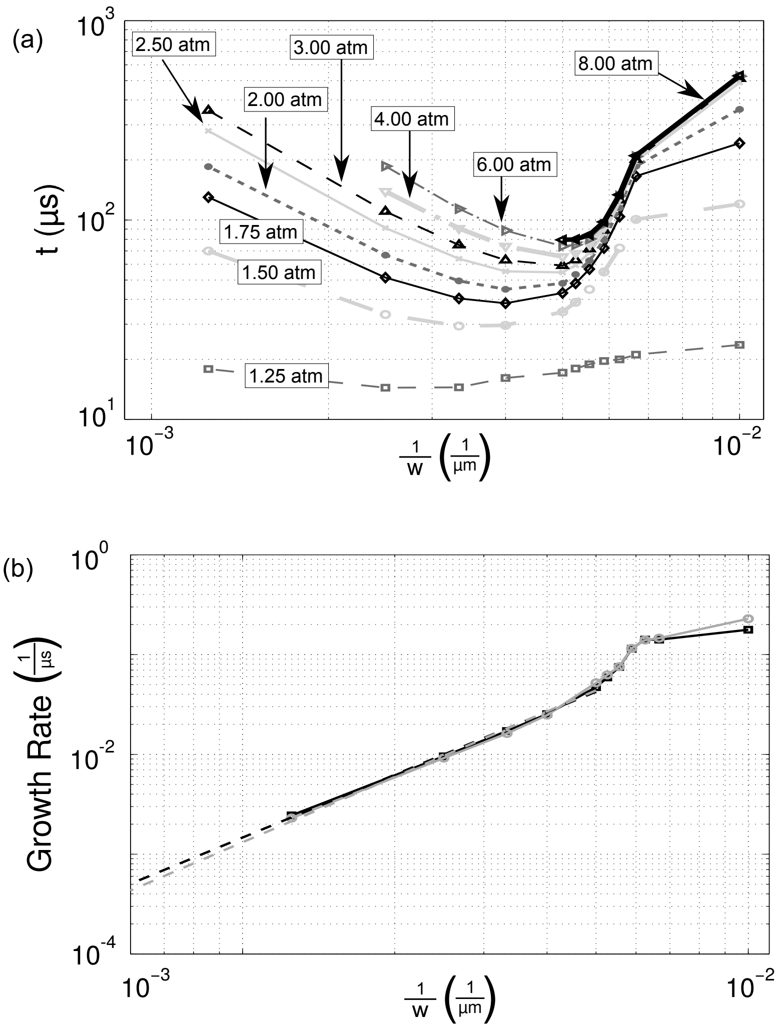

Figure 5.12. (a) The time it takes for the maximum pressure to build to 1.25 atm (dashed, thin, dark gray curve with open squares), 1.5 atm (dashed, light gray curve with open squares), 1.75 atm (thin, black line), 2.0 atm (dashed, dark gray curve with filled circles), 2.5 atm (light gray curve with X's), 3.0 atm (thin, dashed black curve with open up-facing triangles), 4.0 atm (thick, dot-dashed light gray curve with open downward triangles), 6.0 atm (thin, dot-dashed dark gray curve with right-facing open triangles), and 8.0 atm (thick black curve with open left-facing triangles) and (b) the exponential growth rate of the pressure pulse (black curve with open squares) and the growth rate of maximum Mach number (light gray curve with open circles) as well as the curve fit (dashed lines) versus inverse channel width for an initial mixture of $0.6H_2 + 0.3O_2 + 0.1N_2$.

TABLE 5.1

ESTIMATE OF THE BUILDUP TIME

Channel Width	p					$Ma = 1$
	1.25 atm	1.50 atm	1.75 atm	2.00 atm	4.00 atm	
1600 μm = 1.6 mm	31.4 μs	233 μs	404 μs	552 μs	1.32 ms	1.14 ms
3200 μm = 3.2 mm	214 μs	1.08 ms	1.82 ms	2.45 ms	5.75 ms	5.08 ms
10^4 μm = 10 mm= 1 cm	2.02 ms	9.49 ms	15.8 ms	21.3 ms	49.7 ms	48.9 ms
10^5 μm = 10 cm	168 ms	744 ms	1.23 s	1.65 s	3.84 s	4.54 s
10^6 μm = 100 cm= 1 m	14.1 s	58.5 s	96.1 s	129 s	298 s	420 s

cases were examined. In order to reduce the computational cost, the $w = 1600$ μm case was run only to 350 μs. An approximation for an infinite channel was obtained by performing a one-dimensional study. As the estimated time for the pressure to build in the $w = 1$ m estimate is excessively long and the fact that the simulation time for the $w = 1600$ μm case was truncated at 350 μs, the infinitely wide case was only simulated until 450 μs. The maximum pressure traces for the $w = 800$ μm (indicated by black curve), $w = 1600$ μm (indicated by dark gray curve), and infinite (indicated by light gray curve) cases are shown in Figure 5.13. The estimates are indicated by filled circles if they occur within the simulation time. The pressure pulse produced by the energy deposition function are nearly identical except for the increases due to reflections from the walls. By extrapolating using the growth rate from the infinite case, the time to get to even 2 atm is 2.1 s which is on the similar order of the estimate for the 10 cm case's estimate. This again indicates the importance of the adiabatic wall in accelerating the flame towards a detonation. However, due to the small amount growth, it difficult to get an accurate growth rate for this infinite case. Similarly, for the $w = 1600$ μm channel case the estimate for the pressure to build to

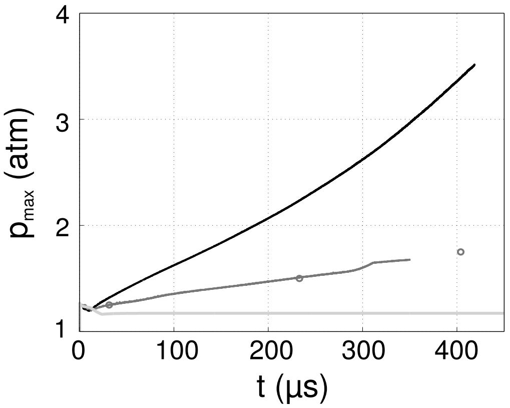

Figure 5.13. The maximum pressure versus time for an initial mixture of $0.6H_2 + 0.3O_2 + 0.1N_2$ in channels with widths of 800 μm (black curve) and 1600 μm (dark gray curve) and infinitely wide channel (light gray curve).

1.75 atm is 404 μs, and the simulation yields an estimate based on the growth rate of $t = 396$ μs. Moreover, both estimates shown in Table 5.1 for $1.25,\ 1.5$ atm agree well with the simulation times of $\sim 32.5,\ 2.25 \times 10^2$ μs, respectively.

Figure 5.14 shows comparison of the pressure along the centerline of the widest two channels studied, $w = 800$ μm (indicated by thin black curves) and $w = 1600$ μm (indicated by thick dark gray curves) to that of the infinite channel (indicated by thick light gray curves) at (a) $t = 5$ μs, (b) $t = 25$ μs, (c) $t = 50$ μs, (d) $t = 150$ μs, (e) $t = 250$ μs, and (f) $t = 350$ μs. Initially, the front pulse decays and nearly becomes separated from the trailing flame as seen in Figure 5.14(a). The oscillations present in the two two-dimensional cases are absent from the infinitely wide case as there are no reflections of the pressure pulse from side walls. The location of the flame front, which is indicated by a flat zone at the left part of the domain remains at the similar pressures and locations for all three cases up $t \sim 5$ μs. Later in time, Figure 5.14(b) and (c), the oscillations present indicate acoustic waves propagating forward towards the front pressure pulse; additionally, there begins to be a separation between the three different cases with the flame's pressure pulse becoming apparent in the 800 μm wide channel. By $t = 150$ μs, nearly all of the oscillations are negligible with the front pulse being connected directly to the flame's ever growing pressure pulse. After this point, the fact the pressure pulse grows faster in $w = 800$ μm and $w = 1600$ μm than in infinite channel case becomes even more apparent. Moreover, the flame fronts which are clearly discernible in both cases begin to separate further in both magnitude and location indicating a significant difference in flame speed and accelerations. However, the front pressure wave propagates at nearly the same rate for the first 350 μs; as it propagates at nearly the ambient speed of sound. At this last point, the front pressure pulse in the 800 μm wide case is finally being driven at a slightly higher rate than the other cases. Additionally, the pressure wave is beginning to separate from the flame front in the 1600 μm wide channel case, representing the slight anomaly in the pressure trace from Figure 5.13.

5.3.2 Effect of the Varying Amount of Diluent

Next, a study was performed in which the percentage of nitrogen (diluent) was varied with the goal of determining how the addition of diluent alters the rate of growth of the pressure pulse. As one would expect by increasing the percent of diluent, the rate of growth of the pressure pulse at the flame front is decreased; additionally, the flame acceleration is also slower. This is demonstrated in Figure 5.15, which shows (a) the maximum pressure and (b) the maximum Mach number of the flow versus time in a $w = 800$ μm channel for mixtures with a molar ratio of $H_2 : O_2$ of $2 : 1$ and consist of a molar percentage of $[1\%, 10\%, 25\%, 40\%, 55.6\%]$ N_2. The exponential growth rate of the pressure pulse at the flame front at this channel width decreases from 2.78×10^{-3} $1/\mu$s for the nearly pure hydrogen-oxygen mixture to 4.85×10^{-4} $1/\mu$s for the hydrogen-air mixture. This causes the time to reach a pressure of only 3.5 atm to change from 345.2 μs to an estimate of greater than 2515 μs (an estimate based on extrapolation of the rate for the hydrogen-air mixture).

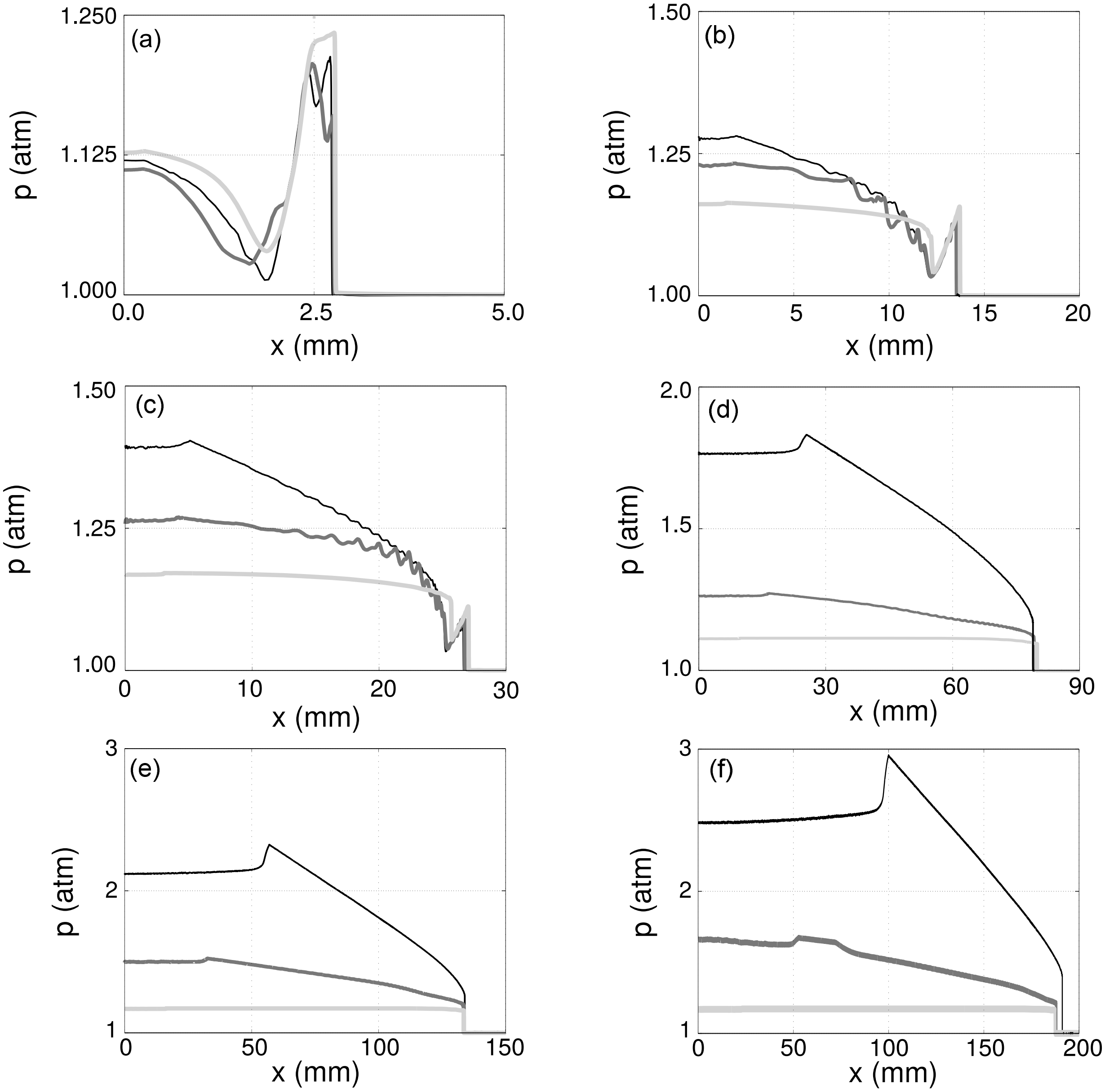

Figure 5.14. The pressure field along the center line for channel widths of 800 μm (thin black curves) and 1600 μm (thick dark gray curves) and the infinitely wide channel (thick light gray curves) at (a) $t = 5$ μs, (b) $t = 25$ μs, (c) $t = 50$ μs, (d) $t = 150$ μs, (e) $t = 250$ μs, and (f) $t = 350$ μs for an initial mixture of $0.6H_2 + 0.3O_2 + 0.1N_2$.

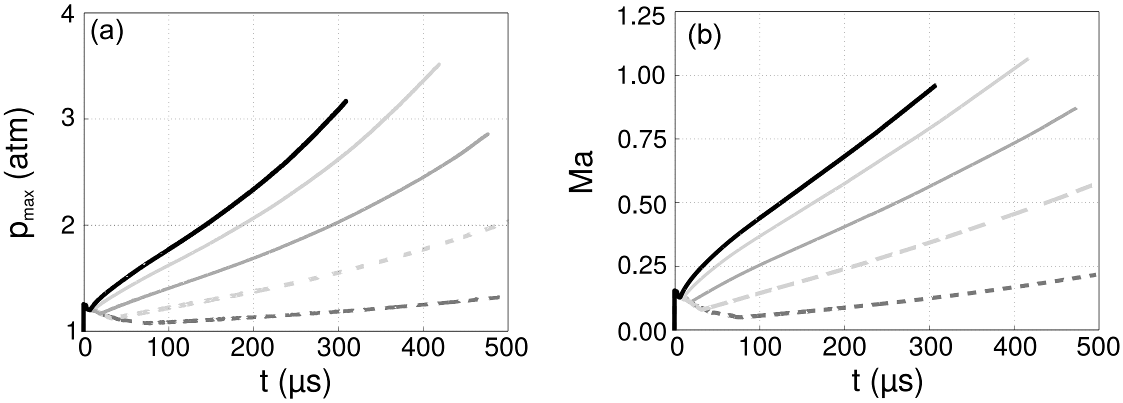

Figure 5.15. (a) The maximum pressure and (b) the maximum Mach number in a 800 μm wide channel versus time for initial mixtures with a hydrogen-oxygen ratio of $2:1$ and 1% (solid, black curve), 10% (solid, light gray curve), 25% (solid, dark gray curve), 40% (dashed, light gray curve), and 55.6% (dashed, dark gray curve) of N_2.

Similarly, the time it takes for the flow to become supersonic ($Ma = 1$) changes from 309.4 μs to more than 2451 μs (an estimate based on extrapolation of the rate for the hydrogen-air mixture).

The cause of this delay in the buildup of pressure or the reduction in the rate the flame accelerates towards detonation is most probably dependent on two factors. The first is the reduction in overall energy released from reaction due to adding a larger percentage of non-reacting species N_2, and thus, reducing the overall moles of $2H_2 + O_2$ in the initial mixture. The second is due to the decrease in the unreacted thermal conductivity and the slight increase in unreacted viscosity. The small increase in viscosity helps slow the flow and coincidently converts a minor amount more of mechanical energy to thermal energy along the wall boundaries. However, the thermal conductivity decreases by nearly half between the pure hydrogen-oxygen mixture and the hydrogen-air mixture. Thus, the fluid behind the weak initial pressure pulse does a less efficient job of using this thermal energy along the no-slip walls as the feedback loop between pressure, temperature, and reaction rate is weakened.

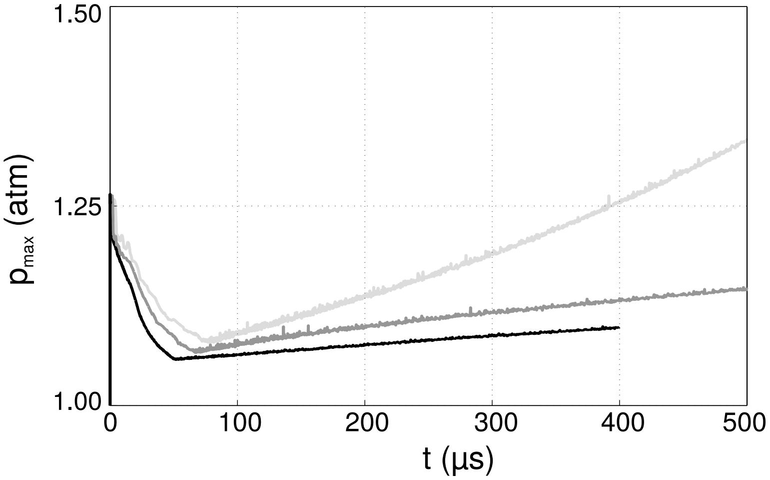

Figure 5.16. The maximum pressure versus time for an initial mixture of $0.296H_2 + 0.148O_2 + 0.556N_2$ in channels with widths of 200 μm (black curve), 400 μm (dark gray curve), and 800 μm (light gray curve).

In addition to reducing the growth rate of the flame front's pressure pulse, increasing the percentage of diluent can also shift the width at which the viscous resistance due to the capillary effects becomes dominant. Recall that for the $0.6H_2 + 0.3O_2 + 0.1N_2$ mixture, this crossover point was shown to be at a channel width of approximately 250 μm. For a mixture of hydrogen-air ($0.296H_2 + 0.148O_2 + 0.556N_2$), this crossover point occurs above the channel width of 400 μm. This can be deduced from Figure 5.16, which shows pressure traces for a hydrogen-air mixture at $w = [200, 400, 800]$ μm. Unless the capillary effects have become dominant, as the channel width is reduced, the early growth rate of the pressure pulse increases. Thus, as the early growth rate of the pressure pulse is smaller in the $w = 400$ μm channel (indicated by dark gray curve) than that of the $w = 800$ μm channel (indicated by light gray curve), it can be implied that the crossover point must be at a channel with greater than 400 μm. It is conjectured that the crossover point is in fact between 400 μm and 800 μm, but in order to verify this, a larger channel would need to be simulated.

5.3.3 Adiabatic versus Isothermal No-Slip Walls

It is clear that adiabatic walls trap thermal energy in the system allowing the flame to accelerate and the pressure pulse to grow at a faster rate as the channel width is decreased until the viscous resistance of very narrow capillary channels becomes the dominant process. However, in these thin channels the heat losses could play a dramatic role in the flame propagation and acceleration. The use of an isothermal wall at the ambient temperature gives an upper bound on the heat losses to the environment during the flame acceleration to detonation. Additionally, an isothermal wall introduces a thermal boundary layer into the flow; this boundary layer transitions from the hot reacted gases to the ambient temperature. Due to the formation of this fine thermal boundary layer the necessary spatial resolution of $\mathcal{O}(5 \times 10^{-8}$ m) during the flame propagation stage which results in a time step of $\mathcal{O}(1 \times 10^{-11}$ s); similarly, the total number of points also increases to $\mathcal{O}(5 \times 10^{5})$. Therefore, an investigation of the early time (≤ 25 μs) behavior was performed for a initial mixture of $0.6H_2 + 0.3O_2 + 0.1N_2$ for channel widths of 100 μm, 200 μm, 400 μm, and 800 μm.

Figure 5.17 shows the pressure traces over the first 25 μs for (a) the 100 μm wide channel, (b) the 200 μm wide channel, (c) the 400 μm wide channel, and (d) the 800 μm wide channel for both adiabatic (indicated by black curves) and isothermal (indicated by dashed gray curves) walls. In the two narrowest cases which are both below the crossover point, the introduction of the isothermal walls dramatically changes the behavior, causing an extinction of the flame. Moreover, in the two wider cases examined, there is a delay in the time at which the maximum pressure shifts from the initial front to the flame front.

The temperature contours, shown in Figure 5.18 for an initial mixture of $0.6H_2 + 0.3O_2 + 0.1N_2$ in a 800 μm wide channel for adiabatic (top half of channel) and isothermal (bottom half of channel) wall conditions, suggest that in addition to this delay there is also an initial slowing of the flame and ever so slight slowing of the

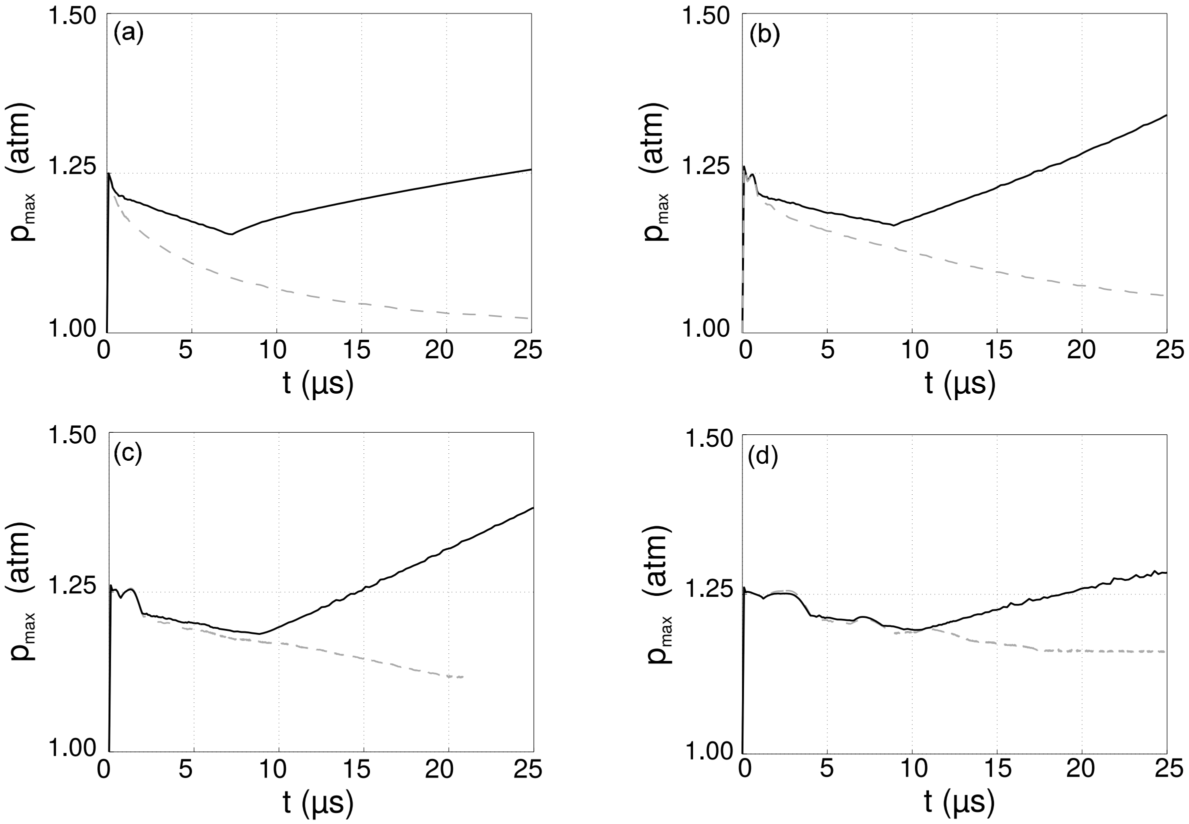

Figure 5.17. The maximum pressure versus time for an initial mixture of $0.6H_2 + 0.3O_2 + 0.1N_2$ in channels with widths of (a) 100 μm, (b) 200 μm, (c) 400 μm, and (d) 800 μm for adiabatic (black curve) and isothermal (dashed gray curve) wall conditions.

front pressure pulse. At $t = 5$ μs, which is shown in Figure 5.18(a), the initial flame profile (indicated by the edge of the red feature) is altered near the wall boundary. The adiabatic case has a flatter edge cross the full domain; whereas; in the isothermal case there is a strong curvature of the flame near the boundary. Figure 5.18(b) shows the difference in the flame propagation in the temperature profiles at $t = 15$ μs. The flame front is retarded in the isothermal case from the equivalent front location in the adiabatic case. By $t = 25$ μs, the isothermal flame front as well as the front pressure pulse location are both discernibly hindered by the presence of the isothermal walls, as shown in Figure 5.18(c). However, it is difficult to distinguish the thermal boundary layer at this point. To more clearly visualize the boundary layer, a zoomed in profile at $t = 25$ μs is shown in Figure 5.18(d). Now, even though the thermal boundary layer is thin, the isothermal walls have macroscale effects on flame position and front pressure pulse location at early times. The later effect of isothermal walls on the propagation and acceleration at this channel remains unquantified at this time; however, the present study suggests that longer time behavior should continued to be examined to understand how dramatic the effect these isothermal walls have on the overall acceleration of the flame.

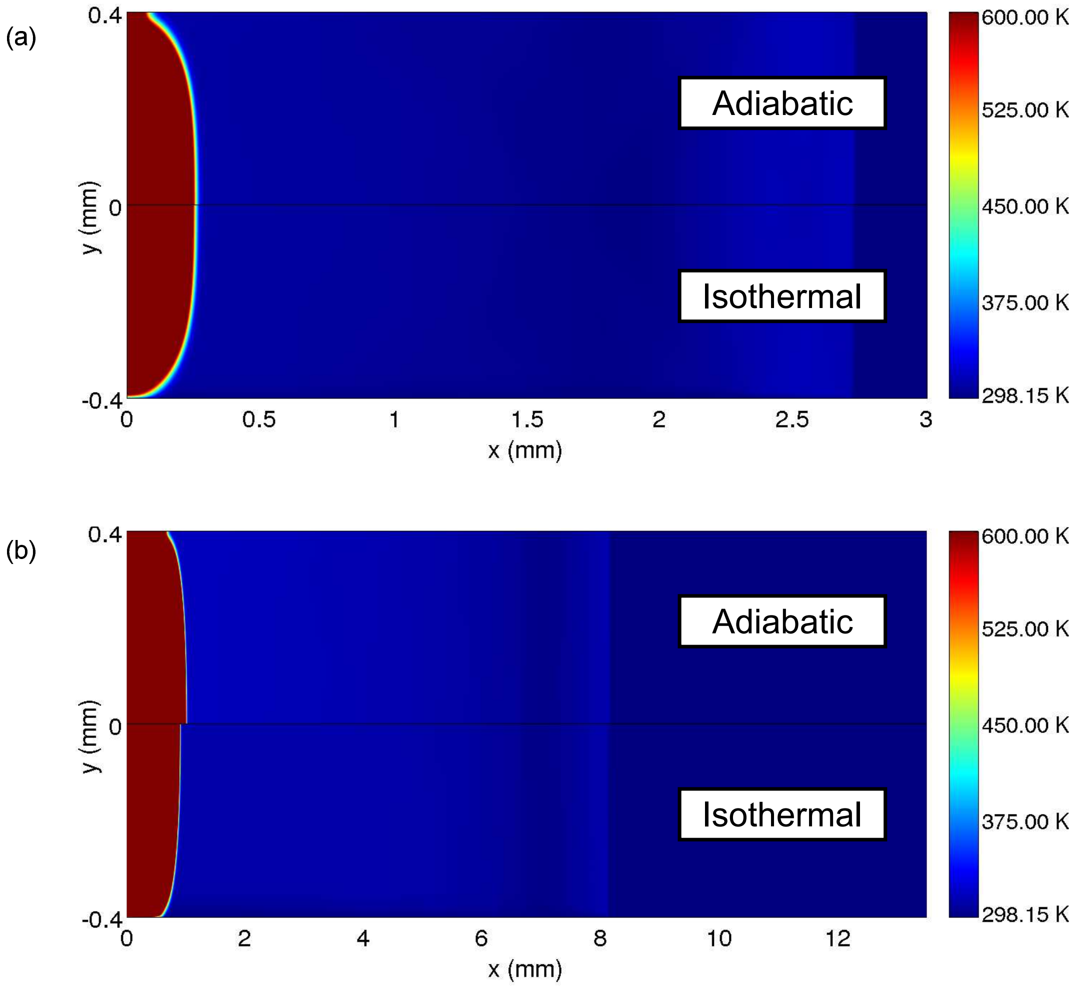

Figure 5.18. The temperature flow field for adiabatic (upper half of channel) and isothermal (lower half of channel) wall conditions at (a) $t = 5$ μs, (b) $t = 15$ μs, and (c) $t = 25$ μs and (d) a zoomed in profile at $t = 25$ μs near the isothermal boundary for an initial mixture of $0.6H_2 + 0.3O_2 + 0.1N_2$ in a 800 μm wide channel (continued on page 127).

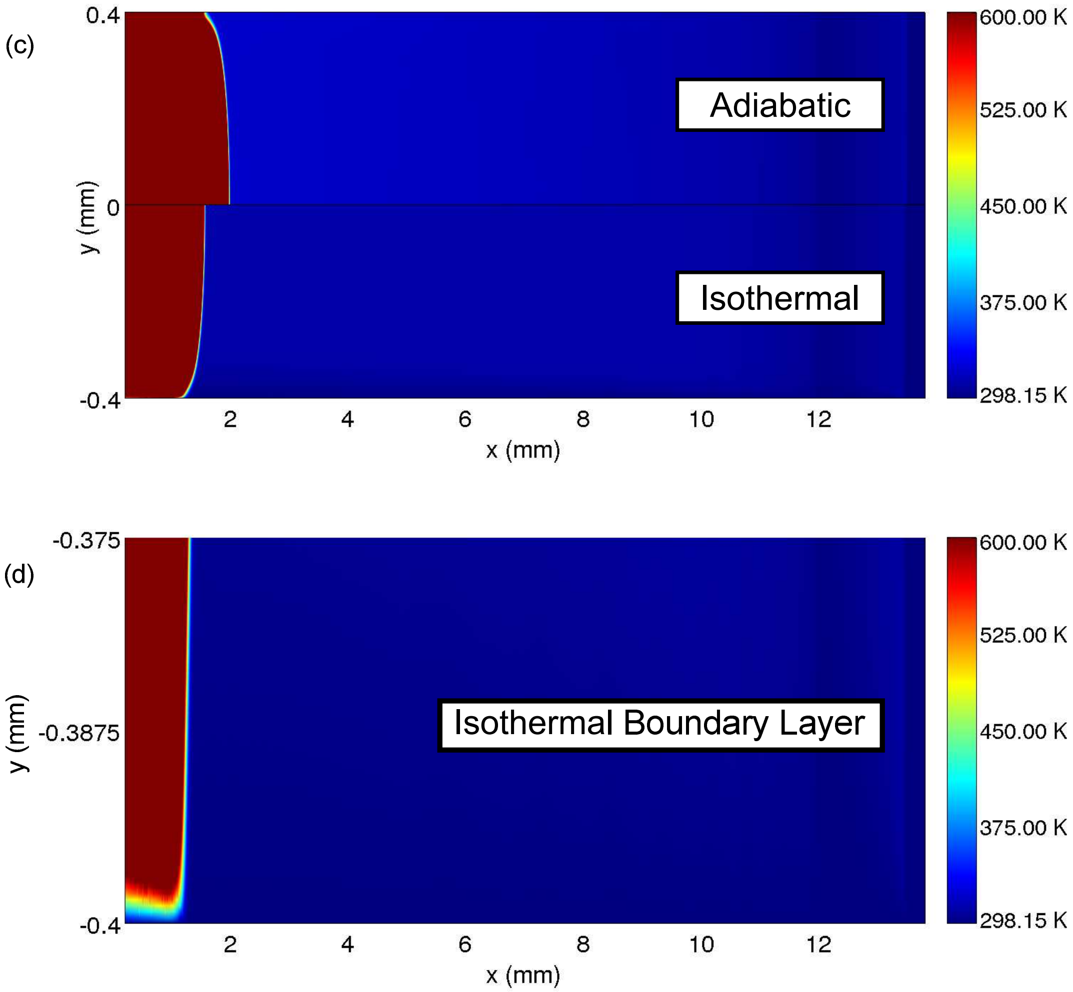

The temperature flow field for adiabatic (upper half of channel) and isothermal (lower half of channel) wall conditions at (a) $t = 5$ μs, (b) $t = 15$ μs, and (c) $t = 25$ μs and (d) a zoomed in profile at $t = 25$ μs near the isothermal boundary for an initial mixture of $0.6H_2 + 0.3O_2 + 0.1N_2$ in a 800 μm wide channel (continued from page 126).

CHAPTER 6

DISCUSSION AND FUTURE WORK

The current work has quantified the effects of diffusive processes on propagating gaseous detonations as well as flame propagation and acceleration towards detonation in narrow channel flow by resolving all of the relevant scales. The models presented built upon previous work done in the inviscid limit. Much of the work in detonation dynamics has neglected diffusive processes; however, the finest reaction length scales occur on scales similar to those on which diffusion acts.

First, a simplified one step kinetics model in one-dimension was examined with the inclusion of only constant diffusive coefficients. The temporal and harmonic analysis of this model suggests that the dynamics of one-dimensional pulsating detonations can be dramatically altered by the introduction of mass, momentum, and energy diffusion. The introduction of diffusion delays the onset of instability and enlarges the activation energy range of the bifurcation process that leads to chaotic detonation in comparison with the inviscid analog. However, the qualitative behavior of the one step model remains unchanged going through period-doubling bifurcations and a transition to what is most likely chaotic behavior. It was necessary to use a fine resolution to capture the dynamics accurately. Employing coarse spatial resolution results in seemingly plausible but dramatically different predicted dynamics in some cases, suggesting that the use of filtering or sub-grid models maybe problematic. Moreover, for this model an *a priori* estimate has been made of the necessary resolution to properly capture the dynamics based on the activation energy of the reaction. This model, however, lacked some more physically based properties such as multi-component mass diffusion, temperature and mixture-dependent viscosity and thermal conductivity, multiple reaction length scales and lastly, a heat release on a longer scale.

The second model examined a series of piston-driven detonations utilizing a hydrogen-oxygen-nitrogen detailed kinetics model and extended the previous model by including multi-component diffusion, as well as mixture and temperature dependent fluid properties. Several distinct phases in behavior were predicted using the WAMR method to fully resolve the necessary scales: stable propagation, high-frequency pulsating propagation, dual-mode (high and low frequencies) pulsating propagation, low-frequency pulsating propagation, and period-2 low frequency pulsation. As the scales on which diffusion and the main heat release driving the detonation are more disparate than the previous case, the mass, momentum, and energy diffusion has a much smaller effect. In fact, it delays the onset of instability by less than 2% in the piston velocity; however, near the stability limit there is a significant reduction oscillation amplitude. The lower the piston velocity, the more unstable the hydrogen-air detonation becomes and the weaker effect of viscosity has on the propagation behavior. Moreover, the fine resolutions used to predict the detonation dynamics enabled detailed results to be obtained from harmonic analysis. The harmonic analysis revealed that the fundamental frequency of the pulsations as well as the rest of the spectrum shifts within the different propagation phases. It was demonstrated that the energy deposited into the system by the supporting piston effectively changes the percentage that the various modes of energy carry.

Lastly, a series of channel flows consisting of hydrogen-oxygen-nitrogen mixtures were examined using the WAMR method to fully resolve the necessary scales while reducing the computational cost required. Inside an adiabatic channel, there are two distinct types of propagation and acceleration of flames. In the narrowest channels the flow is dominated by capillary effects due to viscosity and diffusion; this yielded a long slow growth in the magnitude of the pressure pulse at the flame front followed by a fast exponential growth of the pressure and the formation of a strong shock near the flame front but behind the initial pressure wave front. In wider channels ($w \geq 250\ \mu$m) the pressure pulse at the flame front grew exponentially, accelerating the bulk flow downstream of the flame by sending acoustic waves forward. These acoustic waves coalesce at the initially weak pressure wave front causing it to grow in strength and eventually becoming a stronger shock. In these wider channels, the mechanical energy from the acoustic waves was converted to thermal energy in the boundary layer, but the bulk of the flow remained weakly affected. In contrast, more of the bulk flow is attenuated by the boundary layer in the narrow channels. Moreover, the results from the infinitely wide case indicate that without viscous effects at the boundaries the acceleration towards detonation would take a near infinite amount of time. Increasing the percent of diluent present in the mixture slowed the growth rate of the pressure at the flame front and hence delayed the acceleration of the flame. Additionally, it also shifts the point at which the viscous resistance becomes dominant. When isothermal walls were considered, the two cases within the capillary dominated flow regime had flame extinction. In the wider cases examined there is a significant delay in the time at which the pressure pulse at the flame front overtakes the initial pressure pulse in magnitude. Additionally, there is no appreciable growth to the pressure at the flame front after it overtakes the initial pressure pulse in magnitude. Moreover, there is a discernible slowing of the flame propagation speed and that of the front pressure wave at early times due to the thermal energy lost through the boundary.

Neglecting diffusive processes helps reduce the necessary resolution to fully capture the relevant scales in detonation modeling. However, by introducing physical diffusive processes, a meaningful cutoff scale is introduced. Without such a physically relevant scale, another cutoff scale is usually introduced, as in the various sub-grid models, *e.g* Large-Eddy-Simulation or turbulent mixing models. This may be problematic, as believable but inaccurate results can be predicted. Moreover, there are regimes in which viscous effects are important, *e.g.* near stability boundaries or in channels where the walls accelerate the flame towards detonation. Furthermore, by resolving these diffusive scales, detailed results can be given in the spatial, temporal, and frequency domains without the loss of filtering the active high frequency modes or fine structures.

This work suggests several extensions for possible future work. A simple extension would be to continue the simulations with the ambient temperature isothermal walls to verify that the retardation from the early times continues at later times. Additionally, examining more channel widths would yield a better estimate of when the effects of the isothermal walls are important during the development and propagation of the flame. Likewise, the less reactive cases such as hydrogen-air could be simulated further in time until it reaches a sonic flow.

Another straightforward extension would be to examine the difference between the flame acceleration in a channel versus in a tube. Symmetrical cylindrical flow can be mathematically modeled in a similar manner to that of channel flow with source terms added to the momenta and energy equations. Another complementary study would be the investigation of flame formation, propagation, and acceleration in a non-premixed mixture.

Moreover, the inclusion of more complex constitutive relations for the diffusive processes may provide further insight, including some non-equilbrium effects. These non-equilbrium effects may be important particularly in or near the shock especially for dense polyatomic gases. This also likely suggests that a more complicated mixing rule be used, as the polyatomic gases would no longer be treated as ideal gases.

If an implicit integration technique could be implemented in combination with the WAMR method, a reduction in the number of computational time steps necessary to simulate a flow in a channel could be realized. Therefore, a fully detonating flow with realistic diffusion parameters could be simulated. However, care must be taken to ensure that a small enough time step is still used to capture the high frequency oscillations present in the flow as the implicit time step could act as a low-pass filter when compared to an explicit time step which is chosen based on the resolution employed. Moreover, a more complex chemical mechanism and fuel could be examined if less computational steps were necessary to calculate a solution. Correspondingly, a true three-dimensional channel/tube flame acceleration could be pursued as well. In addition, this could also be used to evaluate the how the detonation cell size is effected by the no-slip walls in various channel widths. As briefly mentioned in Section 5.2.2, as the flame accelerates towards detonation, the computational expense dramatically increases with the current computational method implemented. This is due to the reduction in the size of the time step and the increase in the necessary resolution (thus an increase in the number of points) which are correlated with each other in the explicit integration scheme currently used. This increase in computational cost nearly precludes a study of cellular structures in multi-dimensional detonations when resolving all relevant reactive, advective, and diffusive spatial scales with the implemented computational method without a very substantial amount of computational resources.

The results here indicate that viscous effects can be important in certain regimes, *e.g.* near stability boundaries or near walls where the boundary layer is on a similar order to that of the finest reaction length scales. However, it remains intractable with current computational resources to fully resolve all the finest scales while performing an engineering sized calculation in a timely fashion. Thus, the development of models, such as those developed by Fiorina and Lele [34], that manifest these smaller scales onto larger ones that can be captured in engineering calculations will continue. These models should include a smooth transition to meaningful physical cutoff scale introduced by diffusion when all the physical scales are resolved. Meaning that as the smallest utilized shrinks near a large gradient in the flow, the contribution due to the artificial part reduces towards zero. Likewise, in areas of the flow that need less refinement and have smaller gradients, the contribution is also small [34]. This allows a single unified model to examined and compared to experiments over a variety of physical conditions. Furthermore, this would give rise to further examinations pushing the limits of the range of scales that can be resolved in an engineering calculation.

APPENDIX A

MULTICOMPONENT GASEOUS PHASE SPECIES TRANSPORT PROPERTIES

As mentioned in Section 2.2, the multicomponent diffusion coefficients, D_{ik}, the thermal diffusion coefficients, D_i^T, and the isotropic mixture thermal conductivity, k, for a mixture of N species are obtained by solving the linear $\mathsf{L}-$matrix system [23]. The $\mathsf{L}-$matrix system is given by

$$\begin{bmatrix} \mathsf{L}^{00,00} & \mathsf{L}^{00,10} & \mathsf{L}^{00,01} \\ \mathsf{L}^{10,00} & \mathsf{L}^{10,10} & \mathsf{L}^{10,01} \\ \mathsf{L}^{01,00} & \mathsf{L}^{01,10} & \mathsf{L}^{01,01} \end{bmatrix} \cdot \begin{bmatrix} \mathbf{c}_{00} \\ \mathbf{c}_{10} \\ \mathbf{c}_{01} \end{bmatrix} = \begin{bmatrix} \mathbf{0} \\ \mathbf{y} \\ \mathbf{y} \end{bmatrix}, \tag{A.1}$$

where the nine block sub–matrices $\mathsf{L}^{\mathsf{U},\mathsf{U}}$, $\{\mathsf{U},\mathsf{V}\} = 00,\ 10,\ 01$ are constant $N \times N$ matrices, $\mathbf{c}_{\mathsf{U}}$, $\{\mathsf{U}\} = 00,\ 10,\ 01$ the $N-$sized solution vectors to the $\mathsf{L}-$matrix system, and $\mathbf{y}$ the mole fraction vector. The components of each block sub–matrix are defined by Dixon-Lewis [23] as

$$\mathsf{L}_{ij}^{00,00} = \frac{16\ T}{25\ p} \sum_{k=1}^{N} \frac{y_k}{\overline{M}_i\ \mathcal{D}_{ik}} \left(\overline{M}_j\ y_j\,(1 - \delta_{ik}) - \overline{M}_i\ y_j\,(\delta_{ij} - \delta_{jk})\right), \tag{A.2}$$

$$\mathsf{L}_{ij}^{00,10} = \frac{8\ T}{5\ p} \sum_{k=1}^{N} y_j\ y_k\,(\delta_{ij} - \delta_{ik})\ \frac{\overline{M}_k\,(1.2\ \mathcal{C}_{jk} - 1)}{\left(\overline{M}_j + \overline{M}_k\right)\ \mathcal{D}_{jk}}, \tag{A.3}$$

$$\mathsf{L}_{ij}^{00,01} = 0, \tag{A.4}$$

$$\mathsf{L}_{ij}^{10,00} = L_{ji}^{00,10}, \tag{A.5}$$

$$\mathsf{L}_{ij}^{10,10} = \begin{cases} \dfrac{16\ T}{25\ p}\displaystyle\sum_{k=1}^{N}\dfrac{\overline{M}_i\ y_i\ y_k}{\overline{M}_j\ \left(\overline{M}_i+\overline{M}_k\right)^2\ \mathcal{D}_{ik}}\times & \\ \quad\left[(\delta_{jk}-\delta_{ij})\left(\dfrac{15}{2}\overline{M}_j^2+\dfrac{25}{4}\overline{M}_k^2-3\overline{M}_k^2\ \mathcal{B}_{jk}\right)-\right. & \text{if } i\neq j, \\ \quad\left.4\ \overline{M}_j\ \overline{M}_k\ \mathcal{A}_{jk}\,(\delta_{jk}+\delta_{ij})\left(1+\dfrac{5}{3\ \pi}\left(\dfrac{c_i^r}{K_B\ \xi_{ik}}+\dfrac{c_k^r}{K_B\ \xi_{ki}}\right)\right)\right], & \\ & \\ \dfrac{-16\overline{M}_i\ y_i^2}{\mathcal{R}\ \mu_i}\left(1+\dfrac{10\ c_i^r}{K_B\ \xi_{ii}}\right)-\dfrac{16\ T}{25\ p}\displaystyle\sum_{\substack{k=1\\k\neq i}}^{N}\dfrac{y_i\ y_k}{\left(\overline{M}_i+\overline{M}_k\right)^2\ \mathcal{D}_{ik}}\times & \\ \quad\left[\dfrac{15}{2}\overline{M}_i^2+\dfrac{25}{4}\overline{M}_k^2-3\overline{M}_k^2\ \mathcal{B}_{ik}+\right. & \text{if } i=j, \\ \quad\left.4\ \overline{M}_i\ \overline{M}_k\ \mathcal{A}_{ik}\left(1+\dfrac{5}{3\ \pi}\left(\dfrac{c_i^r}{K_B\ \xi_{ik}}+\dfrac{c_k^r}{K_B\ \xi_{ki}}\right)\right)\right], & \end{cases} \tag{A.6}$$

$$\mathsf{L}_{ij}^{10,01} = \begin{cases} \dfrac{32\ T}{5\ \pi\ p\ c_j^i}\displaystyle\sum_{k=1}^{N}\dfrac{\overline{M}_j\ \mathcal{A}_{jk}}{\left(\overline{M}_j+\overline{M}_k\right)\ \mathcal{D}_{jk}}\,(\delta_{ik}+\delta_{ij})\,y_j y_k\dfrac{c_j^r}{K_B\xi_{jk}}, & \text{if } i\neq j, \\ & \\ \dfrac{16\ \overline{M}_i\ y_i^2\ c_i^r}{3\ \pi\ \mathcal{R}\ \mu_i\ \xi_{ii}\ c_i^i}+\dfrac{32\ T}{5\ \pi\ p\ c_i^i}\displaystyle\sum_{\substack{k=1\\k\neq i}}^{N}\dfrac{\overline{M}_i\ \mathcal{A}_{ik}}{\left(\overline{M}_i+\overline{M}_k\right)\ \mathcal{D}_{ik}}\ y_i\ y_k\dfrac{c_i^r}{\xi_{ik}}, & \text{if } i=j, \end{cases} \tag{A.7}$$

$$\mathsf{L}_{ij}^{01,00} = 0, \tag{A.8}$$

$$\mathsf{L}_{ij}^{01,10} = L_{ji}^{10,01}, \tag{A.9}$$

$$\mathsf{L}_{ij}^{01,01} = \begin{cases} 0, & \text{if } i \neq j, \\ \\ -\dfrac{8\ K_B\ \overline{M}_i\ y_i^2\ c_i^r}{\pi\ \mathcal{R}\ \mu_i\ \xi_{ii}\ {c_i^i}^2} - & \text{if } i = j, \\ \dfrac{4\ K_B\ T}{p\ c_i^i} \left(\displaystyle\sum_{k=1}^{N} \dfrac{y_i\ y_k}{\mathcal{D}_{ik}^i} + \sum_{\substack{k=1 \\ k \neq i}}^{N} \dfrac{12\ y_i\ y_k\ \overline{M}_i\ \mathcal{A}_{ik}\ c_i^r}{5\ \pi\ c_i^i\ \overline{M}_k \mathcal{D}_{ik}\ \xi_{ii}} \right), & \end{cases} \tag{A.10}$$

where $\mathcal{D}_{ik}$ is the binary diffusion coefficient between the i^{th} and k^{th} species, δ_{ij} the Kronecker delta, $\mathcal{A}_{ik}$, $\mathcal{B}_{ik}$, and $\mathcal{C}_{ik}$ three ratios of collision integrals, c_i^r and c_i^i the rotational and internal parts of the molecular specific heat capacity of the i^{th} specie, respectively, $K_B = 1.381 \times 10^{-16}$ erg/K the Boltzmann's constant, ξ_{ik} the relaxation collision numbers, and $\mathcal{D}_{ik}^i$ the binary diffusion coefficient of internal energy between the i^{th} and k^{th} species.

For a linear molecule, $c_i^r = K_B$, otherwise $c_i^r = \frac{3}{2} K_B$. In the nomenclature used in the `Transport` package [62], the internal part, which includes both the rotational and vibrational modes, of the molecular specific heat is given by

$$c_i^i = \frac{c_{p_i}}{\mathcal{N}_A} - c_i^r, \tag{A.11}$$

where $\mathcal{N}_A = 6.022 \times 10^{23}$/mole, is Avogadro's constant. Following the work of [23], it assumed that $\xi_{ik} = \xi_{ii}$. The binary diffusion coefficients for internal energy are approximated by the ordinary binary diffusion coefficients; however, in the case for collisions between polar molecules the following correction is necessary

$$\mathcal{D}_{ik}^i = \frac{\mathcal{D}_{ik}}{1 + 2895\ T^{-3/2}}. \tag{A.12}$$

Additionally, the binary diffusion coefficients, $\mathcal{D}_{ik}$, and pure species viscosities, μ_i, can be related to the collision integrals, $\mathbf{\Omega}$, by

$$\mathcal{D}_{ik} = \frac{3\sqrt{2\ \pi\ K_B^3\ T^3\ \left(\overline{M}_i + \overline{M}_k\right) / \left(\overline{M}_i \overline{M}_k\right)}}{4\ p\ \pi\ \left(\sigma_i + \sigma_k\right)^2 \Omega_{ik}^{(1,1)}}, \tag{A.13}$$

$$\mu_i = \frac{5\sqrt{\pi\ \overline{M}_i\ K_B T}}{16\ \pi\ \sigma_i^2\ \Omega_{ii}^{(2,2)}}, \tag{A.14}$$

where σ_i is the Leonard-Jones collision diameter of the i^{th} specie. Furthermore, the three ratios of collision integrals are given by [8, 86, 159]

$$\mathcal{A}_{ik} = \frac{\Omega_{ik}^{(2,2)}}{2\Omega_{ik}^{(1,1)}}, \tag{A.15}$$

$$\mathcal{A}_{ik} = \frac{5\Omega_{ik}^{(1,2)} - \Omega_{ik}^{(1,3)}}{3\Omega_{ik}^{(1,1)}}, \tag{A.16}$$

$$\mathcal{C}_{ik} = \frac{\Omega_{ik}^{(1,2)}}{3\Omega_{ik}^{(1,1)}}. \tag{A.17}$$

Similar to polynomial fit of Equation (2.35) to Equation (A.14) for the pure species viscosities, μ_i, polynomial fits are provided by the `Transport` package [62] for $\mathcal{D}_{ik}$, $\mathcal{A}_{ik}$, $\mathcal{B}_{ik}$, and $\mathcal{C}_{ik}$ for evaluating the $\mathsf{L}-$matrix system efficiently. Therefore the transport data, the collision integrals, and the relaxation collision numbers are adopted from the `Transport` package [62].

After the system has been computed, the multicomponent diffusion coefficients, D_{ik}, are given by

$$D_{ik} = \frac{16\ T\ \overline{M}\ y_i}{25\ p\ \overline{M}_k} \left(P_{ij} - P_{ii}\right), \tag{A.18}$$

where $\mathbf{P}$ is a $N \times N$ matrix defined as the inverse of the first sub-matrix; $\mathbf{P} = \mathsf{L}^{00,00}$. From the solution to Equation (A.1), the thermal diffusion coefficients, D_i^T, and the isotropic mixture thermal conductivity, k, are given by [8, 62, 86]

$$D_i^T = \frac{8\ \overline{M}_i\ y_i}{5\mathcal{R}} c_{i00}, \tag{A.19}$$

$$\mathsf{k} = -\sum_{i=1}^{N} y_i \left(c_{i10} + c_{i01} \right). \tag{A.20}$$

APPENDIX B

POWER SPECTRAL DENSITY CALCULATION

As mentioned in Chapters 3 and 4, harmonic analysis can be used to extract information about active frequencies in time-signal. The tool used for this purpose is the power spectral density (PSD). The PSD of a signal describes how the variance (or power) is distributed in frequency, and it is real-valued for any real signal. It can be used to reveal possible periodicities in a complex signal.

The continuous PSD is defined as the Fourier transform of the auto–correlation of a signal [7, 43]. The continuous autocorrelation function, $\phi(t)$, of the signal, $p(t)$, is defined as

$$\phi(t) = \int_{-\infty}^{\infty} p(\hat{t}+t)p(\hat{t})d\hat{t}, \tag{B.1}$$

where $\hat{t}$ is a dummy integration variable. Therefore the PSD, $\Phi(\nu)$, is defined as

$$\Phi(\nu) = \int_{-\infty}^{\infty} \phi(\hat{t}) \exp(-2\pi\imath\nu\hat{t})d\hat{t}, \tag{B.2}$$

where ν is the frequency and $\imath$ the square-root of -1. The Fourier transform of the continuous auto-correlation can be written as the magnitude squared of the Fourier transform of the signal by using the Wiener-Khinchin theorem. Thus, the PSD is written as

$$\Phi(\nu) = \left| \int_{-\infty}^{\infty} p(\hat{t}) \exp(-2\pi\imath\nu\hat{t})d\hat{t} \right|^2 = |P(\nu)|^2, \tag{B.3}$$

where $P(\nu)$ is the Fourier Transform of $p(t)$.

In this work, only the discrete one-sided mean-squared amplitude PSD is used. The single-sided PSD is chosen so that the aliasing effect at high frequencies could be bypassed. In order to calculate the discrete PSD for a signal, $p(t)$, suppose that the signal is composed of M equally spaced sample values such that

$$p_m = p(t_m), \qquad t_m = m\Delta t, \qquad m = 0, 1 \ldots M-1, \tag{B.4}$$

where Δt is the spacing, then the standard discrete Fourier transform of p at mode k, P_k, is calculated as

$$P_k = \sum_{m=0}^{M-1} p_m \exp\left(-\frac{2\pi \imath m k}{M}\right), \qquad k = 0, 1 \ldots M/2, \tag{B.5}$$

where mode k is associated with frequency, ν_k. Frequencies are only defined for zero and positive values by

$$\nu_k = \frac{k}{M\Delta t}, \qquad k = 0, 1 \ldots M/2. \tag{B.6}$$

Therefore the one-sided mean-squared PSD, Φ_d, can be calculated as,

$$\begin{aligned}
\Phi_d(0) &= \frac{1}{M^2}\left(P_o P_o\right) = \frac{1}{M^2}|P_o|^2, \\
\Phi_d(\nu_k) &= \frac{1}{M^2}\left(P_k P_k + P_{M-k} P_{M-k}\right) \\
&= \frac{1}{M^2}\left(|P_k|^2 + |P_{M-k}|^2\right) \approx \frac{2}{M^2}|P_k|^2, \qquad k = 1, 2 \ldots (M/2-1), \\
\Phi_d(M/2) &= \frac{1}{M^2}\left(P_{M/2} P_{M/2}\right) = \frac{1}{M^2}|P_{M/2}|^2.
\end{aligned} \tag{B.7}$$

This normalization is chosen to allow the sum of $M/2+1$ values of Φ_d to equal the mean-squared amplitude of the discrete detonation pressure signal, $\frac{1}{M}\sum_{m=0}^{M-1} |p_m|^2$, as shown by Parseval's theorem [100]. Equations (B.7) are the discrete analog of Equation (B.3).

APPENDIX C

NON-INERTIAL FRAME TRANSFORMATION

As mentioned in Section 4.2.1, an accelerating piston is used to initiate a detonation in an initially quiescent, and the one-dimensional governing equations can be transformed to a frame of reference attached to the accelerating piston face. Therefore, if the piston is initially located at $x = 0$, and the velocity of the piston is known function of time, $u_p(t)$, the accelerating frame of can be related to the laboratory frame as

$$\tilde{x} = x - \int_0^t u_p(\hat{t}) d\hat{t}, \tag{C.1}$$

$$\tilde{t} = t, \tag{C.2}$$

and thus, the velocity in the accelerating frame, $\tilde{u}$, can be related to the laboratory frame particle velocity as

$$\tilde{u} = u - u_p(t). \tag{C.3}$$

Therefore, the operators in the laboratory frame can be written in terms of the operators in the accelerating frame of reference as

$$\frac{\partial}{\partial x} = \frac{\partial}{\partial \tilde{x}} \frac{\partial \tilde{x}}{\partial x} + \frac{\partial}{\partial \tilde{t}} \frac{\partial \tilde{t}}{\partial x}, \tag{C.4}$$

$$\frac{\partial}{\partial t} = \frac{\partial}{\partial \tilde{x}} \frac{\partial \tilde{x}}{\partial t} + \frac{\partial}{\partial \tilde{t}} \frac{\partial \tilde{t}}{\partial t}, \tag{C.5}$$

but from equations (C.1-C.2), $\partial\tilde{x}/\partial x = 1$, $\partial\tilde{t}/\partial x = 0$, $\partial\tilde{x}/\partial t = -u_p\left(t\right)$, and $\partial\tilde{t}/\partial t = 1$. Thus, equations (C.4-C.5) can be written as

$$\frac{\partial}{\partial x} = \frac{\partial}{\partial \tilde{x}}, \tag{C.6}$$

$$\frac{\partial}{\partial t} = -u_p\left(t\right)\frac{\partial}{\partial \tilde{x}} + \frac{\partial}{\partial \tilde{t}}. \tag{C.7}$$

To examine the governing equations under this transformation, it is useful to separate the viscous terms from conservative one-dimensional, reactive, Navier-Stokes equations, and thus can be written as

$$\frac{\partial \rho}{\partial t} + \frac{\partial}{\partial x}\left(\rho u\right) = 0, \tag{C.8}$$

$$\frac{\partial}{\partial t}\left(\rho u\right) + \frac{\partial}{\partial x}\left(\rho u^2 + p\right) - \frac{\partial}{\partial x}\left(\tau\right) = 0, \tag{C.9}$$

$$\frac{\partial}{\partial t}\left(\rho\left(e + \frac{u^2}{2}\right)\right) + \frac{\partial}{\partial x}\left(\rho u\left(e + \frac{u^2}{2}\right) + pu\right) + \frac{\partial}{\partial x}\left(q - \tau u\right) = 0, \tag{C.10}$$

$$\frac{\partial}{\partial t}\left(\rho Y_i\right) + \frac{\partial}{\partial x}\left(\rho u Y_i\right) + \frac{\partial}{\partial x}\left(j_i\right) = \overline{M}_i\dot{\omega}_i. \tag{C.11}$$

Now recall, the constitutive relations chosen for mass, momentum, and energy diffusion are given by Equations (2.30),(2.31), and (2.32), and in a one dimension can be written as

$$j_i = -\frac{D_i^T}{T}\frac{\partial T}{\partial x} + \rho\sum_{\substack{k=1\\k\neq i}}^{N}\frac{\overline{M}_i D_{ik} Y_k}{\overline{M}}\left(\frac{1}{y_k}\frac{\partial y_k}{\partial x} + \left(1 - \frac{\overline{M}_k}{\overline{M}}\right)\frac{1}{p}\frac{\partial p}{\partial x}\right), \tag{C.12}$$

$$\tau = \frac{4}{3}\mu\frac{\partial u}{\partial x}, \tag{C.13}$$

$$q = -\mathsf{k}\frac{\partial T}{\partial x} + \sum_{i=1}^{N} j_i h_i - \mathcal{R}T\sum_{i=1}^{N}\frac{D_i^T}{\overline{M}_i}\left(\frac{1}{y_i}\frac{\partial y_i}{\partial x} + \left(1 - \frac{\overline{M}_i}{\overline{M}}\right)\frac{1}{p}\frac{\partial p}{\partial x}\right). \tag{C.14}$$

Applying Equations (C.3), (C.6), and (C.7) to the diffusion constitutive relations and recognizing $\partial u_p / \partial x = 0$, the following is obtained,

$$j_i = -\frac{D_i^T}{T}\frac{\partial T}{\partial \tilde{x}} + \rho \sum_{\substack{k=1 \\ k \neq i}}^{N} \frac{\overline{M}_i D_{ik} Y_k}{\overline{M}} \left(\frac{1}{y_k}\frac{\partial y_k}{\partial \tilde{x}} + \left(1 - \frac{\overline{M}_k}{\overline{M}} \right) \frac{1}{p}\frac{\partial p}{\partial \tilde{x}} \right), \tag{C.15}$$

$$\tau = \frac{4}{3}\mu \frac{\partial \tilde{u}}{\partial \tilde{x}}, \tag{C.16}$$

$$q = -\mathsf{k}\frac{\partial T}{\partial \tilde{x}} + \sum_{i=1}^{N} j_i h_i - \mathcal{R}T \sum_{i=1}^{N} \frac{D_i^T}{\overline{M}_i} \left(\frac{1}{y_i}\frac{\partial y_i}{\partial \tilde{x}} + \left(1 - \frac{\overline{M}_i}{\overline{M}} \right) \frac{1}{p}\frac{\partial p}{\partial \tilde{x}} \right). \tag{C.17}$$

Thus, the viscous terms from Equations (C.9)-(C.11) can be rewritten into the accelerating frame as

$$\frac{\partial}{\partial x}\left(\tau\right) = \frac{\partial}{\partial \tilde{x}}\left(\tau\right), \tag{C.18}$$

$$\frac{\partial}{\partial x}\left(q - \tau u\right) = \frac{\partial}{\partial \tilde{x}}\left(q - \tau \tilde{u}\right), \tag{C.19}$$

$$\frac{\partial}{\partial x}\left(j_i\right) = \frac{\partial}{\partial \tilde{x}}\left(j_i\right), \tag{C.20}$$

where again $\partial u_p / \partial x = 0$ has been used.

The remaining pieces of the governing equations are the one-dimensional, reactive, Euler equations and can be written into the form

$$\frac{\partial \mathbf{U}}{\partial t} + \frac{\partial \mathbf{P_x}}{\partial x} = \mathbf{Q}. \tag{C.21}$$

Thus, by applying the transformation given by Equations (C.6) and (C.7) the following form is obtained:

$$\frac{\partial \mathbf{U}}{\partial \tilde{t}} + \frac{\partial}{\partial \tilde{x}}\left(\mathbf{P_x} - u_p(t)\mathbf{U}\right) = \mathbf{Q}. \tag{C.22}$$

Thus, the transformed Euler equations are

$$\frac{\partial \rho}{\partial \tilde{t}} + \frac{\partial}{\partial \tilde{x}}\left(\rho u - \rho u_p(t)\right) = 0, \tag{C.23}$$

$$\frac{\partial}{\partial \tilde{t}}\left(\rho u\right) + \frac{\partial}{\partial \tilde{x}}\left(\rho u u + p - \rho u u_p(t)\right) = 0, \tag{C.24}$$

$$\frac{\partial}{\partial \tilde{t}}\left(\rho\left(e+\frac{u^2}{2}\right)\right)+\frac{\partial}{\partial \tilde{x}}\left(\rho u\left(e+\frac{u^2}{2}\right)+pu-\rho u_p(t)\left(e+\frac{u^2}{2}\right)\right)=0, \tag{C.25}$$

$$\frac{\partial}{\partial \tilde{t}}\left(\rho Y_i\right)+\frac{\partial}{\partial \tilde{x}}\left(\rho u Y_i-\rho Y_i u_p(t)\right)=\overline{M}_i\dot{\omega}_i. \tag{C.26}$$

Using Equation (C.3), these equations can be written as

$$\frac{\partial \rho}{\partial \tilde{t}}+\frac{\partial}{\partial \tilde{x}}\left(\rho\tilde{u}\right)=0, \tag{C.27}$$

$$\frac{\partial}{\partial \tilde{t}}\left(\rho u\right)+\frac{\partial}{\partial \tilde{x}}\left(\rho u\tilde{u}+p\right)=0, \tag{C.28}$$

$$\frac{\partial}{\partial \tilde{t}}\left(\rho\left(e+\frac{u^2}{2}\right)\right)+\frac{\partial}{\partial \tilde{x}}\left(\rho\tilde{u}\left(e+\frac{u^2}{2}\right)+pu\right)=0, \tag{C.29}$$

$$\frac{\partial}{\partial \tilde{t}}\left(\rho Y_i\right)+\frac{\partial}{\partial \tilde{x}}\left(\rho\tilde{u}Y_i\right)=\overline{M}_i\dot{\omega}_i. \tag{C.30}$$

Now, adding and subtracting $\partial/\partial\tilde{t}\left(\rho u_p(t)\right)$ to Equation (C.28)

$$\begin{aligned}\frac{\partial}{\partial \tilde{t}}\left(\rho u\right)+\frac{\partial}{\partial \tilde{x}}\left(\rho u\tilde{u}+p\right)-\frac{\partial}{\partial \tilde{t}}\left(\rho u_p(t)\right)+\frac{\partial}{\partial \tilde{t}}\left(\rho u_p\right)&=0,\\ \frac{\partial}{\partial \tilde{t}}\left(\rho u\right)-\frac{\partial}{\partial \tilde{t}}\left(\rho u_p(t)\right)+\frac{\partial}{\partial \tilde{x}}\left(\rho u\tilde{u}+p\right)&=-\frac{\partial}{\partial \tilde{t}}\left(\rho u_p\right),\\ \frac{\partial}{\partial \tilde{t}}\left(\rho\tilde{u}\right)+\frac{\partial}{\partial \tilde{x}}\left(\rho u\tilde{u}+p\right)&=-\rho\frac{\partial u_p}{\partial \tilde{t}}-u_p\frac{\partial \rho}{\partial \tilde{t}},\end{aligned} \tag{C.31}$$

then applying Equation (C.27)

$$\begin{aligned}\frac{\partial}{\partial \tilde{t}}\left(\rho\tilde{u}\right)+\frac{\partial}{\partial \tilde{x}}\left(\rho u\tilde{u}+p\right)&=-\rho\frac{\partial u_p}{\partial \tilde{t}}+u_p\frac{\partial}{\partial \tilde{x}}\left(\rho\tilde{u}\right),\\ \frac{\partial}{\partial \tilde{t}}\left(\rho\tilde{u}\right)+\frac{\partial}{\partial \tilde{x}}\left(\rho u\tilde{u}+p\right)-u_p\frac{\partial}{\partial \tilde{x}}\left(\rho\tilde{u}\right)&=-\rho\frac{\partial u_p}{\partial \tilde{t}},\end{aligned} \tag{C.32}$$

and finally recalling $\partial u_p/\partial x=0$ the momentum equation can be rewritten as

$$\frac{\partial}{\partial \tilde{t}}\left(\rho\tilde{u}\right)+\frac{\partial}{\partial \tilde{x}}\left(\rho\tilde{u}\tilde{u}+p\right)=-\rho\frac{du_p}{d\tilde{t}}. \tag{C.33}$$

Similarly, by subtracting Equation (C.33) times the piston velocity from Equation

(C.29), the energy equation becomes

$$\begin{aligned}
&\frac{\partial}{\partial \tilde{t}}\left(\rho\left(e+\frac{u^2}{2}\right)\right)+\frac{\partial}{\partial \tilde{x}}\left(\rho\tilde{u}\left(e+\frac{u^2}{2}\right)+pu\right)\\
&\qquad\qquad - \left(\frac{\partial}{\partial \tilde{t}}\left(\rho\tilde{u}\right) - \frac{\partial}{\partial \tilde{x}}\left(\rho\tilde{u}\tilde{u}+p\right) - \rho\frac{du_p}{d\tilde{t}}\right)u_p = 0,\\
&\frac{\partial}{\partial \tilde{t}}\left(\rho e\right)+\frac{\partial}{\partial \tilde{t}}\left(\rho\frac{u^2}{2}\right)+\frac{\partial}{\partial \tilde{x}}\left(\rho\tilde{u}e+p\tilde{u}\right)+\frac{\partial}{\partial \tilde{x}}\left(\rho\tilde{u}\frac{u^2}{2}\right)\\
&\qquad\qquad - \frac{\partial}{\partial \tilde{t}}\left(\rho\tilde{u}\right)u_p - \frac{\partial}{\partial \tilde{x}}\left(\rho\tilde{u}\tilde{u}\right)u_p - \rho\frac{du_p}{d\tilde{t}}u_p = 0.
\end{aligned}\tag{C.34}$$

By using the chain rule, $\left(\partial/\partial\tilde{t}\left(\rho\tilde{u}u_p\right) = \left(u_p\right)\partial/\partial\tilde{t}\left(\rho\tilde{u}\right) + \left(\rho\tilde{u}\right)\partial/\partial\tilde{t}\left(u_p\right)\right)$, Equation (C.34) can be rewritten as

$$\begin{aligned}
&\frac{\partial}{\partial \tilde{t}}\left(\rho e\right)+\frac{\partial}{\partial \tilde{x}}\left(\rho\tilde{u}e+p\tilde{u}\right)+\frac{\partial}{\partial \tilde{t}}\left(\frac{\rho}{2}\left[u^2-2\tilde{u}u_p\right]\right)\\
&\qquad\qquad +\frac{\partial}{\partial \tilde{x}}\left(\frac{\rho\tilde{u}}{2}\left[u^2-2\tilde{u}u_p\right]\right)+\rho\tilde{u}\frac{\partial u_p}{\partial \tilde{t}}-\rho u_p\frac{\partial u_p}{\partial \tilde{t}} = 0.
\end{aligned}\tag{C.35}$$

Then by completing the square $\left(u^2-2\tilde{u}u_p=\tilde{u}^2+u_p^2\right)$, expanding by $\partial/\partial\tilde{t}\left(\rho u_p^2/2\right)$ $\left(\left(u_p^2/2\right)\partial\rho/\partial\tilde{t}+\left(\rho u_p\right)\partial u_p/\partial\tilde{t}\right)$, and again utilizing $\partial u_p/\partial x=0$ this can be written as

$$\begin{aligned}
&\frac{\partial}{\partial \tilde{t}}\left(\rho e\right)+\frac{\partial}{\partial \tilde{x}}\left(\rho\tilde{u}e+p\tilde{u}\right)+\frac{\partial}{\partial \tilde{t}}\left(\rho\frac{\tilde{u}^2}{2}\right)+\frac{\partial}{\partial \tilde{t}}\left(\rho\frac{u_p^2}{2}\right)\\
&\qquad\qquad +\frac{\partial}{\partial \tilde{x}}\left(\rho\tilde{u}\frac{\tilde{u}^2}{2}\right)+\frac{\partial}{\partial \tilde{x}}\left(\rho\tilde{u}\frac{u_p^2}{2}\right)+\rho\tilde{u}\frac{\partial u_p}{\partial \tilde{t}}-\rho u_p\frac{\partial u_p}{\partial \tilde{t}} = 0,\\
&\frac{\partial}{\partial \tilde{t}}\left(\rho\left(e+\frac{\tilde{u}^2}{2}\right)\right)+\frac{\partial}{\partial \tilde{x}}\left(\rho\tilde{u}\left(e+\frac{\tilde{u}^2}{2}\right)+p\tilde{u}\right)\\
&\qquad\qquad +\frac{u_p^2}{2}\left(\frac{\partial\rho}{\partial \tilde{t}}+\frac{\partial}{\partial \tilde{x}}\left(\rho\tilde{u}\right)\right)+\rho u_p\frac{\partial u_p}{\partial \tilde{t}}+\rho\tilde{u}\frac{\partial u_p}{\partial \tilde{t}}-\rho u_p\frac{\partial u_p}{\partial \tilde{t}} = 0,\\
&\frac{\partial}{\partial \tilde{t}}\left(\rho\left(e+\frac{\tilde{u}^2}{2}\right)\right)+\frac{\partial}{\partial \tilde{x}}\left(\rho\tilde{u}\left(e+\frac{\tilde{u}^2}{2}\right)+p\tilde{u}\right) = -\rho\tilde{u}\frac{du_p}{d\tilde{t}}.
\end{aligned}\tag{C.36}$$

Recombining the inviscid Equations (C.27), (C.33), (C.36), and (C.30) with the viscous terms from Equations (C.18)-(C.20) gives

$$\frac{\partial \rho}{\partial \tilde{t}} + \frac{\partial}{\partial \tilde{x}} \left(\rho \tilde{u} \right) = 0, \tag{C.37}$$

$$\frac{\partial}{\partial \tilde{t}} \left(\rho \tilde{u} \right) + \frac{\partial}{\partial \tilde{x}} \left(\rho \tilde{u}^2 + p - \tau \right) = -\rho \frac{du_p}{d\tilde{t}}, \tag{C.38}$$

$$\frac{\partial}{\partial \tilde{t}} \left(\rho \left(e + \frac{\tilde{u}^2}{2} \right) \right) + \frac{\partial}{\partial \tilde{x}} \left(\rho \tilde{u} \left(e + \frac{\tilde{u}^2}{2} \right) + \left(p - \tau \right) \tilde{u} + q \right) = -\rho \tilde{u} \frac{du_p}{d\tilde{t}}, \tag{C.39}$$

$$\frac{\partial}{\partial \tilde{t}} \left(\rho Y_i \right) + \frac{\partial}{\partial \tilde{x}} \left(\rho \tilde{u} Y_i + j_i \right) = \overline{M}_i \dot{\omega}_i. \tag{C.40}$$

These are the one-dimensional compressible, reactive Navier-Stokes equations in a reference frame attached to the face of an accelerating piston.

BIBLIOGRAPHY

1. A. N. Al-Khateeb, J. M. Powers, and S. Paolucci. On the necessary grid resolution for verified calculation of premixed laminar flames. *Communications in Computational Physics*, 8(2):304–326, 2010.

2. A. N. Al-Khateeb, J. M. Powers, and S. Paolucci. Analysis of the spatio-temporal scales of laminar premixed flames near equilibrium. *Combustion Theory and Modelling*, 17(1):560–595, 2013.

3. M. Arienti and J. E. Shepherd. A numerical study of detonation diffraction. *Journal of Fluid Mechanics*, 529:117–146, 2005.

4. R. Aris. *Vectors, Tensors, and the Basic Equations of Fluid Mechanics*. Dover, Mineola, NY, 1989.

5. J. Austin. *The Role of Instability in Gaseous Detonation*. PhD thesis, California Institute of Technology, 2003.

6. J. Bebernes and D. Eberly. *Mathematical Problems from Combustion Theory*. Springer, New York, NY, 1989.

7. D. R. Billinger. *Time Series: Data Analysis and Theory*. Society for Industrial and Applied Mathematics, Philadelphia, PA, 2001.

8. R. B. Bird, W. E. Stewart, and E. N. Lightfoot. *Transport Phemomena*. Wiley, New York, NY, 2007.

9. A. Bourlioux and A. J. Majda. Theoretical and numerical structure for unstable two-dimensional detonations. *Combustion and Flame*, 90(3):211–229, 1992.

10. A. Bourlioux, A. J. Majda, and V. Roytburd. Theoretical and numerical structure for unstable one-dimensional detonations. *SIAM Journal on Applied Mathematics*, 51(2):303–343, 1991.

11. D. L. Chapman. On the rate of explosion in gases. *Philosophical Magazine*, 47: 90–104, 1899.

12. S. Chapman and T. G. Cowling. *The Mathematical Theory of Non-Uniform Gases: An Account of the Kinetic Theory of Viscosity, Thermal Conduction and Diffusion in Gases*. Cambridge University Press, Cambridge, UK, 1970.

13. W. R. Chapman and R. V. Wheeler. The propagation of flame in mixtures of methane and air. Part V. the movement of the medium in which the flame travels. *Journal of the Chemical Society*, 2139:38–46, 1926.

14. G. Chen. Global solutions to the compressible Navier-Stokes equations for a reacting mixture. *SIAM Journal of Mathematical Analysis*, 23(3):609–634, 1992.

15. A. Chinnayya, A. Hadjadj, and D. Ngomo. Computational study of detonation wave propagation in narrow channels. *Physics of Fluids*, 25(3), 2013. 036101.

16. G. Ciccarelli and J. Card. Detonation in mixtures of JP-10 vapor and air. *AIAA Journal*, 44(2):362–367, 2006.

17. J. F. Clarke, D. R. Kassoy, and N. Riley. On the direct initiation of a plane detonation wave. *Proceedings of the Royal Society of London. Series A: Mathematical and Physical Sciences*, 408(1834):129–148, 1986.

18. J. F. Clarke, D. R. Kassoy, N. E. Meharzi, N. Riley, and R. Vasantha. On the evolution of plane detonations. *Proceedings of the Royal Society of London. Series A: Mathematical and Physical Scienes*, 429(1877):259–283, 1990.

19. Y. Daimon and A. Matsuo. Detailed features of one-dimensional detonations. *Physics of Fluids*, 15(1):112–122, 2003.

20. Y. Daimon and A. Matsuo. Unsteady features on one-dimensional hydrogen-air detonations. *Physics of Fluids*, 19(11), 2007. 116101.

21. R. Deiterding. Detonation structure simulation with AMROC. In *Proceedings of High Performance Computing and Communications*, pages 916–927, 2005.

22. R. Deiterding. A parallel adaptive method for simulating shock-induced combustion with detailed chemical kinetics in complex domains. *Computers and Structures*, 87(11-12):769–783, 2009.

23. G. Dixon-Lewis. Flame structure and flame reaction kinetics. II. Transport phenomena in multicomponent systems. *Proceedings of the Royal Society of London. Series A: Mathematical and Physical Sciences*, 307(1488):111–135, 1968.

24. W. Döring. On the detonation process in gases. *Annals of Physics*, 43:421–436, 1943.

25. R. E. Duff. Investigation of spinning detonation and detonation stability. *Physics of Fluids*, 4(11):1427–1433, 1961.

26. C. A. Eckett. *Numerical and Analytical Studies of the Dynamics of Gaseous Detonations*. PhD thesis, California Institute of Technology, 2001.

27. C. A. Eckett, J. J. Quirk, and J. E. Shepherd. The role of unsteadiness in direct initiation of gaseous detonations. *Journal of Fluid Mechanics*, 421:147–183, 2000.

28. J. J. Erpenbeck. Stability of steady-state equilibrium detonations. *Physics of Fluids*, 5(5):604–614, 1962.

29. J. J. Erpenbeck. Stability of idealized one-reaction detonations. *Physics of Fluids*, 7(5):684–696, 1964.

30. J. A. Fay. A mechanical theory of spinning detonation. *Journal of Chemical Physics*, 20(6):942–950, 1952.

31. R. P. Fedkiw, B. Merriman, and S. Osher. High accuracy numerical methods for thermally perfect gas flows with chemistry. *Journal of Computational Physics*, 132(2):175–190, 1997.

32. M. J. Feigenbaum. The universal metric properties of nonlinear transformations. *Journal of Statistical Physics*, 21(6):669–706, 1979.

33. W. Fickett and W. C. Davis. *Detonation*. University of California Press, Berkeley, CA, 1979.

34. B. Fiorina and S. K. Lele. An artificial nonlinear diffusivity method for supersonic reacting flows with shocks. *Journal of Computational Physics*, 222(1): 246–264, 2007.

35. K. O. Friedrichs. On the mathematical theory of deflagrations and detonations. Technical Report 79-46, NAVORD, 1946.

36. M. Gad-el-Hak. Questions in fluid mechanics: Stokes' hypothesis for a Newtonian, isotropic fluid. *Journal of Fluids Engineering*, 117(1):3–5, 1995.

37. V. N. Gamezo, D. Desbordes, and E. S. Oran. Formation and evolution of two-dimensional cellular detonations. *Combustion and Flame*, 116(1):154–165, 1999.

38. V. N. Gamezo, D. Desbordes, and E. S. Oran. Two-dimensional reactive flow dynamics in cellular detonation waves. *Shock Waves*, 9(1):11–17, 1999.

39. I. Gasser and P. Szmolyan. A geometric singular perturbation analysis of detonation and deflagration waves. *SIAM Journal of Mathematical Analysis*, 24(4): 968–986, 1993.

40. A. I. Gavrikov, A. A. Efimenko, and S. B. Dorofeev. A model for detonation cell size prediction from chemical kinetics. *Combustion and Flame*, 120(1):19–33, 2000.

41. I. Glassman. *Combustion*. Academic Press, New York, NY, 1977.

42. X. J. Gu, D. R. Emerson, and D. Bradley. Modes of reaction front propagation. *Combustion and Flame*, 133(1):63–74, 2003.

43. J. D. Hamilton. *Time Series Analysis*. Princeton University Press, Princeton, NJ, 1994.

44. M. Hanana, M. H. Lefebvre, and P. J. V. Tiggelen. Pressure profiles in detonation cells with rectangular and diagonal structures. *Shock Waves*, 11(2):77–88, 2001.

45. L. He and J. H. S. Lee. The dynamical limit of one-dimensional detonations. *Physics of Fluids*, 7(5):1151–1158, 1995.

46. X. He and A. R. Karagozian. Pulse-detonation-engine simulations with alternative geometries and reaction kinetics. *Journal of Propulsion and Power*, 22 (4):852–861, 2006.

47. A. K. Henrick, T. D. Aslam, and J. M. Powers. Simulations of pulsating one-dimensional detonations with true fifth order accuracy. *Journal of Computational Physics*, 213(1):311–329, 2006.

48. J. O. Hirschfelder and C. F. Curtiss. Theory of detonations. I. irreversible unimolecular reaction. *Journal of Chemical Physics*, 28(6):1130–1147, 1958.

49. X. Y. Hu, D. L. Zhang, B. C. Khoo, and Z. L. Jiang. The cellular structure of a two-dimensional $H_2/O_2/Ar$ detonation wave. *Combustion Theory and Modelling*, 8(2):339–359, 2004.

50. X. Y. Hu, D. L. Zhang, B. C. Khoo, and Z. L. Jiang. The structure and evolution of a two-dimensional $H_2/O_2/Ar$ cellular detonation. *Shock Waves*, 14 (1-2):37–44, 2005.

51. P. H. Hugoniot. On the propagation of movements in bodies, especially perfect gases. *Journal de l'École Polytechnique*, 58:1–125, 1889.

52. J. Humpherys, G. Lyng, and K. Zumbrun. Stability of viscous detonations for Majda's model. *Physica D: Nonlinear Phenomena*, 259:63–80, 2013.

53. Z. Huque, M. R. Ali, and R. Kommalapati. Application of pulse detonation technology for boiler slag removal. *Fuel Processing Technology*, 90(4):558–569, 2009.

54. M. F. Ivanov, A. D. Kiverin, and M. A. Liberman. Hydrogen-oxygen flame acceleration and transition to detonation in channels with no-slip walls for a detailed chemical reaction model. *Physical Review E*, 83(5), 2011. 056313.

55. M. F. Ivanov, A. D. Kiverin, I. S. Yakovenko, and M. A. Liberman. Hydrogen-oxygen flame acceleration and deflagration-to-detonation transition in three-dimensional rectangular channels with no-slip walls. *International Journal of Hydrogen Energy*, 38(36):16427–16440, 2013.

56. D. A. Jones, G. Kemister, E. S. Oran, and M. Sichel. The influence of cellular structure on detonation transmission. *Shock Waves*, 6(3):119–129, 1996.

57. E. Jouguet. On the propagation of chemical reactions in gases. *Journal de Mathématiques Pures et Appliquées*, 1:347–425, 1905.

58. A. K. Kapila, D. W. Schwendeman, J. J. Quirk, and T. Hawa. Mechanisms of detonation formation due to a temperature gradient. *Combustion Theory and Modelling*, 6(4):553–594, 2002.

59. A. R. Kasimov and D. S. Stewart. On the dynamics of self-sustained one-dimensional detonations: A numerical study in the shock-attached frame. *Physics of Fluids*, 16(10), 2004. 3566.

60. D. R. Kassoy. The response of a compressible gas to extremely rapid transient, spatially resolved energy addition: an asymptotic formulation. *Journal of Engineering Mathematics*, 68(3-4):249–262, 2010.

61. D. R. Kassoy, J. A. Kuehn, M. W. Nabity, and J. F. Clarke. Detonation initiation of the microsecond time scale: DDTs. *Combustion Theory and Modelling*, 12(6):1009–1047, 2008.

62. R. J. Kee, G. Dixon-Lewis, J. Warnatz, M. E. Coltrin, and J. A. Miller. A Fortran computer code package for the evaluation of gas-phase multi-component transport properties. Technical Report SAND86-8246, Sandia National Laboratories, 1991.

63. R. J. Kee, F. M. Rupley, and J. A. Miller. Chemkin II: A Fortran chemical kinetics package for the analysis of gas phase chemical kinetics. Technical Report SAND89-8009B, Sandia National Laboratories, 1992.

64. J. Kelly. After combustion: Detonation! top engineers at two aerospace giants race to design the replacement for the jet turbine. *Popular Science*, 263(3): 50–59, 2003.

65. A. M. Khokhlov, E. S. Oran, and G. O. Thomas. Numerical simulation of deflagration-to-detonation transition: The role of shock-flame interactions in turbulent flames. *Combustion and Flame*, 117(1):323–339, 1999.

66. D. Kivotides. Viscous microdetonation physics. *Physics Letters A*, 363(5-6): 458–467, 2007.

67. C. K. Law. *Combustion Physics*. Cambridge University Press, Cambridge, UK, 2006.

68. H. I. Lee and D. S. Stewart. Calculation of linear detonation instability: One-dimensional instability of planar detonations. *Journal of Fluid Mechanics*, 216: 103–132, 1990.

69. J. H. S. Lee. *The Detonation Phenomenon.* Cambridge University Press, Cambridge, UK, 2008.

70. H. F. Lehr. Experiments on shock-induced combustion. *Astronautica Acta*, 17: 589–597, 1972.

71. Z. Liang and L. Bauwens. Cell structure and stability of detonations with pressure-dependent chain-branching reaction rate model. *Combustion Theory and Modelling*, 9(1):93–112, 2005.

72. Z. Liang, S. Browne, R. Deiterding, and J. E. Shepherd. Detonation front structure and the competition for radicals. *Proceedings of the Combustion Institute*, 31(2):2445–2453, 2007.

73. M. A. Liberman, M. F. Ivanov, A. D. Kiverin, M. S. Kuznetsov, A. A. Chukalovsky, and T. V. Rakhimova. Deflagration-to-detonation transition in highly reactive combustible mixtures. *Acta Astronautica*, 67(7-8):688–701, 2010.

74. M. A. Liberman, A. D. Kiverin, and M. F. Ivanov. Regimes of chemical reaction waves initiated by nonuniform initial conditions for detailed chemical reaction models. *Physical Review E*, 85(5), 2012. 056312.

75. G. Little. Mach 20 or bust: Weapons research may yet produce a true spaceplane. *Air & Space Magazine*, 22(4):68–73, 2007.

76. F. K. Lu, P. K. Panicker, D. R. Wilson, and J. Li. System and method for power production using a hybrid helical detonation device, 09 2009. US Patent Application # 20090322102.

77. Y. Lv and M. Ihme. Discontinuous Galerkin method for multicomponent chemically reacting flows and combustion. *Journal of Computational Physics*, 270: 105–137, 2014.

78. G. Lyng and K. Zumbrun. One-dimensional stability of viscous strong detonation waves. *Archives of Rational Mechanical Analysis*, 173(2):213–277, 2004.

79. D. K. Manley, A. McIlroy, and C. A. Taatjes. Research needs for future internal combustion engines. *Physics Today*, 61(11):47–52, 2008.

80. L. Massa, R. Kumar, and P. Ravindran. Dynamic mode decomposition analysis of detonation waves. *Physics of Fluids*, 24(6), 2013. 066101.

81. J. Matthews. Son of a buzz bomb: An engine with a checkered past is the power of the future. *Air & Space Magazine*, 22(4):62–67, 2007.

82. D. W. Mattison, M. A. Oehischlaeger, C. I. Morris, Z. C. Owens, E. A. Barbour, J. B. Jefferies, and R. K. Hanson. Evaluation of pulse detonation engine modeling using laser-base temperature and OH concentration measurements. *Proceedings of the Combustion Institute*, 30(2):2799–2807, 2005.

83. R. M. May. Simple mathematical models with very complicated dynamics. *Nature*, 261(5560):459–467, 1976.

84. K. Mazaheri and S. A. Hashemi. The effect of chain initiation reaction on the stability of gaseous detonations. *Combustion Science and Technology*, 179(8): 1701–1736, 2007.

85. K. Mazaheri, Y. Mahmoudi, and M. I. Radulescu. Diffusion and hydrodynamic instabilities in gaseous detonations. *Combustion and Flame*, 159(6):2138–2154, 2012.

86. H. J. Merk. The macroscopic equations for simultaneous heat and mass transfer in isotropic, continuous and closed systems. *Applied Scientific Research*, 8(1): 73–99, 1959.

87. C. D. Meyer, D. S. Balsara, and T. D. Aslam. A stabilized Runge-Kutta-Legendre method for explicit super-time-stepping of parabolic and mixed equations. *Journal of Computational Physics*, 257:594–626, 2014.

88. V. Mikhelson. The normal velocity of ignition of combustible gaseous mixtures. *Transactions of Moscow University*, 10:1–92, 1893.

89. J. A. Miller, R. E. Mitchell, M. D. Smooke, and R. J. Kee. Toward a comprehensive chemical kinetic mechanism for the oxidation of acetylene: Comparison of model predictions with results from flame and shock tube experiments. In *Symposium (International) on Combustion*, volume 19, pages 181–196, 1982.

90. C. J. Montgomery, A. M. Khokhlov, and E. S. Oran. The effect of mixing irregularities on mixed-region critical length for deflagration-to-detonation transition. *Combustion and Flame*, 115(1):38–50, 1998.

91. I. Müller and T. Ruggeri. *Rational Extended Thermodynamics*. Springer, New York, NY, 1998.

92. H. D. Ng and J. H. S. Lee. Direct initiation of detonation with a multi-step reaction scheme. *Journal of Fluid Mechanics*, 476:179–211, 2003.

93. H. D. Ng, A. J. Higgins, C. B. Kiyanda, M. I. Radulescu, J. H. S. Lee, K. R. Bates, and N. Nikiforakis. Nonlinear dynamics and chaos analysis of one-dimensional pulsating detonations. *Combustion Theory and Modeling*, 9(1): 159–170, 2005.

94. Y. A. Nikolaev, A. A. Vasil'ev, and B. Y. Ul'yanitskii. Gas detonation and its application in engineering and technology (review). *Combustion, Explosion, and Shock Waves*, 39(4):382–410, 2003.

95. D. P. Nolan. *Handbook of Fire and Explosion Protection Engineering Principles for Oil, Gas, Chemical and Related Facilities*. Elsevier, Westwood, NJ, 2011.

96. G. Norris. High-speed strike weapon to build on X-51 flight. *Aviation Week and Space Technology*, 175(16):24–27, 2013.

97. A. K. Oppenheim. Introduction to the gasdynamics of explosions. In *International Center for Mechanical Sciences, Courses and Lectures*, volume 48. Springer, Udine, Italy, 1970.

98. A. K. Oppenheim, R. A. Stern, and P. A. Urtiew. On the development of detonation with pre-ignition. *Combustion and Flame*, 4(4):335–341, 1960.

99. A. K. Oppenheim, N. Manson, and H. G. Wagner. Recent progress in detonation research. *AIAA Journal*, 1(10):2243–2252, 1963.

100. A. V. Oppenheim and R. W. Schafer. *Digital Signal Proccessing*. Prentice-Hall, Englewood Cliffs, NJ, 1975.

101. E. S. Oran and V. N. Gamezo. Origins of the deflagration-to-detonation transition in gas-phase combustion. *Combustion and Flame*, 148(1-2):4–47, 2007.

102. E. S. Oran, J. P. Boris, T. Young, M. Flanigan, T. Burks, and M. Picone. Numerical simulations of detonations in hydrogen-air and methane mixtures. In *Symposium (International) on Combustion*, volume 18, pages 1641–1649, 1981.

103. E. S. Oran, J. W. Weber, E. I. Lefebvre, and J. D. Anderson. A numerical study of a two-dimensional H_2-O_2-Ar detonation using a detailed chemical reaction model. *Combustion and Flame*, 113(1-2):147–163, 1998.

104. E. G. Pantow, M. Fischer, and T. Kratzel. Decoupling and recoupling of detonation waves with sudden expansion. *Shock Waves*, 6(3):131–137, 1996.

105. S. Paolucci, Z. Zikoski, and T. Grenga. WAMR: An adaptive wavelet method for the simulation of compressible reactive flow. Part II. The parallel algorithm. *Journal of Computational Physics*, 272:842–864, 2014.

106. S. Paolucci, Z. Zikoski, and D. Wirasaet. WAMR: An adaptive wavelet method for the simulation of compressible reactive flow. Part I. Accuracy and efficiency of the algorithm. *Journal of Computational Physics*, 272:814–841, 2014.

107. J. M. Powers. Review of multiscale modeling of detonation. *Journal of Propulsion and Power*, 22(6):1217–1229, 2006.

108. J. M. Powers and S. Paolucci. Accurate spatial resolution estimates for reactive supersonic flow with detailed chemistry. *AIAA Journal*, 43(5):1088–1099, 2005.

109. W. H. Press, S. A. Teukolsky, W. T. Vetterling, and B. P. Flannery, editors. *Numerical Recipes in FORTRAN 90: the Art of Parallel Scientific Computing*. Cambridge University Press, Cambridge, UK, 1996.

110. I. Prigogine and R. Defay. *Chemical Thermodynamics*. Longmans, London, UK, 1954.

111. J. J. Quirk. A contribution to the great Riemann solver debate. *International Journal for Numerical Methods in Fluids*, 18(6):555–574, 1994.

112. M. I. Radulescu and R. K. Hanson. Effect of heat loss on pulse-detonation-engine flow fields and performance. *Journal of Propulsion and Power*, 21(2): 274–285, 2005.

113. M. I. Radulescu, G. J. Sharpe, C. K. Law, and J. H. S. Lee. The hydrodynamic structure of unstable cellular detonations. *Journal of Fluid Mechanics*, 580: 31–81, 2007.

114. W. J. M. Rankine. On the thermodynamic theory of waves of finite longitudinal disturbance. *Philosophical Transactions of the Royal Society of London*, 160: 277–288, 1870.

115. Y. A. Rastigejev. *Multiscale Computations with a Wavelet Adaptive Algorithm*. PhD thesis, University of Notre Dame, 2002.

116. Y. A. Rastigejev and S. Paolucci. Wavelet-based adaptive multiresolution computation of viscous reactive flows. *International Journal for Numerical Methods in Fluids*, 52(7):749–784, 2006.

117. Y. A. Rastigejev and S. Paolucci. Wavelet adaptive multiresolution representation: Applications to viscous multiscale flow simulations. *International Journal of Wavelets, Multiresolution, and Information Processing*, 4(2):333–343, 2006.

118. J. D. Regele, D. R. Kassoy, and O. V. Vasilyev. Effect of high activation energies on acoustic timescale detonation initiation. *Combustion Theory and Modelling*, 16(4):650–678, 2012.

119. P. J. Roache. Code verification by the method of manufactured solutions. *Journal of Fluids Engineering*, 124(1):4–10, 2002.

120. C. M. Romick, T. D. Aslam, and J. M. Powers. The effect of diffusion on the dynamics of unsteady detonations. *Journal of Fluid Mechanics*, 699:453–464, 2012.

121. C. M. Romick, T. D. Aslam, and J. M. Powers. Verified and validated calculation of unsteady dynamics of viscous hydrogen-air detonations. *Journal of Fluid Mechanics*, 769:154–181, 2015.

122. G. D. Roy, S. M. Frolov, A. A. Borisov, and D. W. Netzer. Pulse detonation propulsion: Challenges, current status, and future perspective. *Progress in Energy and Combustion Science*, 30(6):545–672, 2004.

123. A. L. Sánchez, M. Carretero, P. Calvin, and F. A. Williams. One-dimensional overdriven detonations with branched-chain kinetics. *Physics of Fluids*, 13(3): 776–792, 2001.

124. I. R. Seitenzahl, C. A. Meakin, D. M. Townsley, D. Q. Lamb, and J. W. Truran. Spontaneous initiation of detonations in white dwarf environments: Determination of critical sizes. *The Astrophysical Journal*, 696(1):515–527, 2009.

125. G. J. Sharpe. Transverse waves in numerical simulations of cellular detonations. *Journal of Fluid Mechanics*, 447:31–51, 2001.

126. G. J. Sharpe. Shock-induced ignition for a two-step chain-branching kinetics model. *Physics of Fluids*, 14(12):4373–4388, 2002.

127. G. J. Sharpe. Linear stability of idealized detonations. *Proceedings of the Royal Society of London. Series A: Mathematical, Physical and Engineering Sciences*, 453(1967):2603–2625, 1997.

128. G. J. Sharpe and S. A. E. G. Falle. Numerical simulations of pulsating detonations: I. nonlinear stability of steady detonations. *Combustion Theory and Modeling*, 4(4):557–574, 2000.

129. G. J. Sharpe and N. Maflahi. Homogeneous explosion and shock initiation for a three-step chain branching reaction model. *Journal of Fluid Mechanics*, 566: 163–194, 2006.

130. G. J. Sharpe and J. J. Quirk. Nonlinear cellular dynamics of the idealized detonation model: Regular cells. *Combustion Theory and Modelling*, 12(1): 1–21, 2008.

131. J. E. Shepherd. Structural response of piping to internal gas detonation. In *2006 Proceedings of the ASME Pressure Vessels and Piping Conference*, Vancouver, BC, Canada, July 2006. PVP2006- ICPVT11-93670.

132. J. E. Shepherd. Detonation in gases. *Proceedings of the Combustion Institute*, 32(1):83–98, 2009.

133. M. Short. An asymptotic derivation of the linear stability of the square-wave detonation using the newtonian limit. *Proceedings of the Royal Society of London. Series A: Mathematical, Physical and Engineering Sciences*, 452(1953): 2203–2224, 1996.

134. M. Short and D. S. Stewart. The multi-dimensional stability of weak-heat-release detonations. *Journal of Fluid Mechanics*, 382:109–135, 1999.

135. M. Short and D. Wang. On the dynamics of pulsating detonations. *Combustion Theory and Modelling*, 5(3):343–352, 2001.

136. M. Short, A. K. Kapila, and J. J. Quirk. The chemical-gas dynamic mechanisms of pulsating detonation wave instability. *Philosophical Transactions of the Royal Society of London. Series A, Mathematical, Physical, and Engineering Sciences*, 357(1764):3621–3637, 1999.

137. A. A. Sileem, D. R. Kassoy, and A. K. Hayashi. Thermally initiated detonation through deflagration to detonation transition. *Proceedings of the Royal Society of London. Series A: Mathematical and Physical Sciences*, 435(1895):459–482, 1991.

138. S. Singh, J. M. Powers, and S. Paolucci. Detonation solutions from reactive Navier-Stokes equations. AIAA Paper 1999-0966, 1999.

139. S. Singh, Y. Rastigejev, S. Paolucci, and J. M. Powers. Viscous detonation in H_2-O_2-Ar using intrinsic low-dimensional manifolds and wavelet adaptive multilevel representation. *Combustion Theory and Modelling*, 5(2):163–184, 2001.

140. N. N. Smirnov and I. I. Panfilov. Deflagration to detonation transition in combustible gas mixtures. *Combustion and Flame*, 101(1-2):91–100, 1995.

141. D. W. Stamps and M. Berman. High-temperature hydrogen combustion in reactor safety applications. *Nuclear Science and Engineering*, 109(1):39–48, 1991.

142. R. A. Strehlow. Gas phase detonations: Recent developments. *Combustion and Flame*, 12(2):81–101, 1968.

143. R. A. Strehlow. *Combustion Fundamentals*. McGraw-Hill, New York, NY, 1984.

144. S. H. Strogatz. *Nonlinear Dynamics and Chaos: With Applications to Physics, Biology, Chemistry, and Engineering*. Westview Press, Cambridge, MA, 2014.

145. M. A. Sussman. *Numerical Simulation of Shock-Induced Combustion*. PhD thesis, Stanford University, 1995.

146. S. Taki and T. Fujiwara. Numerical simulation of triple shock behavior of gaseous detonation. In *Symposium (International) on Combustion*, volume 18, pages 1671–1681, 1981.

147. D. Tan and A. Tesei. Nonlinear stability of strong detonation waves in gas dynamical combustion. *Nonlinearity*, 10(2):355–376, 1997.

148. V. E. Tangirala, A. J. Dean, P. F. Pinard, and B. Varatharajan. Investigations of cycle processes in a pulsed detonation engine operating on fuel-air mixtures. *Proceedings of the Combustion Institute*, 30(2):2817–2824, 2005.

149. B. D. Taylor, D. A. Kessler, V. N. Gamezo, and E. S. Oran. The influence of chemical kinetics on the structure of hydrogen-air detonations. AIAA Paper 2012-0979, 2012.

150. J. Tegnér and B. Sjögreen. Numerical investigation of deflagration to detonation transitions. *Combustion Science and Technology*, 174(8):153–186, 2002.

151. H. H. Teng, Z. L. Jiang, and H. D. Ng. Numerical study on unstable surfaces of oblique detonations. *Journal of Fluid Mechanics*, 744:111–128, 2014.

152. B. Texier and K. Zumbrun. Transition to longitudinal instability of detonation waves is generically associated with Hopf bifurcation to time-periodic galloping solutions. *Communications in Mathematical Physics*, 302(1):1–51, 2011.

153. L. Tisza. Supersonic absorption and Stokes' viscosity relation. *Physical Review*, 61(7-8):531–536, 1942.

154. C. Truesdell. Precise theory of the absorption and dispersion of forced plane infinitesimal waves according to the Navier-Stokes equations. *Journal of Rational Mechanics and Analysis*, 2(5):643–741, 1953.

155. N. Tsuboi, S. Katoh, and K. Hayashi. Three-dimensional numerical simulations for hydrogen/air detonation: Rectangular and diagonal structures. *Proceedings of the Combustion Institute*, 29(2):2783–2788, 2003.

156. N. Tsuboi, K. Eto, and A. K. Hayashi. Detailed structure of spinning detonation in a circular tube. *Combustion and Flame*, 149(1-2):144–161, 2007.

157. O. V. Vasilyev and S. Paolucci. Dynamically adaptive multilevel wavelet collocation method for solving partial differential equations in a finite domain. *Journal of Computational Physics*, 125(2):498–512, 1996.

158. O. V. Vasilyev and S. Paolucci. A fast adaptive wavelet collocation algorithm for multidimensional PDEs. *Journal of Computational Physics*, 138(1):16–56, 1997.

159. W. G. Vincenti and C. H. Kruger. *Introduction to Physical Gas Dynamics*. Wiley, New York, NY, 1965.

160. J. von Neumann. Theory of detonation waves. Technical Report 549, OSRD, 1942.

161. D. H. Wagner. The existence and behavior of viscous structure for plane detonation waves. *SIAM Journal of Mathematical Analysis*, 20(5):1035–1054, 1989.

162. M. A. T. Walter and L. F. F. da Silva. Numerical study of detonation stabilization by finite length wedges. *AIAA Journal*, 44(2):353–361, 2006.

163. B. Wang, H. He, and S. T. J. Yu. Direct calculation of wave implosion for detonation initiation. *AIAA Journal*, 43(10):2157–2169, 2005.

164. C. J. Wang and S. L. Xu. Re-initiation phenomenon of gaseous detonation induced by shock reflection. *Shock Waves*, 16(3):247–256, 2007.

165. C. J. Wang and S. L. Xu. Gaseous detonation propagation in a bifurcated tube. *Journal of Fluid Mechanics*, 599:81–110, 2008.

166. S. D. Watt and G. J. Sharpe. Linear and nonlinear dynamics of cylindrically and spherically expanding detonation waves. *Journal of Fluid Mechanics*, 522: 329–356, 2005.

167. C. R. Wilke. A viscosity equation for gas mixtures. *Journal of Chemical Physics*, 18(4):517–519, 1950.

168. D. N. Williams, L. Bauwens, and E. S. Oran. A numerical study of the mechanisms of self-reignition in low-overdrive detonations. *Shock Waves*, 6(2):93–110, 1996.

169. D. Wirasaet. *Numerical Solutions of Multidimensional Partial Differential Equations Using an Adaptive Wavelet Method*. PhD thesis, University of Notre Dame, 2008.

170. D. Wirasaet and S. Paolucci. An adaptive wavelet method for incompressible flows in complex domains. *Journal of Fluids Engineering*, 127(4):656–665, 2005.

171. W. W. Wood. Existence of detonations for small values of the rate parameter. *Physics of Fluids*, 4(1):46–60, 1961.

172. W. W. Wood. Existence of detonations for large values of the rate parameter. *Physics of Fluids*, 6(8):1081–1090, 1963.

173. S. Xu, T. D. Aslam, and D. S. Stewart. High resolution numerical simulation of ideal and non-ideal compressible reacting flows with embedded internal boundaries. *Combustion Theory and Modeling*, 1(1):113–142, 1997.

174. L. Yuan and T. Tang. Resolving the shock-induced combustion by an adaptive mesh redistribution method. *Journal of Computational Physics*, 224(2):587–600, 2007.

175. S. Yungster and K. Radhakrishan. Pulsating one-dimensional detonations in hydrogen-air mixtures. *Combustion Theory and Modelling*, 8(4):745–770, 2004.

176. S. Yungster and K. Radhakrishan. Structure and stability of one-dimensional detonations in ethylene-air mixtures. *Shock Waves*, 14(1-2):61–72, 2005.

177. V. E. Zakharov and L. A. Ostrovsky. Modulation instability: The beginning. *Physica D : Nonlinear Phenomena*, 238(5):540–548, 2009.

178. Y. B. Zel'dovich. On the theory of the propagation of detonation in gaseous systems. *Soviet Journal of Experimental and Theoretical Physics*, 10(17):542–568, 1940.

179. J. L. Ziegler, R. Deiterding, J. E. Shepherd, and D. I. Pullin. An adaptive high-order hybrid scheme for compressive, viscous flows with detailed chemistry. *Journal of Computational Physics*, 230(20):7598–7630, 2011.

180. Z. J. Zikoski. *A Parallel Adaptive Wavelet Method for Multidimensional Simulations of Hypersonic Propulsion*. PhD thesis, University of Notre Dame, 2011.

This document was prepared & typeset with LaTeX 2_ε*, and formatted with* NDdiss2_ε *classfile (v3.2013[2013/04/16]) provided by Sameer Vijay and updated by Megan Patnott.*